CONTENTS

ABSTRACTS

Ramesh Chand, Gian Chand Rana
Magneto Convection in a Layer of Nanofluid with Soret Effect

Double diffusive convection in a horizontal layer of nanofluid in the presence of uniform vertical magnetic field with Soret effect is investigated for more realistic boundary conditions. The flux of volume fraction of nanoparticles is taken to be zero on the isothermal boundaries. The normal mode method is used to find linear stability analysis for the fluid layer. Oscillatory convection is ruled out because of the absence of the two opposing buoyancy forces. Graphs have been plotted to find the beffects of various parameters on the stationary convection and it is found that magnetic field, solutal Rayleigh number and nanofluid Lewis number stabilizes fluid layer, while Soret effect, Lewis number, modified diffusivity ratio and nanoparticle Rayleigh number destabilize the fluid layer.

Michał Doroszko, Andrzej Seweryn
Modeling of the Tension and Compression Behavior of Sintered 316L Using Micro Computed Tomography

This paper describes the method of numerical modeling of the tension and compression behavior of sintered 316L. In order to take into account the shape of the mesostructures of materials in the numerical modeling, X-ray microtomography was used. Based on the micro-CT images, three-dimensional geometrical models mapped shapes of the porosity were generated. To the numerical calculations was used finite element method. Based on the received stress and strain fields was described the mechanism of deformation of the materials until fracture. The influence of material discontinuities at the mesoscopic scale on macromechanical properties of the porous materials was investigated.

Tomáš Brestovič, Natália Jasminská, Marián Lázár
Application of Analytical Solution for Extended Surfaces on Curved and Squared Ribs

The presented article discusses how to increase heat transfer through ribbed surfaces and it is oriented to the mathematical representation of temperature fields and the total thermal flow. The complexity of solving for some types of ribs with variable cross-section requires the application of numerical methods, which are applied consequently to the planar rib as well. In this case there was chosen the finite-difference method (FDM). During solution of the cylindrical ribs the FDM method is preferably used directly with regard to the complexity of solving for infinite sums and improper integrals in Bessel functions. In conclusion is assessed the application suitability of the calculation procedure applied to curved ribs. This procedure is usually used to planar ribs. At the same time it is pointed out the possibility of using this method for calculation of the total thermal flow through cylindrical ribs, which have got the squared form.

Oleksii Nosko, Takuo Nagamine, Hiroki Mori, Yuichi Sato
Friction-Induced Oscillations of a Non-Asbestos Organic Pin Sliding on a Steel Disc

Friction-induced oscillations result in deterioration of performance of disc brakes and are generally undesired. We conduct experi-mental study of friction-induced oscillations in a non-asbestos organic material / steel pair used in disc brakes of motor vehicles. The tests are done by use of a pin-on-disc machine in which the pin sample is supported on a deformable beam. The adjustable friction parameters are the disc velocity, contact pressure and temperature. The tests show that the friction coefficient decreases with the sliding velocity and increases with the temperature. The friction-induced tangential oscillation of the pin sample occurs with a frequency equal to the first natural frequency of the beam. The effects of the disc velocity and temperature on the oscillation characteristics are investigated. The oscillation amplitude increases with the disc velocity on the interval of velocities below 2 m/s. Temperature changes of several tens of degrees Celsius lead to the oscillation occurrence / decay. The obtained results can be useful for prognostication of friction-induced oscillations in disc brakes with non-asbestos organic pads.

Bogdan Sapiński
Theoretical Analysis of MR Damper Characteristics in Squeeze Mode

The paper summarises the theoretical study of a magnetorheological (MR) damper operated in squeeze mode, intended to be used as an actuator in a semi-active mount system in a car motor. The structural design and operating principle of the damper are described and a simplified model of the MR fluid flow in the gap is presented. The plots of the damper force generated by the MR damper are obtained for monoharmonic piston motion with respect to the centre point of the gap height and in the conditions of the control coil being supplied with direct current.

Marek Gała, Kazimierz Jagieła, Andrzej Jąderko, Janusz Rak
Integrated Multimotor Electrical DC Drive for Metallurgical Rolling Table

A drive system of a section of a metallurgical rolling table consisting of six dc motors, 2220 amperes of total current, fed from a single ABB reversible thyristor converter has been described in this paper. Autonomous excitation circuits of the motors are fed from independent thyristor converters working in the so called MULTIFEX system linked with a supervisory high power converter. There are presented schemes of the DSL communication realized by FEX excitation cards of the motors using the SDSC card of the DCS-800-S02 converter and logic control system based on a PLC controller. The parameterization of the DCS-800 converter and the DCF 803 excitation systems was conducted using the DriveWindow software tool. Significant waveforms of voltages, cur-rents and the estimated motor velocity are described and presented for the idle run as well as during transporting sheets dis-charged from a pusher furnace.

Romuald Mosdorf, Grzegorz Górski
Detection of Two-Phase Flow Patterns in a Vertical Minichannel Using the Recurrence Quantification Analysis

The two-phase flow (water-air) occurring in square minichannel (3x3 mm) has been analysed. In the minichannel it has been ob-served: bubbly flow, flow of confined bubbles, flow of elongated bubbles, slug flow and semi-annular flow. The time series recorded by laser-phototransistor sensor was analysed using the recurrence quantification analysis. The two coefficients:Recurrence rate (RR) and Determinism (DET) have been used for identification of differences between the dynamics of two-phase flow patterns. The algorithm which has been used normalizes the analysed time series before calculating the recurrence plots.Therefore in analy-sis the quantitative signal characteristicswas neglected. De-spite of the neglect of quantitative signal characteristics the analysis of its dynamics (chart of DET vs. RR) allows to identify the two-phase flow patterns. This confirms that this type of analysis can be used to identify the two-phase flow patterns in minichannels.

Sylwia M. Wojda
Comparative Analysis of Two Methods of Assessment Wear of Dental Materials

Wear of dental materials used for permanent dental fillings has a significant impact on their lifetime. Wear products generated dur-ing chewing process involving direct tribological contact between a composite and tooth enamel can cause damage not only to enamel itself but also to the entire tooth structure thus affecting the patient's the health. It is essential therefore to assess the pro-cess of wear rates as well as the useful-ness and effectiveness of the method used to measure these values. As there are a num-ber of different methods used to quantify the loss of dental materials subjected to friction, eg.: scanning digital 3D models of dental casts, confocal microscope scanning or profilographometer measurements, the authors chose to analyze two selected research methods using confocal microscopy and profilographometer to assess their effectiveness. Two commercially available composite dental materials, i.e. ES and FFE previously subjected to friction tests in contact with human dental enamel, were used for the analysis human dental enamel, were used for the analysis.

Grzegorz Golba
Accuracy Assessment for CAD Modeling of Freeform Surface Described by Equation

This paper presents the results of comparative analysis of modeling accuracy the freeform surface constructed by using a variety of algorithms for surface modeling. Also determined the accuracy of mapping the theoretical freeform surface described by mathematical equation. To model surface objects used: SolidWorks 2012, CATIA v5 and Geomagic Studio 12. During the design process of CAD models were used: profile curves, fitting parametric surface and polygonal mesh. To assess the accuracy of the CAD models used Geomagic Qualify 12. On the basis of analyse defined the scope of application of each modeling techniques depending on the nature of the constructed object.

Heorhiy Sulym, Lyubov Piskozub, Yosyf Piskozub, Iaroslav Pasternak
Antiplane Deformation of a Bimaterial Containing an Interfacial Crack with the Account of Friction. I. Single Loading

The paper presents the exact analytic solution to the antiplane problem for a non-homogeneous bimaterial medium containing closed interfacial cracks, which faces can move relatively to each other with dry friction. The medium is subjected to the action of normal and arbitrary single loading in a longitudinal direction. Based on the discontinuity function method the problem is reduced to the solution of the system of singular integral-differential equations for stress and displacement discontinuities at the possible slippage zones. Influence of loading parameters and the effects of friction on the sizes of these zones is analyzed. The stress in-tensity factors, stress and displacement discontinuities, energy dissipation are determined for several characteristic types of external loading.

MAGNETO CONVECTION IN A LAYER OF NANOFLUID WITH SORET EFFECT

Ramesh CHAND*, Gian Chand RANA**

*Department of Mathematics, Government Arya Degree College Nurpur, Himachal Pradesh, 176202, India
**Department of Mathematics, Government College Nadaun, Himachal Pradesh, 177103, India

rameshnahan@yahoo.com, drgcrana15@gmail.com

received 22 February 2015, revised 22 July 2015, accepted 24 July 2015

Abstract: Double diffusive convection in a horizontal layer of nanofluid in the presence of uniform vertical magnetic field with Soret effect is investigated for more realistic boundary conditions. The flux of volume fraction of nanoparticles is taken to be zero on the isothermal boundaries. The normal mode method is used to find linear stability analysis for the fluid layer. Oscillatory convection is ruled out because of the absence of the two opposing buoyancy forces. Graphs have been plotted to find the effects of various parameters on the stationary convection and it is found that magnetic field, solutal Rayleigh number and nanofluid Lewis number stabilizes fluid layer, while Soret effect, Lewis number, modified diffusivity ratio and nanoparticle Rayleigh number destabilize the fluid layer.

Keywords: Nanofluid, Zero-Flux, Soret Effect, Nanofluid Lewis Number, Chandrasekhar Number, Magnetic Field, Galerkin Method

1. INTRODUCTION

Double-diffusive convection is referred to convection induced by temperature and concentration gradients or by concentration gradients of two spices. Double diffusive convection has become important in recent years because of its applications in many fields of science, engineering and technology. Nield (1968) investigate the double-diffusive convection using linear stability analysis for various thermal and solutal boundary conditions. The onset of the double-diffusive convection by using a weak nonlinear theory was investigated by Rudraiah et al.(1982). Later Nield et al. (1993) considered the effects of inclined temperature and solutal gradients on the double convection. Thermal convection in binary fluid driven by the Soret and Dufour effect has been investigated by Knobloch (1980).He has shown that the equations are identical to the thermosolutal problem except relation between the thermal and solutal Rayleigh numbers. Bahloulet al. (2003) investigated the effects of Soret (thermal diffusion) in double –diffusive flow. Thermosolutal convection in the presence of Dufour and Soret effects by Motsa (2008) and found that Soret parameter stabilize while Dufour parameter destabilize the stationary convection. Dufour and Soret effects on thermosolutal convection in a visco-elastic fluid layer have been given by Chand and Rana (2012a, 2014a), Chand et al. (2015a)and observed that Dufour and Sore parameters have significance influence on the fluid layer.

The effect of magnetic field on double-diffusive convection finds importance in geophysics, particularly in the study of Earth's core where the Earth's mantle, which consists of conducting fluid. Magnetic field plays an important role in engineering and industrial applications. These applications include design of chemical processing equipment, formation and dispersion of fog, distributions of temperature and moisture over agricultural fields and groves of fruit trees and damage of crops due to freezing and pollution of the environment etc. Chandrasekhar (1961) studied in detail the thermal convection in a hydromagnetics. Patil and Rudraiah (1973), Alchaar et al.(1995) considered the problem of thermo-solutal convection in the presence of magnetic field for different boundary conditions.

Nanofluids have novel properties that make them potentially useful in wide range of engineering applications where cooling is of primary concern. Nanofluid used as heat transfer, chemical nanofluids, smart fluids, bio-nanofluids, medical nanofluids (drug delivery and functional tissue cell interaction) etc. in many industrial applications.The term nanofluid refers to a fluid containing a suspension of nanoscale particles. This type of fluid is a mixture of a regular fluid, with a very small amount of suspended metallic or metallic oxide nanoparticles or nanotubes, which was first coined by Choi (1995). Suspensions of nanoparticles are being developed medical applications including cancer therapy. Convection in nanofluid based on Buongiorno's model [Buongiorno, (2006)] was studied by Tzou (2008a,b), Alloui et al.(2010), Kuznetsov and Nield (2010a, b , 2011), Nield and Kuznetsov (2009, 2010a, b,c, 2011), Kim et al. (2011), Chand and Rana (2012b,c,d), Chand et al. (2015b). Magneto- convection in a layer of nanofluid finds its applications in biomedical engineering such as MRI, plethora of engineering, power plant cooling systems as well as in computers. Yadav et al. (2013), Chand (2013), Gupta et al. (2013) and Chand and Rana (2014b, 2015) reported various application of magnetic field in a layer of nanofluid heated from below. But the choice of the boundary conditions imposed by them on nanoparticles fraction is somewhat arbitrary; it could be argued that zero-flux for nanoparticles volume fraction is more realistic. Recently Nield and Kuznetsov (2014), Chand el al. (2014), Chand and Rana (2014c,2015) studied the thermal instability of nanofluid by taking normal component of the nanoparticle flux zero at boundary which is more physically realistic. Zero-flux for nanoparticles mean one could control the value of the nanoparticles fraction at the boundary in the same way as the temperature there could be controlled. In this paper an attempt has been made to study the magneto- convection in a horizontal layer

DOI 10.1515/ama-2015-0011

of nanofluid with Soret effect for more realistic boundary conditions.

2. MATHEMATICAL FORMULATIONS OF THE PROBLEM

Consider an infinite horizontal layer of nanofluid of thickness d bounded by surfaces $z = 0$ and $z = d$ heated and soluted from below such that a constant temperature and concentration distribution is prescribed at the boundaries of the fluid layer. Fluid layer is acted upon by gravity force $g(0, 0, -g)$ and a uniform vertical magnetic field $H(0, 0, H)$ as shown in Fig. 1. The temperature and concentration are taken to be T_0 and C_0 at $z = 0$ and T_1 and C_1 at $z = d$, $(T_0 > T_1, C_0 > C_1)$. The reference scale for temperature and nanoparticles fraction is taken to be T_1 and φ_0 respectively.

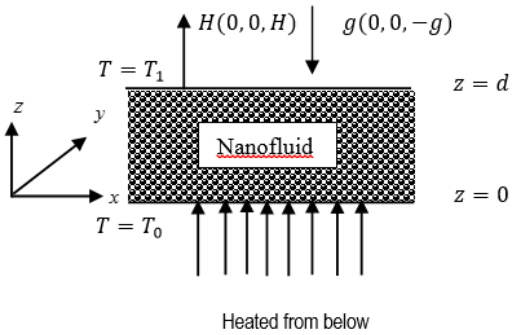

Fig.1. Physical configuration of the problem

2.1. Assumptions

The mathematical equations describing the physical model are based upon the following assumptions:

- Thermo physical properties expect for density in the buoyancy force (Boussinesq Hypothesis)are constant;
- The fluid phase and nanoparticles are in thermal equilibrium state;
- Nanoparticles are spherical;
- Radiation heat transfer between the sides of wall is negligible when compared with other modes of the heat transfer;
- Nanoparticles do not affect the transport of the solute;
- No chemical reactions take place in fluid layer.

2.2. Governing Equations

The appropriate governing equations for magneto double diffusive convection (Chandrasekhar, 1961; Chand, 2013;Nield and Kuznetsov, 2014) are:

$$\nabla \cdot q = 0 \tag{1}$$

$$\rho_0 \frac{\partial q}{\partial t} = -\nabla p + (\phi \rho_p + (1-\phi) \cdot \{\rho_0(1 - \alpha(T - T_0) + \alpha'(C - C_0))\})g + \mu \nabla^2 q + \frac{\mu_e}{4\pi}(H \cdot \nabla)H \tag{2}$$

$$\rho c \frac{\partial T}{\partial t} + (\rho c)_f q \cdot \nabla T = k_m \nabla^2 T + \varepsilon(\rho c)_p \cdot (D_B \nabla \phi \cdot \nabla T + \frac{D_T}{T_1} \nabla T \cdot \nabla T) \tag{3}$$

$$\frac{\partial C}{\partial t} + q \cdot \nabla C = \kappa \nabla^2 C + D_{CT} \nabla^2 T \tag{4}$$

$$\frac{\partial \phi}{\partial t} + q \cdot \nabla \phi = D_B \nabla^2 \phi + \frac{D_T}{T_1} \nabla^2 T \tag{5}$$

where: $q(u, v, w)$ is the velocity vector, ρ_0 is the density of nanofluid at lower boundary layer, φ is the volume fraction of the nanoparticles, ρ_p density of nanoparticles, p is the hydrostatic pressure, μ is the velocity viscosity, μ_e is the magnetic permeability, α is thecoefficientof thermal expansion, α' an analogous solvent coefficient of expansion, $\kappa$is the thermal diffusivity, $\kappa'$is the solute diffusivity of fluid, H is the magnetic field, T is the temperature, C is the solute concentration, ρc is the effective heat capacity of fluid, $(\rho c)_p$ is the heat capacity of nanoparticles, k_m is the effective thermal conductivity of the porous medium, g is acceleration due to gravity, D_B is the Brownian diffusion coefficient, D_T is thethermophoretic diffusion coefficient of the nanoparticles and D_{CT} is the Soret coefficient.

Maxwell equations are:

$$\frac{dH}{dt} = (H \cdot \nabla)q + \eta \nabla^2 H \tag{6}$$

$$\nabla \cdot H = 0 \tag{7}$$

where η is the electrical resitivity.

We assume that the temperature is constant and nanoparticles flux is zero on the boundaries. Thus boundary conditions (Chandrasekhar, 1961; Nield and Kuznetsov, 2014) are:

$$w = 0, T = T_0, C = C_0, D_B \frac{\partial \varphi}{\partial z} + \frac{D_T}{T_1}\frac{\partial T}{\partial z} = 0 at z = 0$$
$$w = 0, T = T_1, C = C_1, D_B \frac{\partial \varphi}{\partial z} + \frac{D_T}{T_1}\frac{\partial T}{\partial z} = 0 at z = d \tag{8}$$

Introducing non-dimensional variables as:

$$(x', y', z') = \left(\frac{x, y, z}{d}\right), q'(u', v', w') = q\left(\frac{u, v, w}{\kappa}\right)d,$$
$$t' = \frac{\kappa}{d^2}t, p' = \frac{d^2}{\mu\kappa}p, \phi' = \frac{(\phi - \phi_0)}{\phi_0}, T' = \frac{T}{\Delta T}, C' = \frac{C}{\Delta C'}, H' = \frac{H}{H}.$$

Equations (1) – (8), in non-dimensional form can be written as:

$$\nabla \cdot q' = 0 \tag{9}$$

$$\frac{1}{Pr}\frac{\partial q'}{\partial t} = -\nabla' p' + \nabla^2 q' - Rm\hat{e}_z + RaT'\hat{e}_z - \frac{Rs}{Le}C'\hat{e}_z - Rn\phi'\hat{e}_z + \frac{Pr}{Pr_M}Q(H' \cdot \nabla')H \tag{10}$$

$$\frac{\partial T'}{\partial t'} + q' \cdot \nabla' T' = \nabla^2 T' + \frac{N_B}{Ln}\nabla'\phi' \cdot \nabla T' + \frac{N_A N_B}{Ln}\nabla' T' \cdot \nabla' T' \tag{11}$$

$$\frac{\partial C'}{\partial t'} + q' \cdot \nabla C' = \frac{1}{Le}\nabla^2 C' + Sr\nabla^2 T' \tag{12}$$

$$\frac{\partial \phi'}{\partial t'} + q' \cdot \nabla \phi' = \frac{1}{Ln}\nabla^2 \phi' + \frac{N_A}{Ln}\nabla^2 T' \tag{13}$$

$$\frac{dH'}{dt'} = (H' \cdot \nabla')q' + \frac{Pr}{Pr_M}\nabla'^2 H' \tag{14}$$

$$\nabla' \cdot \boldsymbol{H}' = 0, \tag{15}$$

where non-dimensional parameters are: $Ln = \frac{\kappa}{D_B}$ is a nanofluid Lewis number, $Le = \frac{\kappa}{\kappa'}$ Lewis number, $Ra = \frac{\rho_0 q \alpha d^3 \Delta T}{\mu\kappa}$ is the thermal Rayleigh number, $Rs = \frac{\rho_0 g \alpha' d^3 \Delta C}{\mu\kappa}$ is the solutal Rayleigh number, $Rm = \frac{\left(\rho_p \phi_0 + \rho(1-\phi_0)\right) g d^3}{\mu\kappa}$ is the basic-density Rayleigh number, $Pr = \frac{\mu}{\rho_0 \kappa}$is the Prandtl number, $Pr_M = \frac{\mu}{\rho_0 \eta}$is the magnetic Prandtl number, Q $= \frac{\mu_e H^2 d^2}{4\pi\rho_0 \upsilon\eta}$ is the Chandrasekhar number, $Rn = \frac{(\rho_p - \rho_0)\phi_0 g d^3}{\mu\kappa}$ is the nanoparticle Rayleigh-Darcy number, $Sr = \frac{D_C T \Delta T}{\kappa \Delta C}$ is the Soret parameter, $N_A = \frac{D_T \Delta T}{D_B T_1 \phi_0}$ is the modified diffusivity ratio, $N_B = \frac{(\rho c)_p \phi_0}{\rho c}$ is the modified particle-density increment.

The dimensionless boundary conditions are:

$$\begin{aligned} &w = 0, T = 1, C = 1, \frac{\partial \varphi}{\partial z} + N_A \frac{\partial T}{\partial z} = 0 \ at \ z = 0 \\ &w = 0, T = 0, C = 0, \frac{\partial \varphi}{\partial z} + N_A \frac{\partial T}{\partial z} = 0 \ at \ z = 1 \end{aligned} \tag{16}$$

2.3. Basic Solutions

The basic state of the nanofluid is assumed to be time independent and is described by $q'(u, v, w) = 0, p' = p'(z)$, $H' = H_b(z), T' = T_b(z), C = C_b(z), \phi = \phi_b(z)$.

The steady state solution is obtained as:

$$T_b = 1 - z, C_b = 1 - z, \phi_b = \varphi_0 + N_A z \tag{17}$$

where φ_0 is reference value for nanoparticles volume fraction.

The basic solution for temperature is same as the solution obtained by Chand (2013) while basic solution for the nanoparticles volume fraction is changed in comparison with Chand (2013).

But these basic solutions are identical with solutions obtained by Nield and Kuznetsov (2014).

2.4. Perturbation Solutions

To study the stability of the system, we superimposed infinitesimal perturbations on the basic state, which are of the forms:

$$\begin{aligned} &q' = 0 + q'', T' = T_{b,} + T'', \phi' = \phi_b + \phi'', p' \\ &= p_b + p'', H' = H_b + h(h_x, h_y, h_z) \\ &\text{with } T_b = 1 - z, C_b = 1 - z, \phi_b = \phi_0 + N_A z \end{aligned} \tag{18}$$

There after dropping the dashes (") for simplicity.

Using the equation (18) in the equations (9) – (15), we obtain the linearized perturbation (neglecting the product of the prime quantities) equations as:

$$\nabla \cdot q = 0 \tag{19}$$

$$\begin{aligned} \frac{1}{Pr}\frac{\partial q}{\partial t} = &-\nabla p + \nabla^2 q + Ra T \hat{e}_z - \frac{Rs}{Le} C \hat{e}_z - Rn \phi \hat{e}_z \\ &+ \frac{Pr}{Pr_M} Q \frac{\partial h}{\partial z} \end{aligned} \tag{20}$$

$$\frac{\partial T}{\partial t} - w = \nabla^2 T + \frac{N_B}{Ln}\left(\frac{\partial T}{\partial z} - \frac{\partial \phi}{\partial z}\right) - \frac{2 N_A N_B}{Ln}\frac{\partial T}{\partial z} \tag{21}$$

$$\frac{\partial C}{\partial t} - w = \frac{1}{Le}\nabla^2 C + Sr \nabla^2 T \tag{22}$$

$$\frac{\partial \phi}{\partial t} + w = \frac{1}{Ln}\nabla^2 \phi + \frac{N_A}{Ln}\nabla^2 T \tag{23}$$

$$\frac{\partial h}{\partial t} = \frac{\partial w}{\partial z} + \frac{Pr}{Pr_M}\nabla^2 h \tag{24}$$

$$\nabla \cdot h = 0 \tag{25}$$

The boundary conditions are:

$$w = 0, T = 0, C = 0, \frac{\partial \varphi}{\partial z} + N_A \frac{\partial T}{\partial z} = 0 at z = 0,1 \tag{26}$$

Now eliminating *p* and *h* from equations (20) by making use of equations (19) and (25), we get:

$$\begin{aligned} &\left(\left(\frac{Pr}{Pr_M}\nabla^2 - \frac{\partial}{\partial t}\right)\left(\frac{1}{Pr}\frac{\partial}{\partial t}\nabla^2 - \nabla^4\right) + \frac{Pr}{Pr_M} Q D^2 \nabla^2\right) w \\ &= \left(\frac{Pr}{Pr_M}\nabla^2 - \frac{\partial}{\partial t}\right)\left(Ra \nabla_H^2 T - \frac{Rs}{Le}\nabla_H^2 C - Rn \nabla_H^2 \phi\right) \end{aligned} \tag{27}$$

3. NORMAL MODES ANALYSIS

Analyzing the disturbances into the normal modes and assuming that the perturbed quantities are of the form:

$$\begin{aligned} [w, T, \phi, C] = [W(z), \Theta(z), \Phi(z), \Gamma(z)] exp\big(&ik_x x \\ &+ ik_y y + nt\big) \end{aligned} \tag{28}$$

where: k_x , k_y are wave numbers in x and y direction and n is growth rate of disturbances.

Using equation (28), equations (27), (19), (21) – (23) become:

$$\begin{aligned} &\left(\left(\frac{Pr}{Pr_M}(D^2 - a^2) - n\right)\left(\frac{n}{Pr}(D^2 - a^2) - (D^2 - a^2)^2\right)\right. \\ &\left. + \frac{Pr}{Pr_M} Q D^2 (D^2 - a^2)\right) W \\ &+ \left(\frac{Pr}{Pr_M}(D^2 - a^2) - n\right)\left(a^2 Ra \Theta\right. \\ &\left. - a^2 \frac{Rs}{Le}\Gamma - a^2 Rn \Phi\right) = 0 \end{aligned} \tag{29}$$

$$\begin{aligned} W + \left(D^2 - a^2 + \frac{N_B}{Ln}D - \frac{2 N_A N_B}{Ln}D - n\right)\Theta - \frac{N_B}{Ln} D\Phi \\ = 0 \end{aligned} \tag{30}$$

$$W + Sr(D^2 - a^2)\Theta + \left(\frac{1}{Le}(D^2 - a^2) - n\right)\Gamma = 0 \tag{31}$$

$$W - \frac{N_A}{Ln}(D^2 - a^2)\Theta - \left(\frac{1}{Ln}(D^2 - a^2) - n\right)\Phi = 0 \tag{32}$$

$where: D \equiv \frac{d}{dz}$ *and* $a = \sqrt{k_x^2 + k_y^2}$ is dimensionless resultant wave number.

DOI 10.1515/ama-2015-0011

The boundary conditions of the problem in view of normal mode analysis are:

$$W = 0, D^2W = \Theta = 0, \Gamma = 0, D\Phi + N_A D\Theta = 0$$
$$at\ z = 0,1. \tag{33}$$

For neutral stability the real part of the n is zero. Hence now we write$n = i\omega$, (where ω is real and is dimensionless frequency of the oscillation).

4. METHOD OF SOLUTION

The Galerkin weighted residuals method is used to obtain an approximate solution to the system of equations (29) – (32) with the corresponding boundary conditions (33). On choosing trial functions (satisfying boundary condition (33)) W, Θ, Γ and Φ as:

$$\mathrm{W} = \sum_{p=1}^{N} A_p \mathrm{W_p}, \Theta = \sum_{p=1}^{N} B_p \Theta_\mathrm{p}$$
$$\Gamma = \sum_{p=1}^{N} C_p \Gamma_\mathrm{p}, \Phi = \sum_{p=1}^{N} D_p \Phi_\mathrm{p} \tag{34}$$

where: A_p, B_p, C_p and D_p are unknown coefficients, $p = 1, 2, 3, \ldots N$ and the base functions W_p, Θ_p,Γ_p and Φ_p are assumed in the following form:

$$W_p = z^{p+1} - 2z^{p+2} + z^{p+3}, \Theta_p = \Gamma_p = z^p - z^{p+1}\Phi_p = -N_A(z^p - z^{p+1}) \tag{35}$$

such that W_p,Θ_p,Γ_p and Φ_p satisfy the corresponding boundary conditions. Using expression for W, Θ, Γ and Φ in equations (29) – (32) and multiplying first equation by W_p second equation by Θ_p and third by Γ_p and forth by Φ_p, and integrating in the limits from zero to unity, we obtain a set of 4N linear homogeneous equations in 4N unknown $A_p, B_p, C_p$and $D_p; p = 1, 2, 3, \ldots N$. For existing of nontrivial solution, the vanishing of the determinant of coefficients produces the characteristics equation of the system in term of Rayleigh number Ra. Thus Ra is found in terms of the other parameters.

5. STATIONARY CONVECTION

Oscillatory convection is ruled out because of the absence of the two opposing buoyancy forces so we consider the case of the stationary convection.

For the first Galerkin approximation we take $N = 1$; the appropriate trial function for boundary condition (33) is given by:

$$W_p = z^2(1-z)^2, \Theta_p = \Gamma_p = z(1-z), \Phi_p = -N_A z(1-z) \tag{36}$$

Substituting trail functions (36) in the system of equations (29) – (32) and using boundary condition (33), we obtain the eigenvalue equation as:

$$\mathrm{R}a - Rs(1-Sr) + (N_A + Ln)LeRn = \frac{28}{27a^2}(a^4 + 24a^2 + 504 + 12Q)(a^2 + 10) \tag{37}$$

In the absence of solute gradient ($Rs = 0, Le = 1$), the corresponding Rayleigh number Ra for steady onset is given by$\mathrm{R}a = \frac{28}{27a^2}(a^4 + 24a^2 + 504 + 12Q)(a^2 + 10) - (N_A + Ln)Rn$.This is good agreement of the result obtained by Chand (2013).

In the absence of magnetic field ($Q = 0$), equation (37) reduces to:

$$\mathrm{R}a - Rs(1-Sr) + (N_A + Ln)LeRn = \frac{28}{27a^2}(a^4 + 24a^2 + 504 + 12Q)(a^2 + 10) \tag{38}$$

The right- hand side of equation (38) takes the minimum value when $a = 3.12$ and its minimum value is 1750. Hence the onset stationary convection is given by: $\mathrm{R}a - Rs(1-Sr) + (N_A + Ln)LeRn = 1750$.

The value 1750 obtained using the Galerkin first term approximation is about 3% greater than exact value 1707.76 for the critical Rayleigh number for the classical Rayleigh- Bénard problem.

In the absence of both magnetic field ($Q = 0$) and solute gradient ($Rs = 0, Le = 1$), the onset of stationary convection is given by $Ra + (N_A + Ln)Rn = 1750$.

This is good agreement of the result obtained by Nield and Kuznetsov (2014).

6. RESULT AND DISCUSSION

Double diffusive convection in a horizontal layer of nanofluid in the presence of vertical magnetic field with Soret effect is investigated. Equation (37) expresses the thermal stationary Rayleigh number Ra as a function of dimensionless wave number a and magnetic field (Chandrasekhar number Q), Lewis number Le, nanofluid Lewis numberLn,modified diffusivity ratio N_A, and nanoparticles Rayleigh number Rn. It is also noted that parameter NB does not appear in the equation, thus instability is purely phenomenon due to buoyancy coupled with the conservation of nanoparticles. It is independent of the contributions of Brownian motion and thermophoresis to the thermal energy equation. The parameter N_B drops out because of an orthogonal property of the first order trail functions and their first derivatives.

Now we discuss the results graphically. Numerical computations are carried out for different values of Chandrasekhar number Q, Lewis number Le, nanofluid Lewis number Ln, Soret parameter Sr and solutal Rayleigh numberRs. The parameters considered are in the range of Chand and Rana (2013, 2014a) $10^2 \leq Ra \leq 10^5$(thermal Rayleigh number), $10^2 \leq Rs \leq 10^5$ (solutal Rayleigh number), $10 \leq Q \leq 10^3$ (Chandrasekhar number), $1 < \varepsilon < 10^{-1}$(porosity parameter), $0 \leq Sr \leq 1$ (Soret parameter), $10^{-1} \leq Le \leq 10$ (Lewis number) $10^2 \leq Ln \leq 10^4$ (nanofluid Lewis number), $1 < N_A < 10$ (modified diffusivity ratio), $1 \leq Rn \leq 10$ (nanoparticle Rayleigh number).

The variation of the stationary thermal Rayleigh number as functions of the wave number for different sets of values for the different parameters are shown in Figs. 2 – 8.

The stationary convection curves in (Ra, a) plane for various values of Chandrasekhar number Q and fixed values of other parameters is shown in Fig. 2. It is found that the Rayleigh number increases with increase in the value of Chandrasekhar number$Q$, thus magnetic field has stabilizing effect on fluid layer.

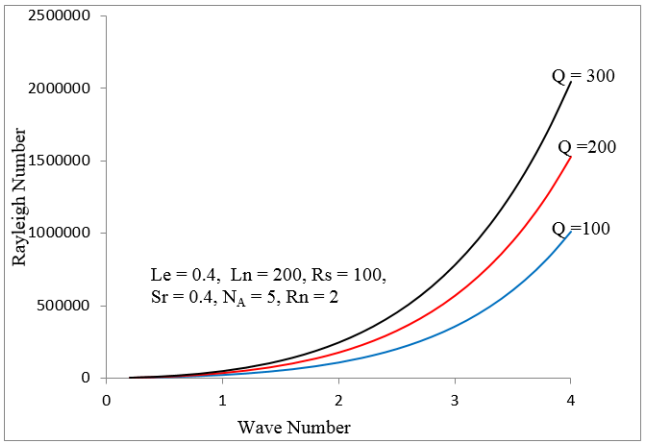

Fig. 2. Variation of Rayleigh number with wave number for different values of Chandrasekhar number

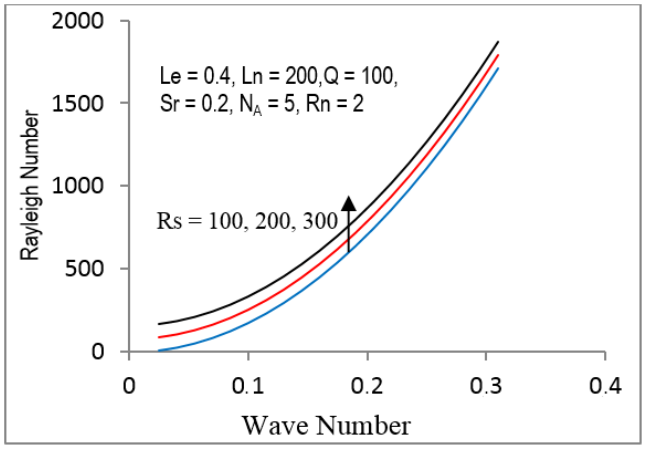

Fig. 3. Variation of stationary Rayleigh number with wave number for different values of solutal Rayleigh number

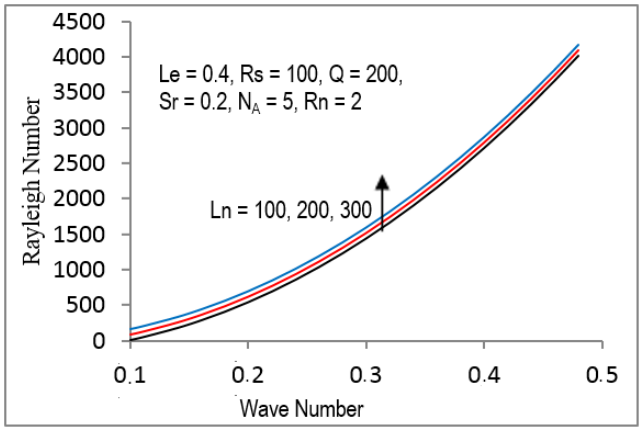

Fig. 4. Variation of stationary Rayleigh number with wave number for different values of nanofluid Lewis number

Fig. 3 shows the variation of thermal Rayleigh number with wave number for different values of solutal Rayleigh number. It is found that the thermal Rayleigh number increases as values of solutal Rayleigh number increases. Thus solutal Rayleigh number stabilizes the fluid layer.

Fig. 4 shows the variation of thermal Rayleigh number with wave number for different values of nanofluid Lewis number. It is found that the thermal Rayliegh number increases as values of nanofluid Lewis number increases. Thus nanofluid Lewis number stabilizes the fluid layer.

Fig. 5 shows the variation of Rayleigh number with wave number for different values of Soret parameter. It is found that the Rayleigh number decreases as values of Soret parameter increases. Thus Soret parameter has destabilizing effect on fluid layer.

Fig. 6 shows the variation of Rayleigh number with wave number for different values of nanoparticle Rayleigh number. It is found that the Rayleigh number decreases as values of nanoparticle Rayleigh number increases. Thus nanoparticle Rayleigh number destabilizes the fluid layer.

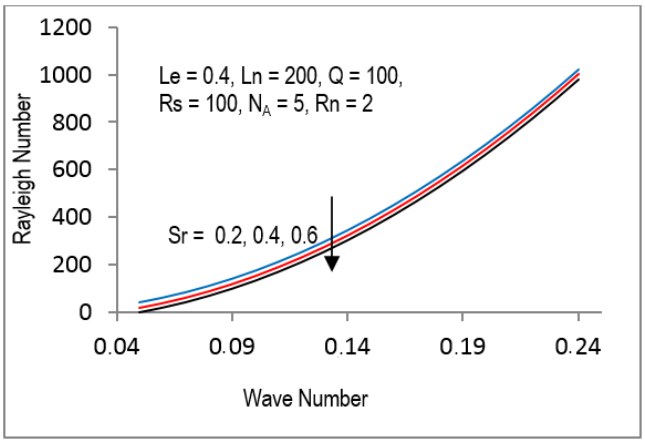

Fig. 5. Variation of stationary Rayleigh number with wave number for different values of Soret parameter

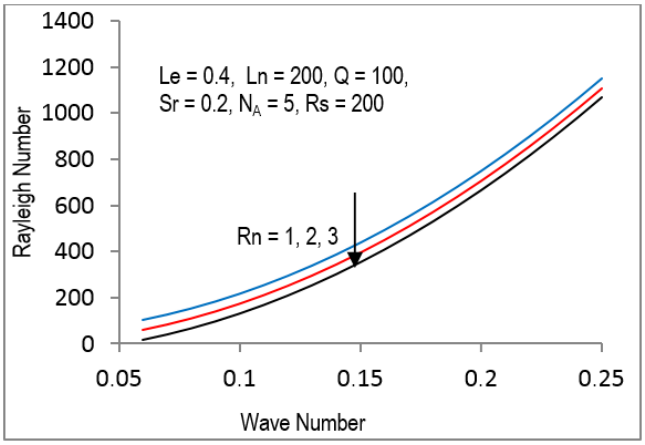

Fig. 6. Variation of stationary Rayleigh number with wave number for different values of nanoparticle Rayleigh number

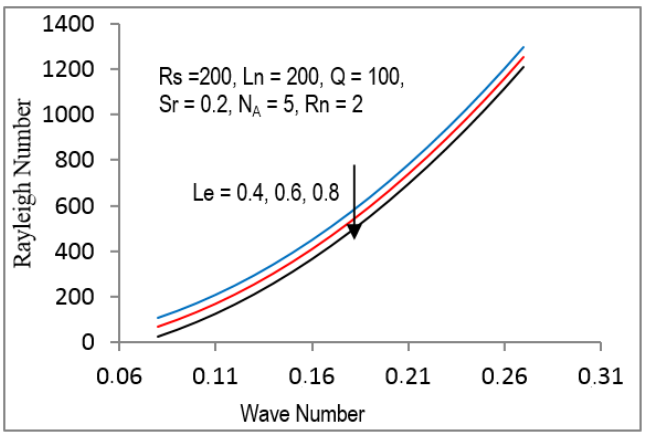

Fig. 7. Variation of stationary Rayleigh number with wave number for different values of Lewis number

DOI 10.1515/ama-2015-0011

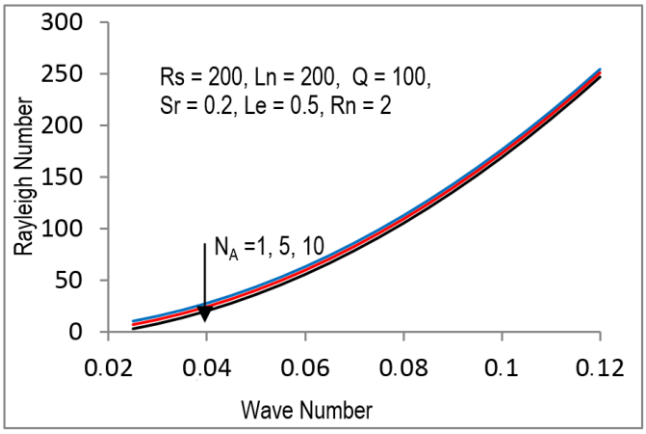

Fig. 8. Variation of Rayleigh number with wave number for different values of modified diffusivity ratio

Fig. 7 shows the variation of Rayleigh number with wave number for different values of Lewis number. It is found that the Rayleigh number decreases as values of Lewis number increases. Thus Lewis number destabilizes the fluid layer.

Fig. 8 shows the variation of Rayleigh number with wave number for different values of modified diffusivity ratio. It is found that the Rayleigh number decreases as values of modified diffusivity ratio increases. Thus modified diffusivity ratio has destabilizing effect on the fluid layer.

7. CONCLUSIONS

Double-diffusive convection in a horizontal layer of nanofluid in the presence of magnetic field with Soret effect is investigated for more realistic boundary conditions. The problem is analyzed boundaries which are isothermal and the flux of volume fractions of nanoparticles is zero on the boundaries.The resulting eigenvalue problem is solved numerically using the Galerkin technique.

The main conclusions are:

- The critical cell size is not a function of any thermo physical properties of nanofluid.
- Instability is purely phenomenon due to buoyancy coupled with the conservation of nanoparticles. It is independent of the contributions of Brownian motion and thermophoresis.
- Oscillatory convection is ruled out because of the absence of the two opposing buoyancy forces.
- For stationary convection the magnetic field, nanofluid Lewis number and solutal Rayleigh number stabilizes fluid layer, while Soret effect, Lewis number modified diffusivity ratio and nanoparticle Rayleigh number destabilize the fluid layer.

Nomenclature: a – wave number, C – solute concentration, c_p – heat capacity, d – thickness of fluid layer, D_B – diffusion coefficient, D_T – thermophoretic diffusion coefficient, D_{CT} –Soret coefficient, g – acceleration due to gravity, H – magnetic field, k_m – thermal conductivity, Le – Lewis number, Ln – nanofluid Lewis number, n – growth rate of disturbances, N_A – modified diffusivity ratio, N_B – modified particle-density increment, p – pressure, Pr – Prandtl number, Pr_M – magnetic Prandtl number, q – velocity of fluid, Q – Chandrasekhar number, Ra –thermal Rayleigh number, Ra_c – critical Rayleigh number, Rm – density Rayleigh number, Rn – concentration Rayleigh number, Rs – solutal Rayleigh number, t – time, T – temperature, T_1 – reference scale for temperature, (u, v, w) – components of fluid velocity, (x, y, z) – space co-ordinates.

Greek symbols: α – thermal expansion coefficient, α' – analogous solvent coefficient of expansion, μ_e – magnetic permeability, μ – viscosity, ρ – density of the nanofluid, ρ_0 – density of the nanofluid at lower boundary, ρ_c – heat capacity, $(\rho c)_p$ – heat capacity of the nanoparticles, φ – volume fraction of the nanoparticles, φ_0 – reference scale for nanoparticles fraction, ρ_p – density of the nanoparticles, ρ_f – density of base fluid, κ – thermal diffusivity, κ' – solute diffusivity, ω – frequency of oscillation, ∂ – curly operator.

Superscripts: $'$ – non-dimensional variables, $''$ – perturbed quantities.

Subscripts: p – particle, f – fluid, s – stationary convection.

REFERENCES

1. **Alchaar S., Vesseur P., Bilgen E.**(1995), Effect of a magnetic field on the onset of convection in a porous medium, *Heat and Mass Transfers*, 30, 259-267.
2. **Alloui Z., Vasseur P., Reggio M.**(2010), Natural convection of nanofluids in a shallow cavity heated from below, *International Journal of Thermal Science*, 50(3), 385-393.
3. **Bahloul A., Boutana N., Vasseur P.** (2003), Double-diffusive and Soret-induced convection in a shallow horizontal porous layer, J. *Fluid Mech.*, 491, 325-352.
4. **Buongiorno J.**(2006), Convective Transport in Nanofluids, *ASME Journal of Heat Transfer*, 12, 240-250.
5. **Chand R.**(2013), On the onset of Rayleigh-Bénard convection in a layer of nanofluid in Hydromagnetics, *Int. J. of Nanoscience*, 12(6), 1350038-7.
6. **Chand R., Kango S. K., Rana G. C.** (2014),Thermal Instability in Anisotropic Porous Medium Saturated by a Nanofluid-A Realistic Approach, *NSNTAIJ*, 8(12), 445-453.
7. **Chand R., Kango S. K., Singh V.** (2015a), Megneto-convection in a layer of Maxwell visco-elastic fluid in a porous medium with Soret effect, *Research J. of Engineering and Tech.*, 6(7), 23-30.
8. **Chand R., Rana G. C.** (2012a), Dufour and Soret effects on the thermosolutal instability of Rivlin-Ericksen elastico-viscous fluid in porous medium, *Z. Naturforsch*, 67a, 685-691.
9. **Chand R., Rana G. C.** (2012b), Oscillating convection of nanofluid in porous medium, *Transp Porous Med.*, 95, 269-284.
10. **Chand R., Rana G. C.** (2012c), On the onset of thermal convection in rotating nanofluid layer saturating a Darcy-Brinkman porous medium, *Int. J. of Heat and Mass Transfer*, 55, 5417-5424.
11. **Chand R., Rana G. C.**(2012d),Thermal instability of Rivlin-Ericksen elastico-viscous nanofluid saturated by a porous medium, *J. Fluids Eng.*, 134(12), 21203-7.
12. **Chand R., Rana G. C.**(2014a), Double diffusive convection in a layer of Maxwell visco-elastic fluid in porous medium in the presence of Soret and Dufour effects, *Journal of Fluids*, 2014, 1-7.
13. **Chand R., Rana G. C.** (2014b), Hall Effect on the thermal instability in a horizontal layer of nanofluid, *Journal of Nanofluids*, 3, 247-253.
14. **Chand R., Rana G. C.** (2014c),Thermal instability in a Brinkman porous medium saturated by nanofluid with no nanoparticle flux on boundaries, Special Topics & Reviews in Porous Media: *An International Journal*, 5(4), 277-286.
15. **Chand R., Rana G. C.** (2015), Magneto convection in a layer of nanofluid in porous medium-A more realistic approach, *Journal of Nanofluids*, 4, 196-202.
16. **Chand R., Rana G. C., Hussein A. K.** (2015b),On the onset of thermal instability in a low Prandtl number nanofluid layer in a porous medium, *Journal of Applied Fluid Mechanics*, 8(2), 265-272.
17. **Chandrasekhar S.**(1961), *Hydrodynamic and Hydromagnetic Stability*, Oxford University Press, Dover Publication, New York.
18. **Choi S.**(1995), Enhancing Thermal Conductivity of Fluids with Nanoparticles in: D.A. Siginer and H. P. Wang (Eds), Developments and Applications of Non-Newtonian Flows, *ASMEFED*, Vol. 231/MD-Vol. 66, 99-105.

19. **Gupta U., Ahuja J., Wanchoo R. K.** (2013), Magneto-convection in a nanofluid layer*, Int. J. Heat and Mass Transfer*, 64, 1163-1171.
20. **Kim J.,Kang Y.T.,Choi C.K.** (2011),Analysis of convective instability and heat transfer characteristics of nanofluids, *Physics of Fluid*, 16(7), 2395-2401.
21. **Knobloch E.,** (1980), Convection in binary fluids, *Phys. Fluids*, 23(9), 1918-1920.
22. **Kuznetsov A. V., Nield D. A. (**2010a), Effect of local thermal non-equilibrium on the onset of convection in a porous medium layer saturated by a nanofluid, *Transport in Porous Media*, 83, 425-436.
23. **Kuznetsov A. V., Nield D. A.** (2010b), The onset of double-diffusive nanofluid convection in a layer of a saturated porous medium, *Transport in Porous Media*, 85(3),941-952.
24. **Kuznetsov A. V., Nield D. A.**(2011), Thermal instability in a porous medium layer saturated by a nanofluid: Brinkman Model, *Transp. Porous Medium*, 81(3), 409-422.
25. **Motsa S. S.** (2008), On the onset of convection in a porous layer in the presence of Dufour and Soret effects, *SJPAM*, 3, 58-65.
26. **Nield D. A.** (1968), Onset of thermohaline convection in a porous medium, *Water Resour. Res.*, 4, 553-560.
27. **Nield D. A., Kuznetsov A. V.** (2009), Thermal instability in a porous medium layer saturated by a nanofluid, *Int. J. Heat Mass Transf.*, 52, 5796-5801.
28. **Nield D. A., Kuznetsov A. V.** (2010a), The on set of convection in a horizontal nanofluid layer of finite depth, European *Journal of Mechanics B/Fluids*, 2, 217-223.
29. **Nield D. A., Kuznetsov A. V.** (2010b), The effect of local thermal non-equilibrium on the onset of convection in a nanofluid, *J. Heat Transfer*, 132(5),052405–052411.
30. **Nield D. A., Kuznetsov A. V.** (2010b), The onset of double-diffusive convection in a nanofluid layer, *Int. J. of Heat and Fluid Flow*, 32(4), 771-776.
31. **Nield D. A., Kuznetsov A. V.** (2011a), The onset of convection in a layer of cellular porous material: Effect of temperature-dependent conductivity arising from radiative transfer, *J. Heat Transfer*, 132(7), 074503-4.
32. **Nield D. A., Kuznetsov A. V.** (2014), Thermal instability in a porous medium layer saturated by a nanofluid: A revised model, I*nt. J. of Heat and Mass Transfer*, 4, 68, 211-214.
33. **Nield D. A., Manole D. M., Lage J. L.** (1993), Convection induced by inclined thermal and thermosolutal gradients in a shallow horizontal layer of porous medium, *J. Fluid Mech.*, 257, 559-568.
34. **Patil R. P., Rudraiah N.** (1973), Stability of hydromagnetic thermoconvective flow through porous medium, *Transactions of the ASME Journal of Applied Mechanics*, 40(E), 879-884.
35. **Rudraiah N., Shrimani P. K., Friedrich R.** (1982), Finite amplitude convection in two component fluid saturated porous layer, *Int. J. Heat and MassTransfer*, 25, 715-722.
36. **Tzou D. Y.** (2008a), Thermal in stability of nanofluids in natural convection, *International Journal of Heat and Mass Transfer*, 51, 2967–2979.
37. **Tzou D. Y.** (2008b), Instability of nanofluids in natural convection, *ASME Journal of Heat Transfer*, 130, 1-9.
38. **Yadav D., Bhargava R., Agrawal G. S.** (2013), Thermal instability in a nanofluid layer with a vertical magnetic field, *J. Eng. Math.*, 80, 147-164.

The authors are grateful to the reviewers for their valuable comments and suggestions for improvement of the paper.

DOI 10.1515/ama-2015-0012

MODELING OF THE TENSION AND COMPRESSION BEHAVIOR OF SINTERED 316L USING MICRO COMPUTED TOMOGRAPHY

Michał DOROSZKO*, Andrzej SEWERYN*

*Faculty of Mechanical Engineering, Department of Mechanics and Applied Computer Science, Bialystok University of Technology, ul. Wiejska 45C, 15-351 Białystok, Poland

m.doroszko@doktoranci.pb.edu.pl, a.seweryn@pb.edu.pl

received 3 March 2015, revised 17 July 2015, accepted 20 July 2015

Abstract: This paper describes the method of numerical modeling of the tension and compression behavior of sintered 316L. In order to take into account the shape of the mesostructures of materials in the numerical modeling, X-ray microtomography was used. Based on the micro-CT images, three-dimensional geometrical models mapped shapes of the porosity were generated. To the numerical calculations was used finite element method. Based on the received stress and strain fields was described the mechanism of deformation of the materials until fracture. The influence of material discontinuities at the mesoscopic scale on macromechanical properties of the porous materials was investigated.

Key words: Finite Element Method, X-Ray Microtomography, Porous Materials, Mechanical Properties, Plasticity

1. INTRODUCTION

Austenitic steel 316L is one of the most commonly used biomaterials for internal fixation devices due to its advantageous combination of mechanical properties, corrosion resistance and cost effectiveness when compared to other metallic implant materials (Disegi and Eschbach, 2000).

Modeling and simulation methods have made significant contributions to understanding of the mechanical properties of cellular materials in conjunction with their structures (Ashby et al., 2000; Rammerstorfer et al., 2002). Determination of the relationships between the structure and properties of cellular materials is a difficult issue because of the complex spatial structure (Kujime et al., 2007; Maruyama et al., 2006). Until recently, in most three-dimensional FEM models were used the simplified control volumes (De Giorgi et al., 2010; Marcadon, 2011; Nammi et al., 2010). Such analyses did not include the effect of the complex geometry which is required for the proper calculation of stress and strain values in the material (Michailidis et al., 2010). Irregular morphology of pores in sintered 316L prevents the use of the geometries simplifications.

Recent researches into cellular materials has been using models mapping the realistic geometries. The most popular method of obtaining cross sections is X-ray computed microtomography (micro-CT). The largest number of works describe the FEM modeling of the strength properties of cellular metallic materials, such as Al open-cell sponge and close-cell foam (Veyhl et al., 2011), porous Al (Michailidis et al., 2010), Ni-foam (Michailidis, 2011), and sintered metal fibers (Veyhl et al., 2013).

This paper presents numerical modeling (FEM) of the tension and compression behavior of porous sintered 316L. Based on high resolution micro-CT images, the structures of the porous materials (on a mesoscale) were mapped as 3D models. On the basis of numerical results, the effect of sintered porous mesostructures on their mechanical properties was described.

2. DETERMINATION OF THE TRUE STRESS-STRAIN CURVE OF THE SOLID 316L

Modeling of the tensile and compression behavior of porous 316L required the determination of the true stress-strain curve of the solid 316L (Sandvik Sanmac 316L). For this reason was carried out the monotonic axial tensile test of the solid material.

In the experiment were used specimens compliant with EN ISO 6892–1:2009. Strength tests were conducted at room temperature using an MTS 322 computer-programmable, hydraulic test machine. For experiments axial extensometer were used with gauge length of 25 mm. The applied rate of specimen displacement was $u_t = 0.02\ \mathrm{mm/s}$, which corresponds to an initial strain rate of $\varepsilon_t = 0.0008\ 1/\mathrm{s}$.

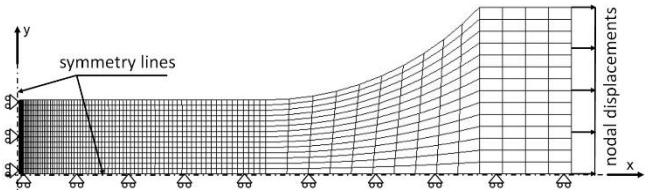

Fig. 1. Boundary conditions used for modeling of the tensile behavior of the axisymmetric model

In order to determine the true work hardening curve of the solid 316L the hybrid method (experimental-numerical) was used (Derpeński and Seweryn, 2011). The curve was further used to define the plastic deformation behavior of sintered 316L in the numerical models. The boundary conditions used in the calculations shown in Fig. 1. The calculations used an elastic-plastic material model with isotropic hardening. The value of Young's modulus $E_s = 202\ \mathrm{GPa}$ was determined empirically and Poisson's ratio was $\nu_s = 0.3$. The received curve $\sigma_{eq} - \varepsilon_{eq}$ (Fig. 2a) defining the solid 316L nonlinearity was obtained iteratively. A comparison of the numerical results and experiments is shown in Fig. 2b.

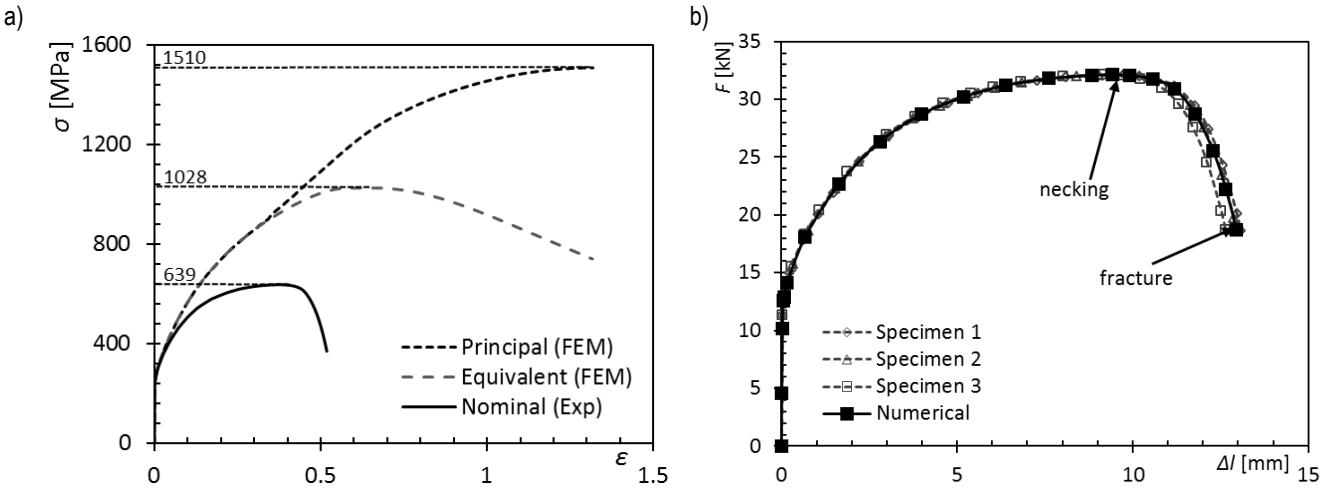

Fig. 2. Comparison of numerical and experimental curves of solid 316L: a) stress-strain, b) force-elongation

The critical force and elongation at which the fracture occurs is determined at the moment when the stress σ_1 has reached the maximum, critical value $\sigma_c = 1510$ MPa (Fig. 3).

Fig. 3. Distributions of principal stress σ_1 at the initial fracture moment

3. NUMERICAL MODELING OF THE TENSION AND COMPRESSION BEHAVIOR OF THE POROUS 316L

For the investigation 3 samples were obtained with porosities of 41, 33 and 26 % using an average pressing pressure of 200, 400 and 600 MPa respectively. In order to take into account the shapes of porous mesostructures in numerical calculations, the microtomography was used. The microtomographic images were obtained by the SkyScan 1172 high resolution micro-CT which is located at the Faculty of Materials Science and Engineering, Warsaw University of Technology. The procedure of mapping three-dimensional porous structures using micro-CT is shown in Fig. 4. Three porous models were separated with the dimensions $0.45 \times 0.2 \times 0.6$ mm, one for each of the porosities. The 3D geometric models were created using Materialise Mimics software.

For the numerical modeling, MSC.Marc software based on finite element method (FEM) was used. In the calculations were used Tetra 134 tetrahedral isoparametric 4-node finite elements (Marc® 2010, Product Documentation). For modeling of the tensile and compression behavior of the porous materials the boundary conditions based on nodal displacements and contact were used (Fig. 5). Application of the fixed displacements in appropriate directions define the symmetry conditions. To modeling of the compression behavior were used two approaches (compression I and II). The first approach was applied for macroscopic deformation $\varepsilon \leq 0.1$ because further deformation causes a distortions of meshes which are inconsistent with the physical process of compression. In compression I and II, self-contact was applied in order to take into account the effect of closing the pores. For models used in compression II added bases and rigid contact surfaces which prevent improper distortions such as in the case of compression I. Coulomb model was used to modeling of friction in contact. The calculations used the elastic-plastic material model using the Huber-von Mises plasticity yield criteria. Young's modulus $E_s = 202$ GPa and Poisson's ratio $\nu_s = 0.3$ determined experimentally were assumed. The material nonlinearity was determined by the curve $\sigma_{eq} - \varepsilon_{eq}$ (Fig. 2a).

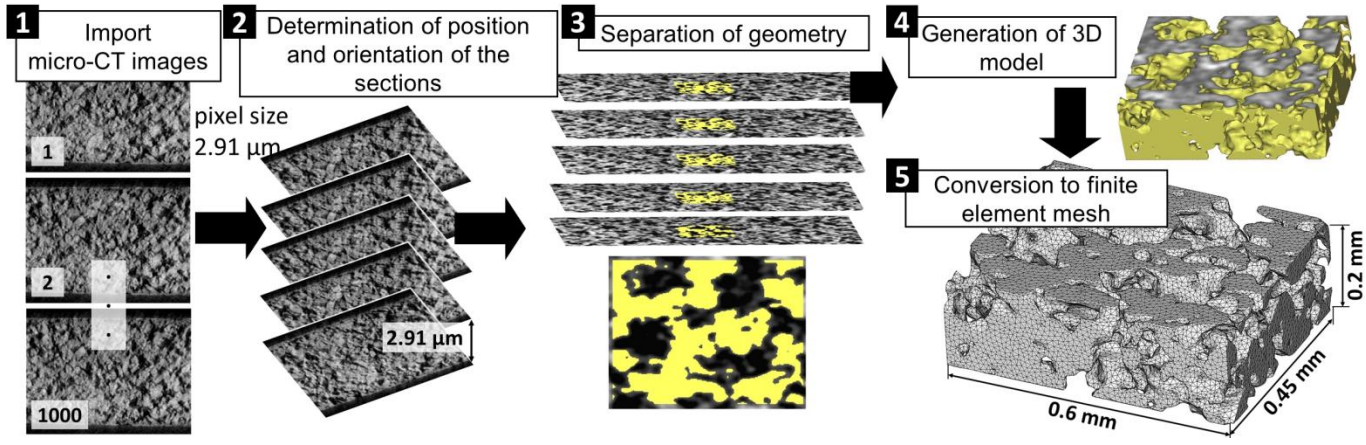

Fig. 4. The procedure of mapping 3D porous structures using micro-CT

DOI 10.1515/ama-2015-0012

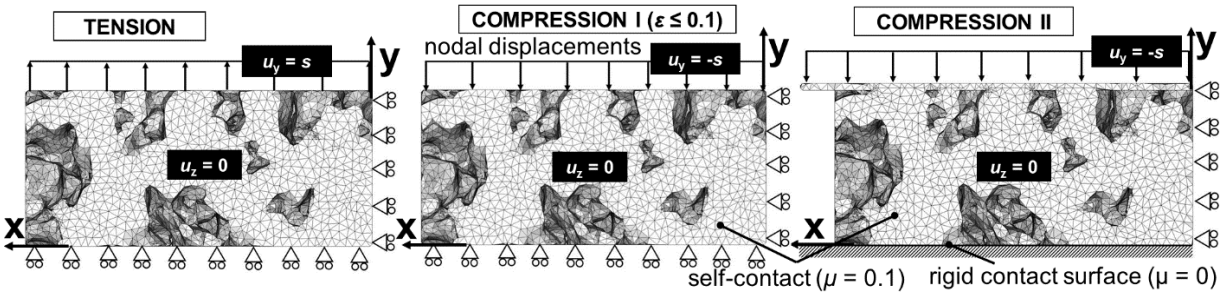

Fig. 5. The boundary conditions used for modeling of the tension and compression of sintered 316L

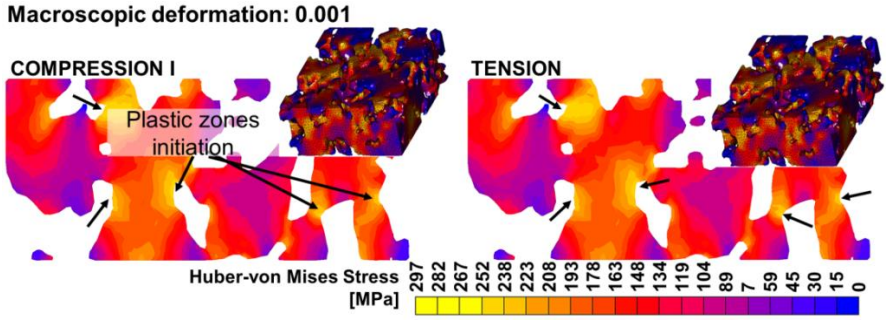

Fig. 6. Huber-von Mises Stress distributions indicating plastic zones initiation

4. NUMERICAL RESULTS

To indicate the plastic zones initiation, Huber-von Mises stress distributions were used in models deformed in 0.1%. Plastic zones initiation are localized in notches in the pores shape. An example of the stress distributions in the sinter with the 41% of porosity shown in Fig. 6. Fig. 6 shows similarity between stress distributions obtained for the tension and compression in small strain (macroscopic) range. This is due to the solid 316L deformation process in small strain range, where tensile and compressive stress values are equal.

Because of not taking into account the fracture criteria in the calculations, critical strain εc (macroscopic nominal strain) at the macro fracture in tension was determined on the basis of experimental results (Falkowska and Seweryn, 2015). In the investigation it was assumed that crack initiation in the material occurs at the maximum principal stress value $\sigma_c = 1510\ \mathrm{MPa}$, received experimentally for solid 316L (Fig. 2a). Principal stress σ1 distributions at the macro fracture moment shown in Fig. 7. Locations where have been achieved stress values close to the critical σ_c were indicated using arrows. Areas of crack initiation are localized in notches in the pores shape as in the case of plasticity initiation.

In Fig. 8 is shown comparison of the principal stress distributions obtained using two approaches of compression (I and II) when macroscopic strain $\varepsilon = 0.1$. As seen the stress distributions are similar to each other. This means that the both methods may be used alternatively up to 10% of macroscopic strain. Deformation larger than 10% using the method of compression I causes a distortions of meshes (Fig. 9). Principal stress distributions in sinters with porosity of 41% and 26%, deformed in 20, 30 and 40%, obtained using compression II shown in Fig. 10. Locations where compressive stresses reach the highest values are bridges with the smallest cross sections and notches in the shape of the pores.

Based on the stress and strain fields, the mechanism of macroscopic deformation was investigated. The influence of material discontinuities at the mesoscopic scale on macromechanical properties of the sintered materials describes nominal stress-strain curves shown in Fig. 11. The presented results indicate that value of porosity it is crucial factor which determine the tension and compresssion behavior of the porous materials. The mechanical properties decrease with the increase in porosity. It should be noted that there is high compliance between the results obtained by both methods used for compression modeling.

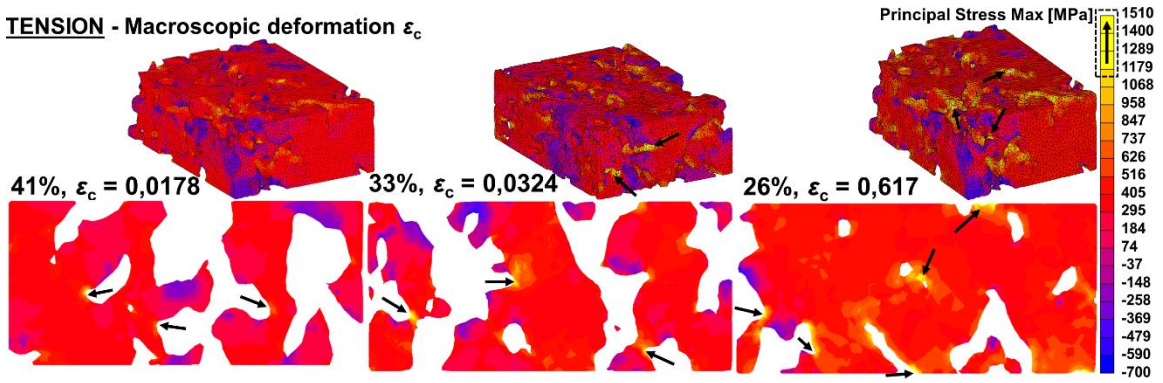

Fig. 7. Principal stress σ_1 distributions at the critical strain moment ε_c

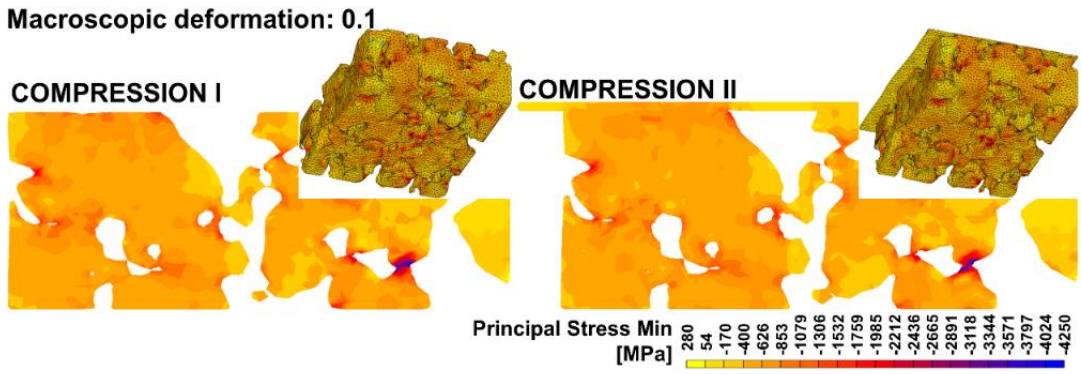

Fig. 8. Huber-von Mises Stress distributions indicating plastic zones initiation

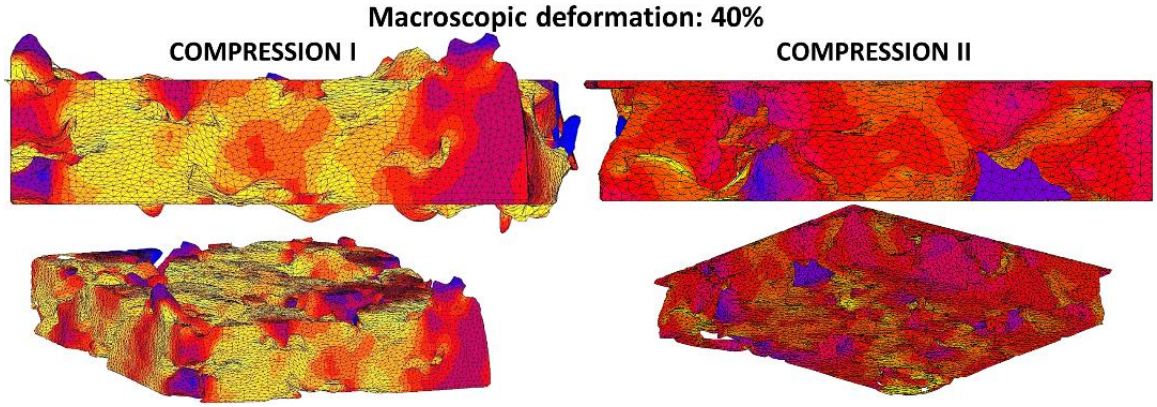

Fig. 9. Huber-von Mises Stress distributions indicating plastic zones initiation

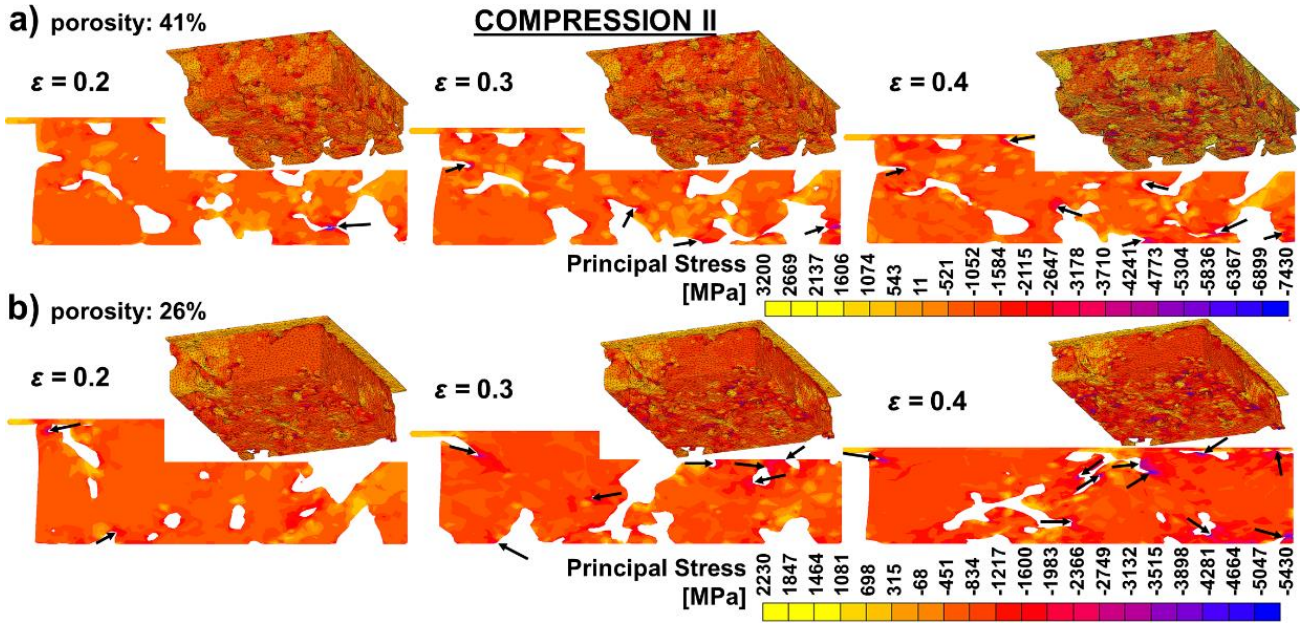

Fig. 10. Principal stress distributions obtained using compression II for porous 316L with porosity of: a) 41%, b) 26%

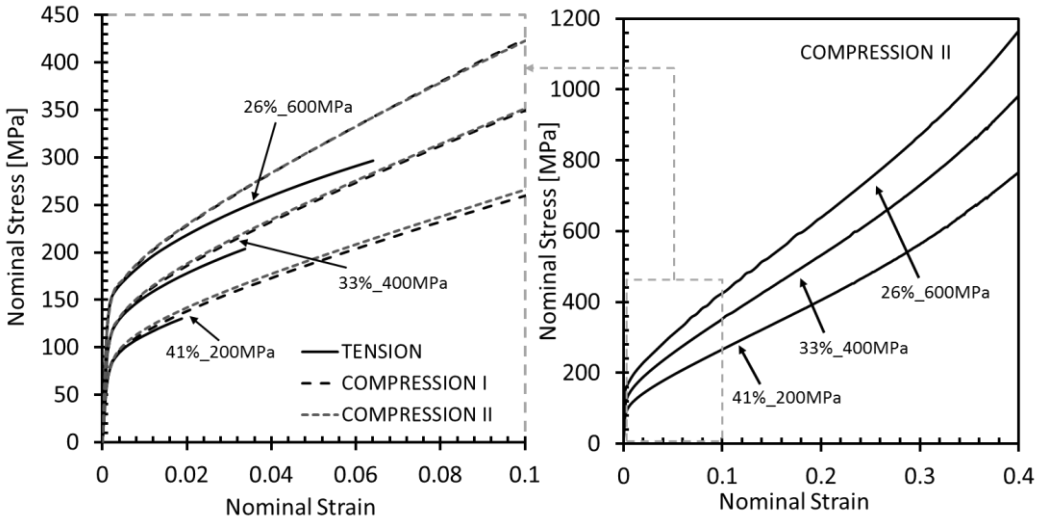

Fig. 11. Nominal stress-strain curves obtained for the sintered 316L

5. CONCLUSIONS

The paper presents modeling of the tensile and compression behavior of sintered 316L with a porosity of 41, 33 and 26%, taking into account the pore shapes at the mesoscale.

The macromechanical properties of the sinters depends on the stress values in the bridges which connect the mesostructures. The deformation mechanism have reflection in the received hardening curves and showing an increase in values of Young's modulus, yield strength and ultimate strength with decreasing porosity. The presented results can be useful in design process of external and internal fixators to decribe the macroscopic non-linearity of sintered 316L.

Due to the insufficient micro-CT accuracy, an important issue is research on methods which reduce the impact of the non-mapped geometries on mechanical properties of the materials. One of such method was proposed by Veyhl C. et al. (2013). Its application to the model described in this paper will be the subject of future research.

Taking into account the stress concentration in bridges of the mesostructures, an important issue is to model the damage accumulation process and cracking at these locations.

REFERENCES

1. **Disegi J. A., Eschbach L.** (2000), Stainless steel in bone surgery, *Injury*, 31,S-D2-6.
2. **Ashby M. F., Evans A. G., Fleck N. A., Gibson L. J., Hutchinson J. W., Wadley H. N. G.** (2000), *Metal Foams: A Design Guid*, Oxford: Butterworth-Heinemann.
3. **Rammerstorfer F. G., Daxner T., Bohm H. J.** (2002), Modeling and Simulation. In: Degischer HP, Kriszt B, editors. *Handbook of Cellular Metals: Production, Processing Applications*, Germany: Wiley-VCH.
4. **Kujime T., Tane M., Hyun S. K., Nakajima H.** (2007), Three-dimensional image-based modeling of lotus-type porous carbon steel and simulation of its mechanical behaviour by finite element method, *Materials Science and Engineering A*, 460-461, 220-226.
5. **Maruyama B., Spowart J. E., Hooper D. J., Mullens H. M., Druma A. M., Druma C., Alam M. K.** (2006), A new technique for obtaining three-dimensional structures in pitch-based carbon foams. *Scripta Materialia*, 54, 1709-1713.
6. **De Giorgi M., Carofalo A., Dattoma V., Nobile R., Palano F.** (2010), Aluminium foams structural modelling, *Computers & Structures*, 88, 25-35.
7. **Marcadon V.** (2011), Mechanical modelling of the creep behaviour of Hollow-Sphere Structures, *Computational Materials Science*, 50, 3005-3015.
8. **Nammi S. K., Myler P., Edwards G.** (2010), Finite element analysis of closed-cell aluminium foam under quasi-static loading. *Materials and Design*, 31, 712-722.
9. **Michailidis N., Stergioudi F., Omar H., Tsipas D. N.** (2010), An image-based reconstruction of the 3D geometry of an Al open-cell foam and FEM modeling of the material response, *Mechanics of Materials*, 42, 142-147.
10. **Veyhl C., Belova I. V., Murch G. E., Fiedler T.** (2011), Finite element analysis of the mechanical properties of cellular aluminium based on micro-computed tomography, *Materials Science and Engineering A,* 528, 4550-4555.
11. **Michailidis N., Stergioudi F., Omar H., Tsipas D.** (2010), FEM modeling of the response of porous Al in compression, *Computational Materials Science*, 48, 282-286.
12. **Michailidis N.** (2011) Strain rate dependent compression response of Ni-foam investigated by experimental and FEM simulation methods, *Materials Science and Engineering A*, 528, 4204-4208.
13. **Veyhl C., Fiedler T., Jehring U., Andersen U., Bernthaler T., Belova I. V., Murch G.E.** (2013), On mechanical properties of sintered metallic fibre structures, *Materials Science and Engineering A*, 562, 83-88.
14. *EN ISO 6892-1:2009*, Metallic materials – Tensile testing – Part 1: Method of test at room temperature, CEN: 2009.
15. **Derpeński Ł., Seweryn A.** (2011), Experimental Research into Fracture of EN-AW 2024 and EW-AW 2007 Aluminum Alloy Specimens with Notches Subjected to Tension, *Experimental Mechanics*, 51, 1075-1094.
16. *Marc® 2010*, Product Documentation, Volume B: Element Library.
17. **Falkowska A., Seweryn A.** (2015), Fatigue of sintered porous materials based on 316l stainless steel under uniaxial loading. *Materials Science* (in press).

The paper has been accomplished under the research project No. S/WM/1/2013 financed by the Bialystok University of Technology. M. Doroszko is a beneficiary of the project 'Scholarships for PhD students of Podlaskie Voivodeship'. The project is co-financed by European Social Fund, Polish Government and Podlaskie Voivodeship.

APPLICATION OF ANALYTICAL SOLUTION FOR EXTENDED SURFACES ON CURVED AND SQUARED RIBS

Tomáš BRESTOVIČ*, Natália JASMINSKÁ*, Marián LÁZÁR

*Faculty of Mechanical Engineering, Technical University in Kosice, Department of Power Engineering, Vysokoškolská 4, 042 00 Košice, Slovak Republic

tomas.brestovic@tuke.sk, natalia.jasminska@tuke.sk, marian.lazar@tuke.sk

received 20 October 2014, revised 18 May 2015, accepted 21 May 2015

Abstract: The presented article discusses how to increase heat transfer through ribbed surfaces and it is oriented to the mathematical representation of temperature fields and the total thermal flow. The complexity of solving for some types of ribs with variable cross-section requires the application of numerical methods, which are applied consequently to the planar rib as well. In this case there was chosen the finite-difference method (FDM). During solution of the cylindrical ribs the FDM method is preferably used directly with regard to the complexity of solving for infinite sums and improper integrals in Bessel functions. In conclusion is assessed the application suitability of the calculation procedure applied to curved ribs. This procedure is usually used to planar ribs. At the same time it is pointed out the possibility of using this method for calculation of the total thermal flow through cylindrical ribs, which have got the squared form.

Key words: Temperature Field, Thermal Flow, Numerical Solution, Finite-Difference Method

1. INTRODUCTION

Cooling of energy equipments, transport vehicles, as well as electronic components requires intensification of heat transfer from a cooled surface. (Increasing the cooling medium speed OR Increase of cooling medium speed) Increase of the cooling medium speed often does not produce the expected cooling effect. Therefore, the cooling area is increased additionally by means of the newly created ribs. In terms of design the ribs can be either planar or cylindrical. Determination of the total thermal flow for each type of extended surfaces is possible only in the simplified cases usually because a solving of the complex non-linear differential equations of higher order is a task difficult enough. Analysis of the differential equation for a planar rib with a constant rib cross-section, ignoring radiation, enables to obtain the thermal flows and temperature fields using analytical method for various boundary conditions (Maga and Harťanský, 2005).

If there is taken into consideration radiation and dependence of the relevant values on the temperature and on the rib length, it is therefore necessary to use the numerical mathematics. Evidently, the simplest method of numerical solution for ribs seems to be an application of the finite difference method (FDM) (Brestovič and Jasminská, 2013; Pyszko et al., 2010; Purcz, 2001). Application of this method is necessary also for some simple cases. The typical situation is for cylindrical ribs, which temperature fields can be determined by means of Bessel functions. These functions represent solution of improper integrals and infinite sums. That is why it is more suitable to use FDM, which allows to see the changes regard changes of all values in relation to a temperature and a rib length.

Introduction of certain simplified assumption enables to eliminate necessity of solution for two and three dimensional heat conduction. Typical situation is in the case of curved ribbed surfaces or squared ribs. In this situation it is possible to retransform a given task to one-dimensional solution with regard to possible calculation failure. An advantage is a quick solution process (Mlynár and Masaryk, 2012; Ferstl and Masaryk, 2011; Purcz, 2001).

This article offers a complex view of the area of rib design with various types and demonstrates the new solution possibilities for heat transfer using a numerical simulation software.

2. ANALYTICAL SOLUTION OF HEAT TRANSFER THROUGH EXTENDED SURFACES

Calculation methodology of thermal flows as well as temperature fields is based on a solution for various types of differential equations obtained from analysis of elementary changes concerning investigated values.

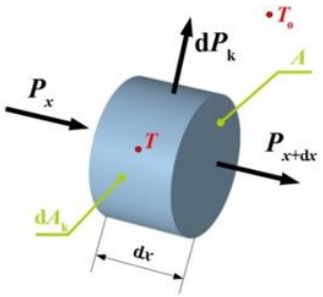

Fig. 1. Thermal flows on the simple rib element

Analytical solution of heat conduction equations is possible only in limited situations, whereas it is applied predominately for stationary one-dimensional heat conduction or for heat conduction with internal sources. More complex geometry volume bodies therefore use software tools based on numerical calcula-

DOI 10.1515/ama-2015-0013

tions that are far beyond the capabilities of analytical solutions (Stone et al., 2014; Kapjor et al., 2010; Brestovič et al., 2012). A principle of this method consists in a fact that the solution is not required for the whole investigated area, but only for finite number of strategically chosen points (parts of task).

It is necessary to take into consideration several assumptions for definition of temperature fields as well as for thermal flow along the rib length:

1. The heat conduction in the x-axis direction is one-dimensional and conduction perpendicular to the x-axis is neglected. Isothermal surfaces are perpendicular to the x-axis and their curvature is neglected.
2. The coefficient of heat transfer and the coefficient of thermal conductivity are constant along the whole rib surface.
3. The heat conduction is stationary and the temperature field is constant during time.

According to the thermal flows in the simple rib element, with regard to the law of energy conservation, it is evident that the sum of conductive thermal flow on the output of element and convection from external surface equals to the input of thermal flow to the element:

$$P_x = P_{x+\mathrm{d}x} + \mathrm{d}P_\mathrm{k} \qquad (\mathrm{W}) \tag{1}$$

Fourier law describes a thermal flow due to conduction by relation (Rohsenow et al., 1998; Incropera et al., 2007; Rajzinger, 2012):

$$P_x = -\lambda \cdot A \cdot \frac{\mathrm{d}T}{\mathrm{d}x} \qquad (\mathrm{W}) \tag{2}$$

where A is a cross-section area in distance x (m^2), λ – coefficient of thermal conductivity $(\mathrm{W}\cdot\mathrm{m}^{-1}\cdot\mathrm{K}^{-1})$. The conductive thermal flow in distance x + dx can be given as follows:

$$P_{x+\mathrm{d}x} = P_x + \frac{\partial P_x}{\partial x}\mathrm{d}x \qquad (\mathrm{W}) \tag{3}$$

Newton law of heat transfer by convection through the elementary surface dA_k, which is written in differential form, describes the thermal flow transferred into the surrounding during cooling:

$$\mathrm{d}P_\mathrm{k} = \alpha \cdot \mathrm{d}A_\mathrm{k} \cdot (T - T_\mathrm{o})\ (\mathrm{W}) \tag{4}$$

where α is heat transfer coefficient $(\mathrm{W}\cdot\mathrm{m}^{-2}\cdot\mathrm{K}^{-1})$, dA_k – elementary surface of rib participated in heat convection (m^2), T – thermodynamic temperature of the rib element with thickness dx (K), T_o – ambient thermodynamic temperature (K).

Joining the relations from (1) to (4) we obtain the relation for energy balance of the thermal flows in the form:

$$P_x = P_x + \frac{\partial\left(-\lambda\cdot A\cdot\frac{\mathrm{d}T}{\mathrm{d}x}\right)}{\partial x}\mathrm{d}x + \alpha\cdot\mathrm{d}A_\mathrm{k}\cdot(T - T_\mathrm{o}) \quad (\mathrm{W}) \tag{5}$$

After modification of this equation and using derivation relations we obtain the general differential equation, which describes the rib temperature fields as follows:

$$\frac{\mathrm{d}^2T}{\mathrm{d}x^2} + \frac{1}{A}\cdot\frac{\mathrm{d}A}{\mathrm{d}x}\cdot\frac{\mathrm{d}T}{\mathrm{d}x} - \frac{\alpha}{A\cdot\lambda}\cdot\frac{\mathrm{d}A_\mathrm{k}}{\mathrm{d}x}\cdot(T - T_\mathrm{o}) = 0 \tag{6}$$

After calculation of temperature behaviour in dependence on the rib length it is possible to obtain the conductive thermal flow in any distance x according to the relation (2).

Solving of differential equation is possible to perform if there are known geometric, physical and boundary conditions of explicitness (Oravec et al., 2010; Vranay, 2012). The simplest situation for analytic solution of equation is a planar rib with a constant cross-section area.

2.1. Equation of Energy for Extended Surfaces Considering Radiation

In case that the rib surface emissivity has not got a zero level (there is considered a grey body), it is necessary to determine the total thermal flow transferred through the rib considering its radiation as well. In the next chapter there is supposed a constant value of emissivity on the whole surface of a sole rib, whereas the ambient effective emissivity equals 1.

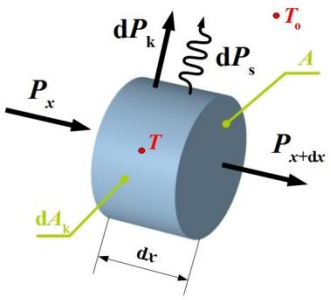

Fig. 2. Description of thermal flows on the simple rib element considering radiation

The equation of the thermal flow, the relation (1), is supplemented with the thermal flow caused by radiation into ambient:

$$P_x = P_{x+\mathrm{d}x} + \mathrm{d}P_\mathrm{k} + \mathrm{d}P_\mathrm{s} \qquad (\mathrm{W}) \tag{7}$$

Elementary radiated thermal flow dP_s transferred from the rib surface into ambient is determined according to the Stefan-Boltzmann Law:

$$\mathrm{d}P_\mathrm{s} = \varepsilon\cdot\sigma\cdot\mathrm{d}A_\mathrm{k}\cdot\left(T^4 - {T_\mathrm{o}}^4\right) \qquad (\mathrm{W}) \tag{8}$$

where σ is the Stefan-Boltzmann constant $(\mathrm{W}\cdot\mathrm{m}^{-2}\cdot\mathrm{K}^{-4})$, ε – the rib surface emissivity (-), and dA_k represents the elementary surface participating on the convention and radiation (m^2).

Using addition of the relations (7) and (8) and by means of mathematical modification we obtain the final non-linear differential equation of the second order, which describes a one-dimensional field of temperature in the rib, considering the radiation.

$$\frac{\mathrm{d}A}{\mathrm{d}x}\cdot\frac{\mathrm{d}T}{\mathrm{d}x} + A\frac{\mathrm{d}^2T}{\mathrm{d}x^2} - \frac{\alpha}{\lambda}\cdot\frac{\mathrm{d}A_\mathrm{k}}{\mathrm{d}x}\cdot\left(T - T_\mathrm{o}\right) - \frac{\varepsilon\cdot\sigma}{\lambda}\cdot\frac{\mathrm{d}A_\mathrm{k}}{\mathrm{d}x}\cdot \left(T^4 - {T_\mathrm{o}}^4\right) = 0 \tag{9}$$

In case of a planar rib with the constant cross-section the equation (9) can be simplified as follows:

$$\frac{\mathrm{d}^2T}{\mathrm{d}x^2} - \frac{\alpha}{\lambda}\cdot\frac{p}{A}\cdot\left(T - T_\mathrm{o}\right) - \frac{\varepsilon\cdot\sigma\cdot p}{\lambda}\cdot\left(T^4 - {T_\mathrm{o}}^4\right) = 0 \tag{10}$$

where p is the perimeter of the rib at a distance x from the base of rib (m).

In view of the problematic solution of these types of differential equations is more convenient to use iterative-numerical calculation using the energy balance of the rib element. To simplify the calculation in the next section is described a calculation procedure using FDM without considering the radiation.

3. APPLICATION OF FDM FOR CALCULATION OF THERMAL POWER OUTPUT AND FIELD OF TEMPERATURE FOR PLANAR RIBS

Determination of the temperature field along the rib height, considering radiation according to the equation (10), is complicated due to a solution of the non-linear differential equation of the second order. At the solution of equation, using the FDM, a set of differential equations is created with the polynomial of the 4th degree. Therefore, it is more suitable to solve the field of temperature using an iterative method with the basic equations describing the conduction and convection. A calculation of the rib temperatures with neglected radiation is realized through equation (6), whereas the first and the second derivations are overwritten by using the Taylor series in the following form (herewith the derivations of the higher order are neglected):

$$\frac{\mathrm{d}U}{\mathrm{d}x} = \frac{U_{i+1} - U_i}{\Delta x} \tag{11}$$

$$\frac{\mathrm{d}^2U}{\mathrm{d}x^2} = \frac{U_{i-1} - 2 \cdot U_i + U_{i+1}}{(\Delta x)^2} \tag{12}$$

where U is a general variable derivative along the x axis, U_i – is a variable in the i-th node, U_{i+1} – is a variable in the $(i+1)$ th node, U_{i-1} – is a variable in the $(i-1)$th node, Δx – is a length of the rib partition (m).

In general, it is possible to take into consideration a change of all the relevant quantities along the rib length. If the rib is divided into n equal elements, it is thus necessary to calculate the $n+1$ temperatures that are mutually dependent in the nodal points. With respect to the relations (11) and (12) we obtain a linear equation from the relation (6) in the form:

$$\frac{T_{i-1} - 2 \cdot T_i + T_{i+1}}{(\Delta x)^2} + \frac{1}{A_i} \cdot \frac{A_{i+1} - A_i}{\Delta x} \cdot \frac{T_{i+1} - T_i}{\Delta x} - \frac{\alpha_i \cdot p_i}{A_i \cdot \lambda_i} \cdot (T_i - T_\mathrm{o}) = 0 \tag{13}$$

Using a separation of the searched temperatures, the relation (13) is modified into the form:

$$T_{i-1} - \left[2 + \frac{A_{i+1} - A_i}{A_i} + \frac{\alpha_i \cdot p_i}{A_i \cdot \lambda_i} \cdot (\Delta x)^2\right] \cdot T_i + \left[1 + \frac{A_{i+1} - A_i}{A_i}\right] \cdot T_{i+1} = -\frac{\alpha_i \cdot p_i \cdot (\Delta x)^2}{A_i \cdot \lambda_i} \cdot T_\mathrm{o} \tag{14}$$

After introducing of a substitution for the coefficients, which are situated in front of the temperatures in the nodal points of the discretised rib, the new form of the relation is:

$$T_{i-1} + a_i \cdot T_i + b_i \cdot T_{i+1} = c_i \tag{15}$$

where a_i, b_i and c_i are constants created by means of the next substitution according to:

$$a_i = -\left[2 + \frac{A_{i+1} - A_i}{A_i} + \frac{\alpha_i \cdot p_i}{A_i \cdot \lambda_i} \cdot (\Delta x)^2\right] \tag{16}$$

$$b_i = 1 + \frac{A_{i+1} - A_i}{A_i} \tag{17}$$

$$c_i = -\frac{\alpha_i \cdot p_i \cdot (\Delta x)^2}{A_i \cdot \lambda_i} \cdot T_\mathrm{o} \tag{18}$$

Equation (15) describes the dependence among the temperature T_i in the i- th node and the temperatures T_{i-1} and T_{i+1} in the neighbouring points. The rib is divided into five elements of the same length according to Fig.3; thereby six nodal temperatures are defined. In order to calculate these temperatures it is necessary to assembly the same number of linear equations. Rib is divided into five elements only for purposes of calculation exemplification. Increase the number of partitions would naturally lead to increase in the accuracy of the calculation.

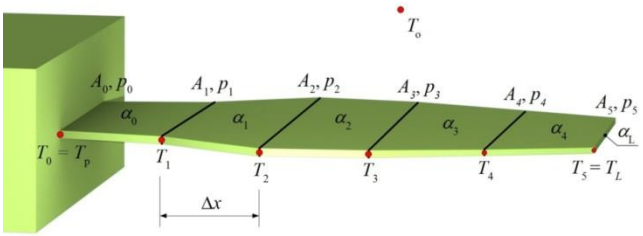

Fig. 3. Illustration of the dipartite rib for FDM

The equation (15) is valid for the nodal points from $i = 1$ to 4, which means the creation of an equation system with 4 ones. The other relations are given by the boundary conditions:

1. The temperature of the rib foot is known $T_0 = T_p = c_0$.
2. We consider convection at the rib end, whereas the thermal flow, caused by conduction at the rib end, equals to thermal flow due to convection from the rib end surface into ambient.

$$-\lambda \cdot \frac{T_5 - T_4}{\Delta x} = \alpha \cdot (T_5 - T_\mathrm{o}) \qquad (\mathrm{W \cdot m^{-2}}) \tag{19}$$

Modifying the relation (19) together with following substitution of constants we obtain a relation between the temperature T_4 and T_5 in the form:

$$\frac{\lambda}{\Delta x} \cdot T_4 - \left(\frac{\lambda}{\Delta x} + \alpha\right) \cdot T_5 = -\alpha \cdot T_\mathrm{o} \qquad (\mathrm{W \cdot m^{-2}}) \tag{20}$$

$$d \cdot T_4 + e \cdot T_5 = c_5 \qquad (\mathrm{W \cdot m^{-2}}) \tag{21}$$

where d and e are the substitution of constants of equation (20).

The system of 6 linear equations can be described in a matrix form:

$$|a| \cdot |T| = |c| \tag{22}$$

$$\begin{vmatrix} 1 & 0 & 0 & 0 & 0 & 0 \\ 1 & a_1 & b_1 & 0 & 0 & 0 \\ 0 & 1 & a_2 & b_2 & 0 & 0 \\ 0 & 0 & 1 & a_3 & b_3 & 0 \\ 0 & 0 & 0 & 1 & a_4 & b_4 \\ 0 & 0 & 0 & 0 & d & e \end{vmatrix} \cdot \begin{vmatrix} T_0 \\ T_1 \\ T_2 \\ T_3 \\ T_4 \\ T_5 \end{vmatrix} = \begin{vmatrix} c_0 \\ c_1 \\ c_2 \\ c_3 \\ c_4 \\ c_5 \end{vmatrix} \tag{23}$$

A solution of the equation system roots can be found for example by means of an inverse matrix method:

$$|T| = |a|^{-1} \cdot |c| \tag{24}$$

A calculation example is realised on the planar rib with the length $50\ \mathrm{mm}$, the thickness $2\ \mathrm{mm}$, the width $100\ \mathrm{mm}$ and the thermal conductivity $\lambda = 55\ \mathrm{W \cdot m^{-1} \cdot K^{-1}}$.

The coefficient of heat transfer of the rib surface is $\alpha = 45\ \mathrm{W \cdot m^{-2} \cdot K^{-1}}$, the temperature of surrounding liquid is $T_0 = 20\ °C$ and the rib partition is $\Delta x = 0.01\ \mathrm{m}$.

The solution result of temperature field is a matrix in the form:

$$|T| = \begin{vmatrix} 50.00 \\ 43.65 \\ 39.28 \\ 36.52 \\ 35.13 \\ 35.01 \end{vmatrix} \qquad (°\mathrm{C}) \tag{25}$$

DOI 10.1515/ama-2015-0013

In Fig. 4 there is illustrated a comparison of resulting temperature in the nodal points of rib determined by FDM and an analytic solution.

The temperature behaviours along the rib length have got an equal character; however, the low level of rib discretisation by means of large distances Δx causes a relevant failure of the calculation using FDM in comparison to an analytic solution.

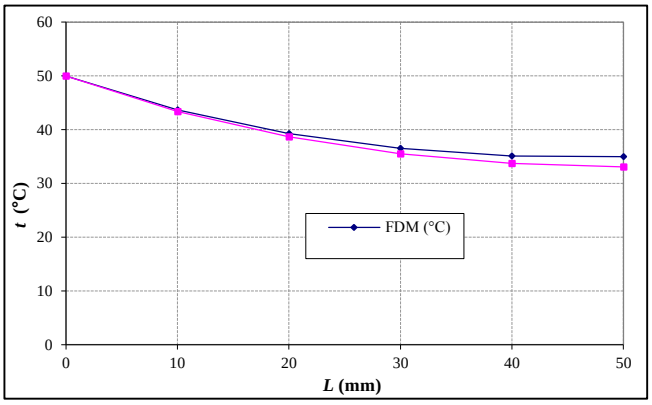

Fig. 4. Behaviour of temperatures along the rib length determined by analytic technique (analytical solution of the equation (6) for planar rib) and by FDM

Calculation deviation considering the actual situation of the rib is $5.84\ \%$, whereas if one-dimensional network on the rib surface is more compacted, the calculation deviation decreases.

3.1. Application of FDM for Calculation of Cylindrical Ribs

It is more suitable to apply numerical methods for a solution of temperature fields as well as for a solution of the total thermal flow removed through the rib with regard to a complicity and slowness of the analytical solution. Software support for a solution of the cooling power output can be created by a proper implementation of the mathematical methods. Such application is useful predominately in the case of coolers (Čarnogurská et al., 2013, Kapalo, 2005).

The analytical solution is too complicated for a design of quick and easy calculation software. Therefore, it was chosen a calculation method, which is based on FDM application. In this case the cylindrical rib is divided along the height into the N coaxial cylindrical elements. This solution was applied assuming that isothermal surfaces have got a cylindrical shape, although in the case of a real cooler the temperature field is deformed due to gradual air heating along the rib height as well as due to an unequal distribution for the velocity field of cooling air (Fig. 5).

The Fourier law in the differential form describes a conductive heat transfer through a rib and it can be transferred into a difference form according to the equation (27) for a very small change of the radius.

At the numerical method there is used a substitution of the differential equation of the first order by a difference equation (with an application of Taylor series neglecting the second and higher derivations) (Michalec et al., 2010, Nagy et al., 2012, Urban et al., 2012). A requirement for solution by means of FDM is to keep the same division of the radius r during task discretisation, i.e.:

$$\frac{\mathrm{d}t}{\mathrm{d}r} = \frac{T_{i+1} - T_i}{r_{i+1} - r_i} \qquad (\mathrm{K \cdot m^{-1}}) \tag{26}$$

Then:

$$P[i] = -2 \cdot \pi \cdot r_i \cdot \delta \cdot \lambda \cdot \frac{T_{i+1} - T_i}{r_{i+1} - r_i} \quad (\mathrm{W}) \tag{27}$$

where: r is the internal radius of the i-th element (m), r_{i+1} is the external radius of the i-th element (m), T_i is the temperature of the i-th element (K), and T_{i+1} is the temperature of the $(i+1)$-th element (K).

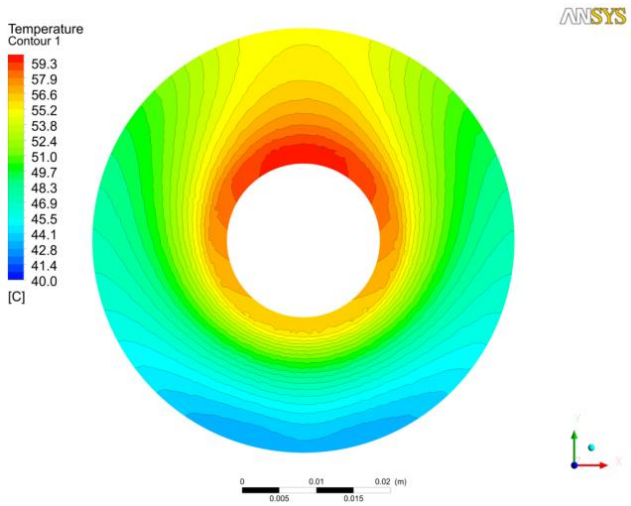

Fig. 5. Temperature field on the rib during flowing of the cooling liquid in y-axis direction

The Newton law describes a heat transfer from a rib surface into the air:

$$P_{\mathrm{k}}[i] = \alpha \cdot (T_i - T_{\mathrm{o}}) \cdot \pi \cdot (r_{i+1}^2 - r_i^2) \qquad (\mathrm{W}) \tag{28}$$

where T_{o} is the cooling air temperature (K).

The relation (29) describes the conductive thermal flow entering the next $[i+1]$-th element, whereas the calculation has to fulfil the basic boundary conditions:

$$P[i+1] = P[i] - 2 \cdot P_{\mathrm{k}}[i] \qquad (\mathrm{W}) \tag{29}$$

The 1st boundary condition: $r[0] = r_1 \Rightarrow t[0] = t_{\mathrm{p}}$. The 2nd boundary condition: $P_{\mathrm{k}}[N] = 2 \cdot \alpha \cdot \pi \cdot r_2 \cdot \delta \cdot (T_N - T_{\mathrm{air}})$ (convection at the rib end), where TN is a temperature of the boundary N-th element (K), T_{air} – temperature of the surrounding fluid medium (K).

It is necessary to estimate the thermal flow as accurately as possible for the first iteration at the rib foot in order to accelerate the iterative calculation.

This requirement can be obtained by a calculation of the planar rib with the constant cross-section, whereas a rib cross-section and a rib circumference is considered at the middle radius of the cylindrical rib:

$$_1P[0] = \sqrt{\alpha \cdot \lambda \cdot p_{\mathrm{avg}} \cdot A_{\mathrm{avg}}} \cdot (T_{\mathrm{o}} - T_{\mathrm{vz}}) \cdot \tanh\left[\sqrt{\frac{\alpha}{\lambda} \cdot \frac{p_{\mathrm{avg}}}{A_{\mathrm{avg}}}} \cdot (r_2 - r_1)\right] \qquad (\mathrm{W}) \tag{30}$$

where: p_{avg} is the perimeter of the planar rib corresponding to the mean radius of the cylindrical rib (m), A_{avg} is a cross-sectional area on the mean radius of the rib (m^2).

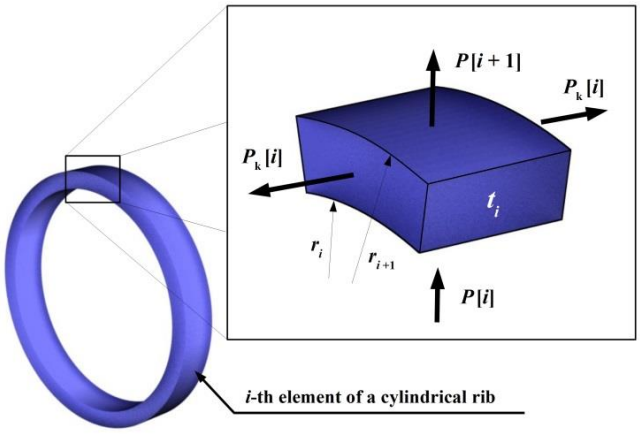

Fig. 6. Thermal flows in the element of a cylindrical rib

The calculation is performed iteratively; at the end of each individual iteration it is necessary to change an initial conductive thermal flow at the rib foot $P_{\mathrm{k}}[0]$ so that the boundary condition No. 2 will be reached. For this purpose there was suggested an iterative condition. During application of this condition it was investigated that its calculation is still converging to the required real value:

$$_{j+1}P[0] = {}_{j}P[0] - \frac{{}_{j}P[N]}{10} \quad \text{(W)} \qquad (31)$$

where: ${}_{j}P[0]$ – is the thermal conductive flow at the rib input for the j-th iteration (W), ${}_{j+1}P[0]$ – is the thermal conductive flow at the rib input for the $(j+1)$-th iteration, and ${}_{j}P[N]$ – is the thermal flow at the external rib radius for j-th iteration (W).

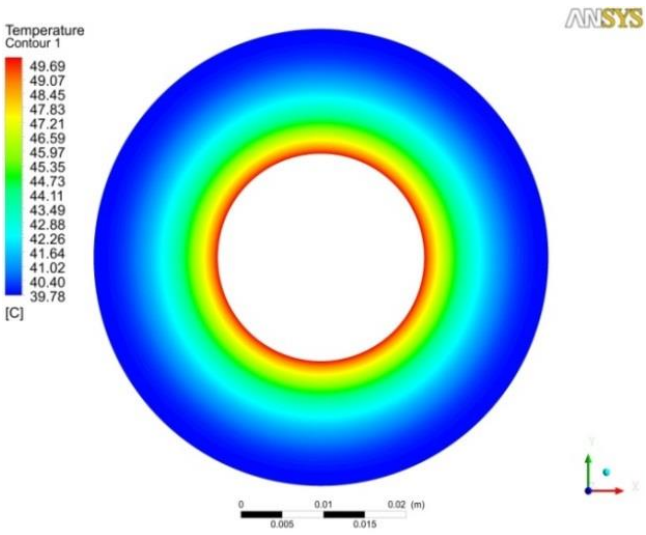

Fig. 7. Temperature field on a cylindrical rib of the natural gas cooler CH_R (ANSYS CFX)

The results of calculation obtained by means of the above-mentioned method were compared using the simulation tool ANSYS CFX (Fig. 8) for the same boundary conditions:

1. The rib foot temperature: 50 °C.
2. The coefficient of heat transfer on the rib: $45\ \mathrm{W} \cdot \mathrm{m}^{-2} \cdot \mathrm{K}^{-1}$ (at ambient air temperature 20 °C).

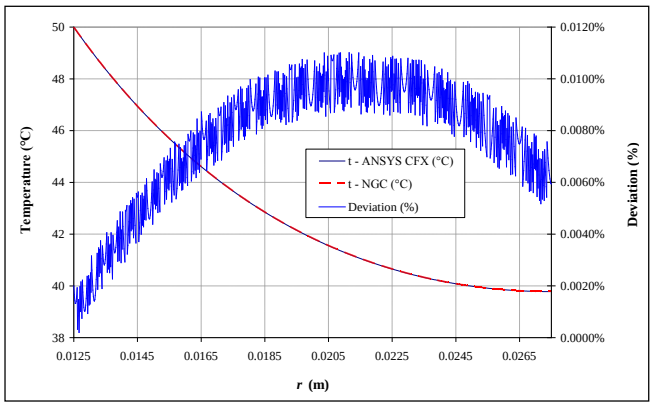

Fig. 8. A comparison of the temperature behaviours along the rib height obtained with various numerical tools

The deviations of the temperature behaviours along the rib height are up to the maximum value 0.015 % (Fig. 8). These temperature behaviours can be obtained either by the numerical calculation, which is performed by the newly developed software NGC (Natural Gas Cooler) or by the commerce software ANSYS CFX.

4. APPLICATION OF ANALYTICAL SOLUTION CONCERNING PLANAR RIBS FOR CURVED RIBS

The analytical and numerical calculation of the planar and cylindrical ribs was realised providing one-dimensional stationary heat conducting. In practical applications there is heat conducted through extended surfaces with a constant cross-section, whereas the centre of gravity for a surface, which conductive thermal flow is passing through, often creates a general curve. Therefore, it is not possible to consider the planar ribs. However, there is an advantageous possibility to apply mathematical functionalities deduced for the planar ribs. A typical example of a curved body is a handle of a fire stove specified for dendromass combustion, (Fig. 9). Although this handle does not fulfil a rib function, the thermal flow, which is passing through it, can be solved by means of assumptions valid for the planar ribs.

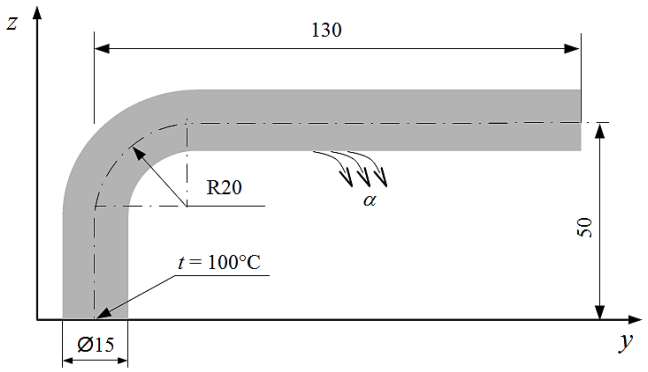

Fig. 9. The geometrical and thermal boundary conditions of the handle

A suitability of the assumption for calculation of the curved ribs with the constant cross-section was verified by a comparison. This comparison was realized between the analytical calculation of the rib end temperature considering the total thermal flow and the second calculation, which was fulfilled using finite volume method

DOI 10.1515/ama-2015-0013

(FVM) in ANSYS CFX.

The rib foot temperature is $100°C$, the ambient air temperature is $25°C$ and the end of the handle is adiabatically insulated.

A gravity point axis of the cross-section surface is situated horizontally. The heat transfer coefficient $\alpha = 8.844\ \mathrm{W \cdot m^{-2} \cdot K^{-1}}$ is determined by means of the criterion equations that are valid for heat transfer during free convection and by the known geometrical and physical characteristics of the handle and ambient air.

The HTC (Heat Transfer Coefficient) software was developed in order to quicken a calculation of the heat transfer coefficient. There is considered the rib thermal conductivity value of $60.5\ \mathrm{W \cdot m^{-1} \cdot K^{-1}}$ and the surface emissivity value $\varepsilon \approx 0$ (this assumption is correct for a chromium-plated surface).

After the solution and modification of the equation (6) we obtain a calculating relation of the handle end temperature in the form:

$$T_L = T_o + (T_p - T_o) \cdot \frac{1}{\cosh(m \cdot L)} \quad (°C) \qquad (32)$$

where m is the substitution of constants resulting from the analytical solution of the differential equation for the extended area $\sqrt{\frac{\alpha}{\lambda} \cdot \frac{p}{A}}\ (\mathrm{m^{-1}})$, L - length of the rib (m).

The analytical calculation, performed according to the relation (32), determines the temperature value $T_L = 71.026\ °C$. After a solution of the equation (6) with applying the Fourier's law, there is the value level of thermal flow, which is removed through the handle, $P_r = 3.953\ \mathrm{W}$. As well using ANSYS CFX a calculation was performed in order to compare the obtained results.

The calculated rib end temperature was $T_{L-ANSYS} = 71.148\ °C$ and the total thermal flow was $P_{r-ANSYS} = 3.956\ \mathrm{W}$. The percentage deviation between the analytical calculation and FVM is $\Delta_T = 0.17\%$ for the temperature values and the percentage deviation for the thermal flow is $\Delta_P = 0.076\ \%$. It is evident, with regard to the above-mentioned deviations, that the applied assumptions are correct for an analytical calculation of the planar ribs. In Fig. 10 there are illustrated the isothermal surfaces of the handle cross-section calculated in ANSYS CFX.

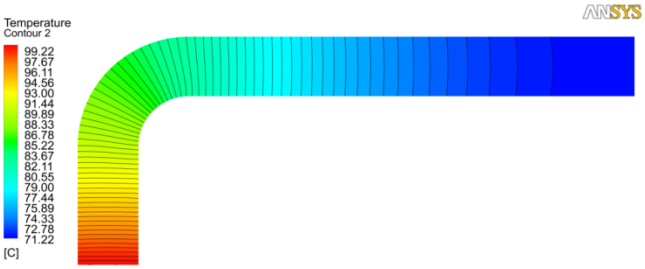

Fig. 10. Thermal field in the plane passing through a middle of handgrip handle

The calculation demonstrates a fact that the isothermal surfaces are not curved in the location of the bar deflection. This fact is favourable for an assumption of an analytical calculation of heat transfer because an increase of convective thermal flow on the external radius is compensated by a reduction of the thermal flow on the internal surface of the handle curvature.

An evaluation of a curvature impact on accuracy of the analytical calculation for a thermal flow passing through a planar rib was realised also for another type of geometry by means of the simulation tool ANSYS CFX. Another geometry consisted from one thread of a helix with such curvature radius, which equals to the pitch $R = h = 50\ \mathrm{mm}$. After a planar rollout of the helix a right triangle is created with the side value $2 \cdot \pi \cdot R$ and the pitch h.

The hypotenuse of this triangle represents a length L of a spatial curve, which passes through the middle of a helix profile.

$$L = \sqrt{(2 \cdot \pi \cdot R)^2 + h^2} \quad (\mathrm{m}) \qquad (33)$$

The equivalent thermal flow of the planar rib, which is made from aluminium, will be solved according to the equation (6) for this geometry with the length L and for the adiabatic rib end. The value of rib heat conductivity is considered $\lambda = 237\ \mathrm{W \cdot m^{-1} \cdot K^{-1}}$ and the heat transfer coefficient value is $\alpha = 50\ \mathrm{W \cdot m^{-2} \cdot K^{-1}}$ at the ambient temperature $20°C$. The defined rib foot boundary condition of the first type is $t_p = 50\ °C$.

The cross-sectional area of a profile is a cyclic one with the diameter d. A change of this diameter causes a change of the ratio R/d as well. The calculation was performed for the ratio values $R/d = 20$ (Fig. 11), $R/d = 10$ (Fig. 12), $R/d = 5$ (Fig. 13), $R/d = 3$ (Fig. 14), $R/d = 1.5$ (Fig. 15) and $R/d = 1$ (Fig. 16).

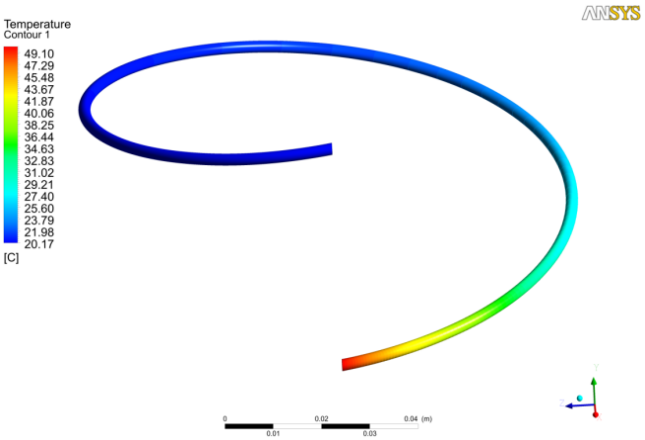

Fig. 11. Surface temperature field of curved bar with the ratio $R/d = 20$

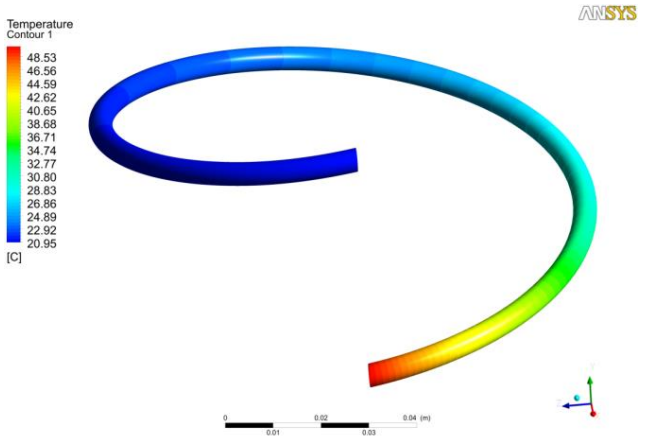

Fig. 12. Surface temperature field of curved bar with the ratio $R/d = 10$

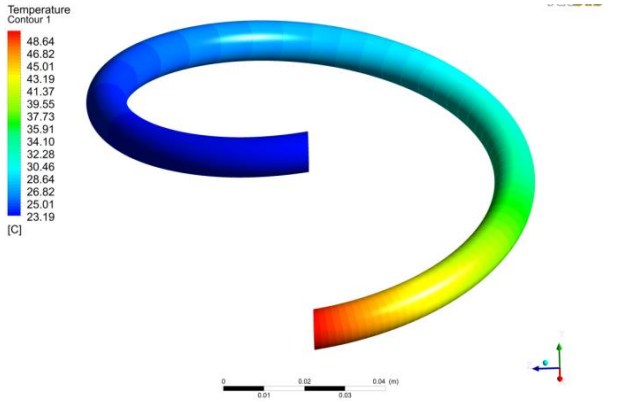

Fig. 13. Surface temperature field of curved bar with the ratio $R/d = 5$

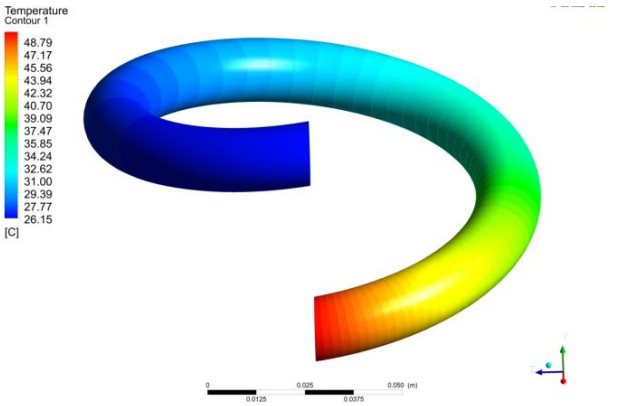

Fig. 14. Surface temperature field of curved bar with the ratio $R/d = 3$

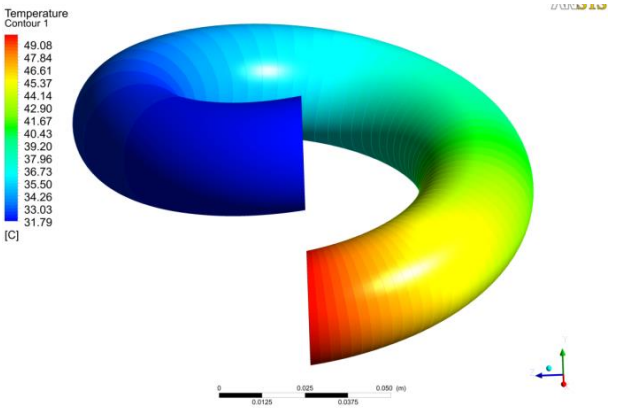

Fig. 15. Surface temperature field of curved bar with the ratio $R/d = 1.5$

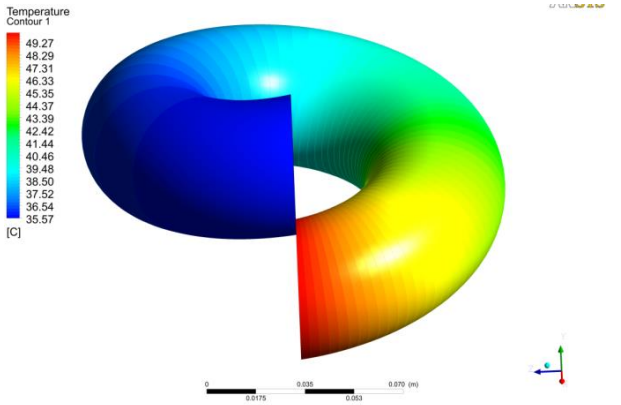

Fig. 16. Surface temperature field of curved bar with the ratio $R/d = 1$

Tab.1 presents a comparison of the total thermal flow values P_r obtained by means of the analytical calculation and the values $P_{r-ANSYS}$, which are resulting from the calculation using the software ANSYS CFX. In this table there are also recorded the calculating deviations corresponding to the both methods.

Tab. 1. Comparison between the analytical calculation and the calculation using FVM

R/d $(-)$	P_r (W)	$P_{r-ANSYS}$ (W)	Calculating Deviation (%)
20	0.641	0.634	1.147
10	1.813	1.790	1.269
5	5.100	5.057	0.847
3	10.801	10.707	0.865
1.5	28.776	28.797	-0.070
1	49.523	50.025	-1.012

A deviation of the both calculation methods does not overreach the value of $1.269\ \%$. So it can be concluded that the above-mentioned method, which substitutes a curved rib calculation by a calculation of planar rib, is a suitable procedure. An inaccuracy of the calculation can be also caused due to the object discretisation by means of FVM.

5. CALCULATION OF POWER OUTPUT FOR FLAT SQUARED RIBS

A heat conduction of flat squared ribs is a two-dimensional process and, as a result, the isothermal surfaces are “deformed” predominately on the external rib side. (Fig.18). Comparison of the temperature fields, for a cylindrical rib and a squared rib, demonstrates a fact that the temperature field is similar in such area where the temperature difference between a surface and surrounding is maximal (on an internal diameter).

The squared rib temperature field is deforming with an increasing distance of a rib element from the central axis. In these areas the surface temperature is lower. An influence of thermal isotherm deformations (curvature) on the total thermal flow, which is determined by an analytical solution of cylindrical ribs, is neglecting in the case of a procedure applied for the squared ribs.

This consideration is verified by a numerical calculation of squared ribs using ANSYS CFX and by a calculation of cylindrical ribs using the own software (FDM). The numerical calculation of cylindrical ribs was also performed in ANSYS CFX in order to compare the temperature fields.

A substitution of squared ribs by cylindrical ribs is possible only on a condition that the frontal surface is the same.

As well as the internal diameter d is identical in both cases. The relation between the square side length and an external diameter of cylindrical rib is given:

$$a = \sqrt{\pi} \cdot \frac{D}{2} \qquad (\mathrm{m}) \tag{34}$$

where a is a square side length (m), d is an internal diameter of rib (m), and D is an external diameter of the cylindrical rib (m).

Various ratio values of diameters D/d were investigated in order to evaluate a suitability of the above-mentioned assumptions. The ratios D/d are corresponding with an adequate ratio value a/d according to the relation (34). A simulation calculation

DOI 10.1515/ama-2015-0013

of a temperature field for a cylindrical rib with the ratio $D/d = 2$ is illustrated in the Fig. 17.

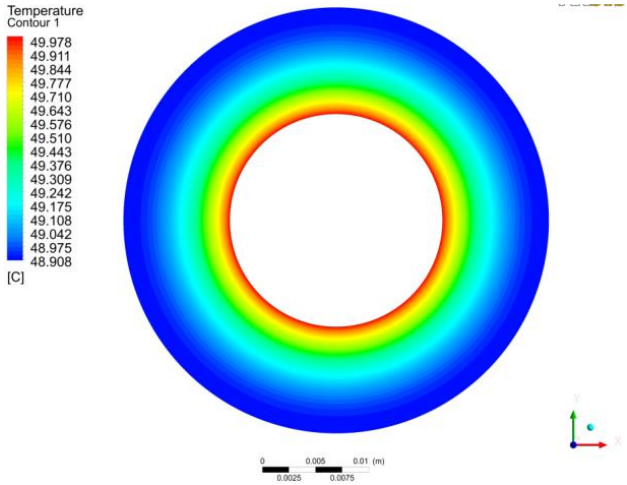

Fig. 17. Temperature field of a cylindrical rib with the ratio of diameters $D/d = 2$

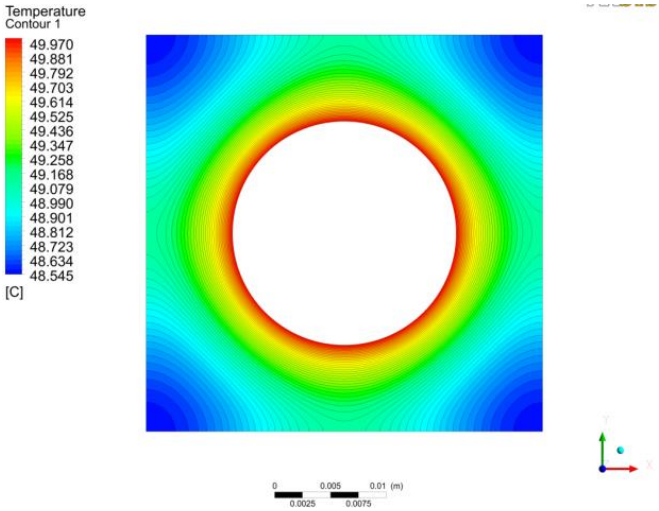

Fig. 18. Temperature field of a squared rib corresponding to the ratio $D/d = 2$

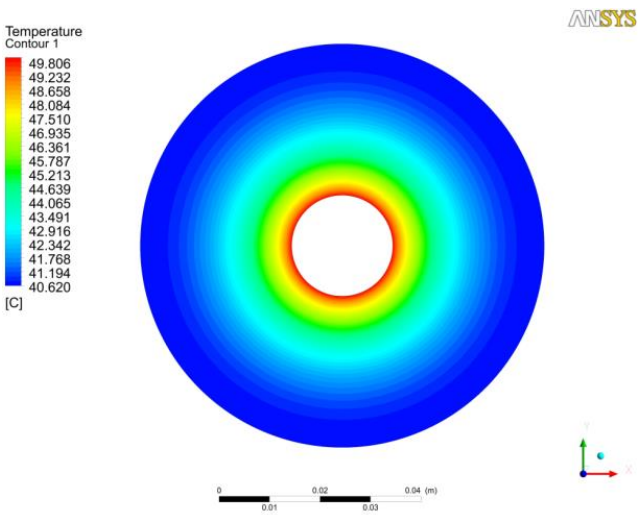

Fig. 19. Temperature field of a cylindrical rib with the ratio of diameters $D/d = 4$

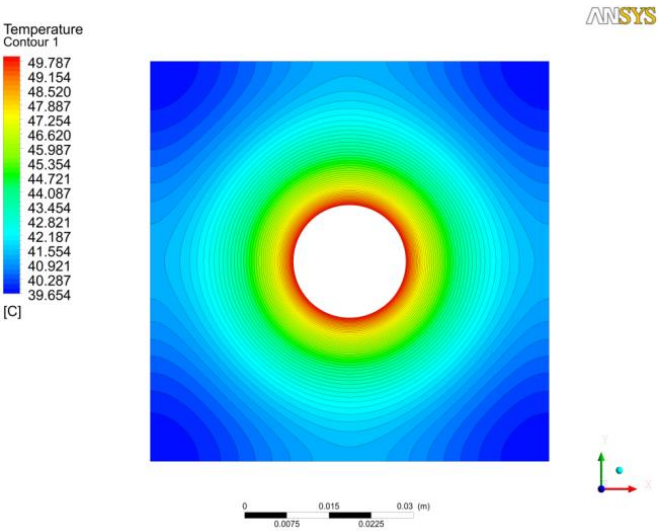

Fig. 20. Temperature field of a squared rib corresponding to the ratio $D/d = 4$

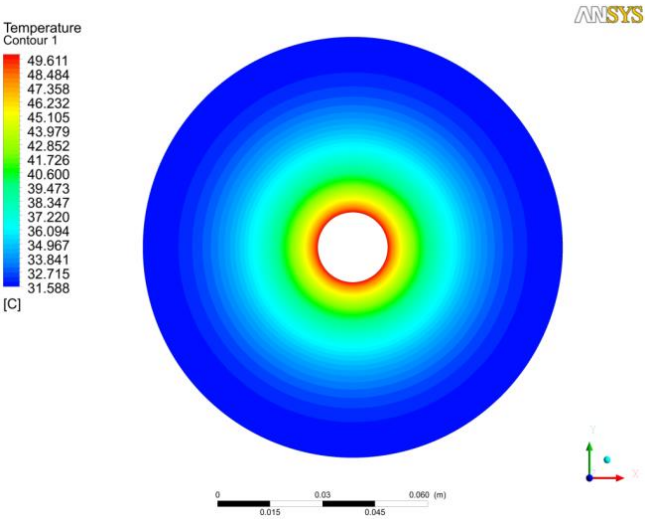

Fig. 21. Temperature field of a cylindrical rib with the ratio of diameters $D/d = 6$

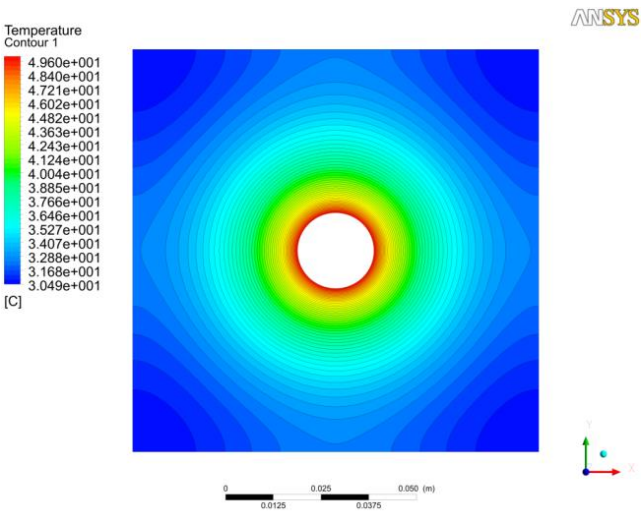

Fig. 22. Temperature field of a squared rib corresponding to the ratio $D/d = 6$

There is the corresponding ratio $a/d = 1.772$ for the squared rib (Fig. 18). The next figures from the Fig. 19 to the Fig. 22 illustrate the temperature contours for the ratios $D/d = 4$ and $D/d = 6$.

The value of rib heat conductivity is considered $\lambda = 237\ \mathrm{W \cdot m^{-1} \cdot K^{-1}}$ and the heat transfer coefficient value is $\alpha = 35\ \mathrm{W \cdot m^{-2} \cdot K^{-1}}$ at the ambient temperature $20\ °\mathrm{C}$. The defined rib foot boundary condition of the first type is $t_p = 50\ °\mathrm{C}$. In the Tab. 2 there is presented comparison of the total thermal flow removed through a cooling cylindrical rib and a squared rib. The cylindrical rib was calculated using the own developed software, which applies the finite difference method FDM.

Tab. 2. The comparison of an analytical calculation with a ANSYS CFX calculation

D/d $(-)$	Squared rib P_r (W)	Cylindrical rib P_r (W)	Calculating deviation (%)
2	1.922	1.926	-0.179
4	7.345	7.373	-0.388
6	10.972	11.017	-0.411

An application suitability of an analytical calculation for thermal flow, which is removed through a cylindrical rib, for a calculation of a flat squared rib was verified on the basis of relatively small calculating deviations of power output values in comparison to the simulations performed in ANSYS CFX.

A gradual rising of deviation absolute values in a calculation process is caused due to a substitution of a cylindrical rib by a squared rib. Both ribs have got the same frontal surface area. This fact causes a rising of distance between the rib axis and the square edge in comparison to the width of a cylindrical rib. However, the rising distance also causes a decrease of surface temperature and in this way the total thermal flow is reduced, which is transferred by convection into environment.

6. CONCLUSIONS

This article is focused on the methodology, which is specified for a design of planar and cylindrical ribs using analytical and a numerical method. Application of an analytical calculation is possible predominately in the case of simpler geometrical shapes and also for simpler accepted boundary conditions.

Numerical methods are suitable especially for more complicated geometrical shapes and for a creation of a functional dependence among the relevant values and temperatures. In such situations there are applied more difficult differential equations that are used for a solution of heat transfer through ribs.

The mostly used method for a solution of the above-mentioned problems is the method of finite differences. This method is a base for the newly developed software tools specified for a calculation of the ribbed surfaces.

In this article there were also described procedures that enable to re-transform the multi-dimensional tasks of the heat transfer through ribs into the one-dimensional tasks.

The main objective for investigation of a transformation possibility of the multi-dimensional tasks into the one-dimensional task is to find simpler tools. Those tools would provide results that are comparable with the results obtained by using various commercial tools, which may not be available for every user.

REFERENCES

1. **Brestovič T., Jasminská N.** (2013), Software support development for numerical solution of Ansys CFX, *Acta Mechanica et Automatica*. Vol. 7, no. 4, 215-221.
2. **Brestovič T., Kubík M., Jasminská N.** (2012), Use of numerical methods for determining the coefficients of pressure losses (in Slovak), *Plynár-Vodár-Kúrenár + Klimatizácia*, Vol. 10, č. 2, 46-47.
3. **Čarnogurská M., Příhoda M., Kubík M., Gállik R., Hršák D.** (2013), Methodology of the Sediment Thickness Calculation on the Heat Exchange Area of a Coolers Natural Gas, *International Journal of Mechanic Systems Engieneering*, Vol. 3, no. 1, 14-19.
4. **Ferstl K.**, **Masaryk M.** (2011), *Heat transfer* (in Slovak), STU Bratislava.
5. **Incropera F. P. et al.** (2007), *Fundamentals of Heat and Mass Transfer*, Publisher John Wiley & Sons.
6. **Kapalo P**. (2005), The effect of the flow rate of hot water to the heat flow through the pipe wall (in Slovak), *TZB*, Vol. 13, No. 3, 22-24.
7. **Kapjor A., Jandačka J., Malcho M., Papučík Š.** (2010), Intensification of Heat Transport from the Floor Convector at Given Geometry and the Way of Use, *Meeting´s of the department of fluid mechanics and thermodynamics – International Conference*, 101 - 104.
8. **Maga D., Harťanský R.** (2005), *Numerical solutions* (in Slovak), Brno.
9. **Michalec Z.**, **Taraba B., Bojko M., Kozubková M.** (2010), CFD modelling of the low-temperature oxidation of coal, *Archivum Combustions*, Vol. 30, No. 3, 133-144.
10. **Mlynár P.**, **Masaryk M.** (2012), Optimalization of absortioption cooling unit, Gépeszet 2012, *8th International conference of Mechanical Engineering*, BME Budapest, 361-365.
11. **Nagy R., Košičanová, D.** (2012), Indoor environment air quality ventilation rates – numerical CFD simulations calculations and measuring apparatus applications, *Czasopismo Techniczne*, 109 (3), 2012, 281–295.
12. **Oravec M., Števo S., Sekaj I.** (2010),Comparison of Using Simple Genetic Algorithm and Parallel Genetic Algorithm in Heat Transfer Model Optimization, *Journal of Cybernetics and Informatics*, Vol. 9, 13-18.
13. **Purcz P.** (2001), Parallel algorithm for spatially one- and two-dimensional initial-boundary-value problem for a parabolic eauation, *Kybernetika*, Vol. 37, No. 2, 171-181.
14. **Pyszko R.**, **Příhoda M., Velička M.** (2010), Method for determining the thermal boundary condition in the CC mould for numeric models, *Proceedings of 19. conference METAL 2010*, Ostrava.
15. **Rajzinger J.** (2012), Calculation of maximum water content in various natural gases by using modified Peng-Robinson equation of state, *Communications*, Vol. 14, No. 4A, 29-35.
16. **Rohsenow W. M., Hartnett J. P., Cho Y. I.** (1998), *Handbook of Heat Transfer*, McGraw-Hill, 250-257
17. **Stone C., Simiček J., Vranay F.** (2014), Assessing the Thermal Stability of Rammed Earth Using Finite Element Methods, Progressive Multifunctional Building Materials, *Constructions and Technological Methods - One Step Closer to Green Visegrad in V4 Countries* – Kosice, 107-118.
18. **Urban F., Kučák Ľ., Bereznai J., Pulmann M., Tihányi J.** (2012), Influence of the mixing grid position on the coolant flow at the outflow part of the nuclear reactor fuel assembly physical model and validation of CFD model, *Communications*, Vol. 14, No. 4A (2012), 42-46.
19. **Vranay F.** (2012), Hydraulic connection with the use of existing heating distribution for cooling) (in Slovak), Vykurovanie, 499-503.

This paper was written with the financial support of the granting agency VEGA of the Ministry of Education of the Slovak Republic within the project solution No. 1/0686/13 and of the granting agency KEGA of the Ministry of Education of the Slovak Republic within the project solution No.041TUKE-4/2013.

DOI 10.1515/ama-2015-0014

FRICTION-INDUCED OSCILLATIONS OF A NON-ASBESTOS ORGANIC PIN SLIDING ON A STEEL DISC

Oleksii NOSKO[*], Takuo NAGAMINE[**], Hiroki MORI[***], Yuichi SATO[**]

[*]Department of Machine Design, KTH Royal Institute of Technology, Brinellvägen 83, Stockholm 100 44, Sweden
[**]Department of Mechanical Engineering, Saitama University, 255 Shimookubo, Sakura Ward, Saitama City 338 8570, Japan
[***]Department of Mechanical Engineering, Kyushu University, 744 Motooka, Nishi Ward, Fukuoka City 819 0395, Japan

nosko@dr.com, nagamine@mech.saitama-u.ac.jp, hiroki@mech.kyushu-u.ac.jp, ysato@mail.saitama-u.ac.jp

received 30 March 2015, revised 18 July 2015, accepted 20 July 2015

Abstract: Friction-induced oscillations result in deterioration of performance of disc brakes and are generally undesired. We conduct experimental study of friction-induced oscillations in a non-asbestos organic material / steel pair used in disc brakes of motor vehicles. The tests are done by use of a pin-on-disc machine in which the pin sample is supported on a deformable beam. The adjustable friction parameters are the disc velocity, contact pressure and temperature. The tests show that the friction coefficient decreases with the sliding velocity and increases with the temperature. The friction-induced tangential oscillation of the pin sample occurs with a frequency equal to the first natural frequency of the beam. The effects of the disc velocity and temperature on the oscillation characteristics are investigated. The oscillation amplitude increases with the disc velocity on the interval of velocities below 2 m/s. Temperature changes of several tens of degrees Celsius lead to the oscillation occurrence / decay. The obtained results can be useful for prognostication of friction-induced oscillations in disc brakes with non-asbestos organic pads.

Key words: Friction-Induced Oscillation, Pin-On-Disc Machine, Non-Asbestos Organic Material, Sliding Velocity, Temperature

1. INTRODUCTION

Friction-induced oscillation is a common phenomenon observed in various tribosystems. It is usually accompanied by uncontrollable changes in the sliding velocity, contact pressure, displacements or stress-and-strain states of the sliding components and generally results in deterioration of performance characteristics (Sheng, 2008).

Disc brakes are tribosystems widely utilized in automobiles, motorcycles, lift-and-transport machines, rail vehicles and aircrafts. The occurrence of friction-induced oscillations essentially reduces the reliability of disc brakes and quality of braking. In addition, these oscillations are the source of undesired noise. Therefore, prognostication and prevention of friction-induced oscillations at the design stage is one of the most challenging problems in the disc brake industry (Kinkaid et al., 2003; Sergienko et al., 2008).

A number of experimental and theoretical studies have been reported on the oscillatory dynamics in disc brake systems. One can distinguish several central theories describing the occurrence conditions and features of friction-induced oscillations. It is known that if the friction coefficient decreases with the sliding velocity, this results in the negative damping and associated oscillations (Kajdanowsky and Haykin, 1933; Mills, 1938). The difference between the kinetic friction force and the maximum tangential force in static contact is the reason for the excitation of stick−slip oscillations. This difference is explained by welding together of the sliding metallic materials at the local points of contact (Bowden and Leben, 1939) or strengthening of the interfacial bonds between the materials with the static contact duration (Ishlinsky and Kragelsky, 1944). The sliding instability in the form of oscillations is also possible under constant friction coefficient. It can occur due to the sprag–slip mechanism when geometrically or kinematically constrained sliding component becomes locked and then returns to the sliding state again through the pliability of the system (Spurr, 1961), thermoelastic distortion of the sliding components (Barber, 1969), self-excited elastic waves at the contact surfaces (Adams, 1995), etc.

The diversity of observations of tribosystem dynamics suggests that there is no simple and unique cause of friction-induced oscillations. The occurrence of oscillation and its features depend on the friction pair materials, friction conditions as well as characteristics of the whole tribosystem. One of the methods of experimental study of friction-induced oscillations is using a pin-on-disc machine with the pin sample mounted on a deformable support. This method allows to substitute the complicated multicomponent tribosystem under study with a simpler tribosystem with adjustable stiffness coefficients, natural frequencies and other parameters. Thereby, one can concentrate more deeply on friction-related phenomena.

Earles and Lee (1976) investigated oscillations in a steel / steel sliding contact with the aid of a pin-on-disc machine in which the pin was supported on a deformable cantilever. The construction of the cantilever allowed for the tangential and normal motions of the pin with respect to the sliding interface and its rotation related to the cantilever torsion. Another pin-on-disc machine was used by Aronov et al. (1983) for studying oscillations in a steel / steel sliding pair in the presence of water lubricant. The pin was supported on a deformable arm. The motions of the pin in the tangential and normal directions were measured by an accelerometer. Dweib and D'Souza (1990) modified the pin-on-disc machine of Aronov et al. so that the angle of the arm torsion could

be measured. Tworzydlo et al. (1999) developed a pin-on-disc machine with the pin connected by a deformable arm to a slider block which, in its turn, was supported on another deformable arm. The 3 translations and 3 rotations of the slider block were measured by 6 accelerometers.

In the present study we investigate experimentally the sliding instability in a non-asbestos organic material / steel pair used in disc brakes of motor vehicles. The tests are conducted by use of a pin-on-disc machine with the pin sample supported on a deformable beam. A special attention is paid to the effects of the disc velocity and temperature.

2. EXPERIMENTAL EQUIPMENT

Fig. 1 shows a schematic of a pin-on-disc machine developed (Nosko, 2013). The pin sample has a cross-section area S =10×10 mm². It is installed into a holder which is attached to a lever by use of a beam. The holder and beam are carefully levelled. The lever can rotate about a vertical axis. The friction disc is machined with high precision to eliminate waviness and distortion of the sliding surface. It is mounted on a horizontally installed shaft together with an inertia disc. A motor drives the shaft and, accordingly, the friction disc with an angular velocity ω. The pin sample is pressed against the friction disc with a normal force N. The average friction radius is r = 35 mm.

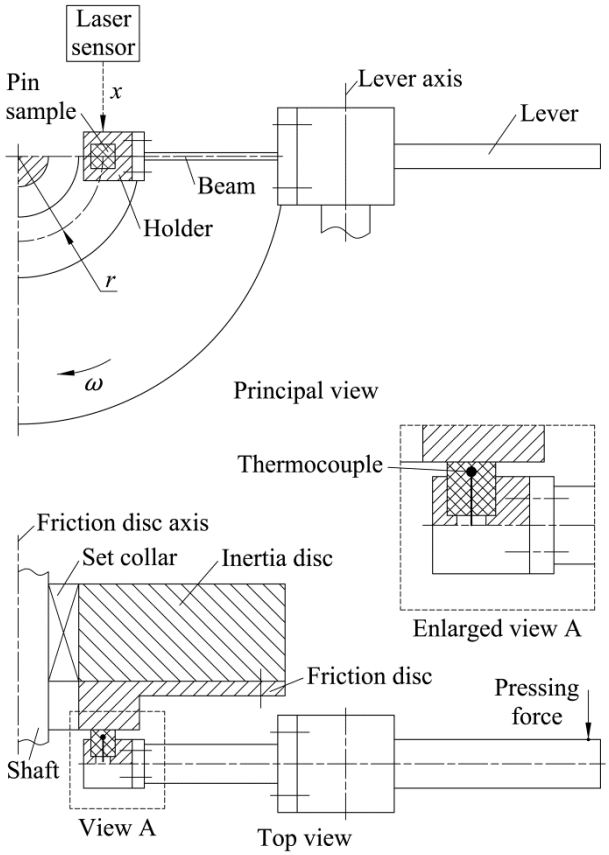

Fig. 1. Schematic of the pin-on-disc machine

The beam has a cross section of 16×2 mm² or 16×2.5 mm². It has a horizontal orientation. Under the action of the friction force on the pin sample, the beam is deformed and the pin sample moves in the direction tangential to the sliding interface. The tangential displacement x of the pin sample is measured by a laser sensor with a resolution of 0.2 μm. The laser spot, 70 μm in diameter, is focused on the polished upper face of the holder and corresponds to the radius r. The signal from the laser sensor is processed by a data logger with a sampling rate of 1 kHz.

For investigation of the temperature effect, the heating / cooling of the friction pair is provided. A gas burner with controllable gas flow rate is used for heating the inertia disc. The heat of the inertia disc is transferred to the friction disc and then to the pin sample through the sliding interface. The temperature T is measured in the pin sample by a chromel–alumel thermocouple installed at a distance of 2 mm from the sliding surface. The cooling is accomplished by natural convection from the exposed surfaces of the friction pair.

Thus, the adjustable parameters of friction are the contact pressure $p = N/S$, linear disc velocity $v = \omega r$ at the radius r and temperature T.

The pin sample is a non-asbestos organic material code-named SFP04 and used as brake pads in motor vehicles. It comprises barite, zirconium oxide, mica, phenolic resin, carbon, copper fiber, rock wool, brass fiber, etc. The friction disc is steel S275.

3. RESULTS AND DISCUSSION

3.1. Friction Coefficient

The tests are conducted to determine the friction coefficient μ at various values of the sliding velocity v_s and T. To prevent possible oscillation of the pin sample, a resin damper is attached to the beam in these tests. The friction coefficient is calculated as the ratio

$$\mu = kx/N$$

where k is the stiffness coefficient of the beam−holder couple determined experimentally. The 16×2 mm² and 16×2.5 mm² cross-section beams have k =19 N/mm and k =35 N/mm, respectively.

Fig.2 illustrates the obtained values of μ. As follows from the presented data, μ decreases with v_s, i.e., the friction–velocity slope is negative, and increases with T.

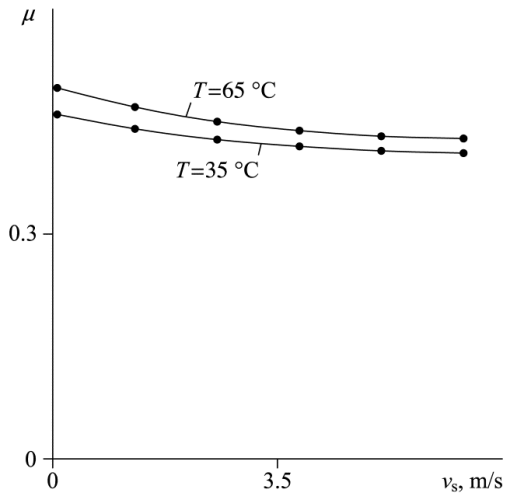

Fig. 2. Friction coefficient μ decreasing with the sliding velocity v_s at p =0.2 MPa

DOI 10.1515/ama-2015-0014

3.2. Oscillation Frequency

When the pin sample slides on the friction disc, one can observe its tangential oscillation, as presented in Fig. 3. The motion of the pin sample has a trajectory close to harmonic. Fig. 4 shows its frequency spectrum obtained by use of the discrete Fourier transform. The spectrum includes two noticeable peaks at f and $\omega/(2\pi)$. The peak at f is dominating. The small peak at $\omega/(2\pi)$ is evidently associated with the oscillation of the disc sliding surface. The tests show that f is 126 Hz for the 16×2 mm^2 cross-section beam and 163 Hz for the 16×2.5 mm^2 cross-section beam.

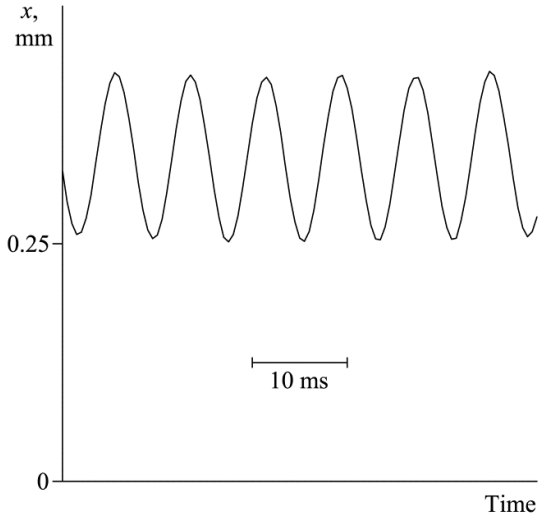

Fig. 3. Harmonic oscillation: 16×2 mm^2 beam, f =126 Hz, p =0.1 MPa, v =1.7 m/s, T =20 ºC

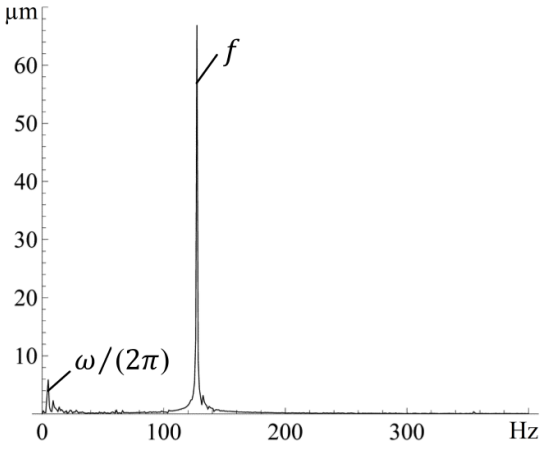

Fig. 4. Frequency spectrum

The evolution of x under the free oscillation of the beam-holder-sample system uninvolved in friction is analyzed. It is found that the frequencies f =126 Hz and f =163 Hz correspond to the first natural frequencies of the systems with the 16×2 mm^2 and 16×2.5 mm^2 cross-section beams, respectively.

Consequently, the observed tangential oscillation of the pin sample is a friction-induced oscillation which is most probably caused by the negative friction–velocity slope and occurs at the first natural frequency of the beam−holder−sample system. The oscillations of such type have been comprehensively studied earlier (see, for instance, Sheng, 2008).

According to the experimental data, if the oscillation occurs, its frequency f is insensitive to the friction conditions. However, the friction conditions influence considerably the oscillation amplitude A. Further, we consider the effects of v and T.

3.3. Disc Velocity Effect

The tests are done at v increasing from zero to some maximum value with a fixed increment each 30 seconds, as shown in Fig.5. One can notice that A increases at each increment of v.

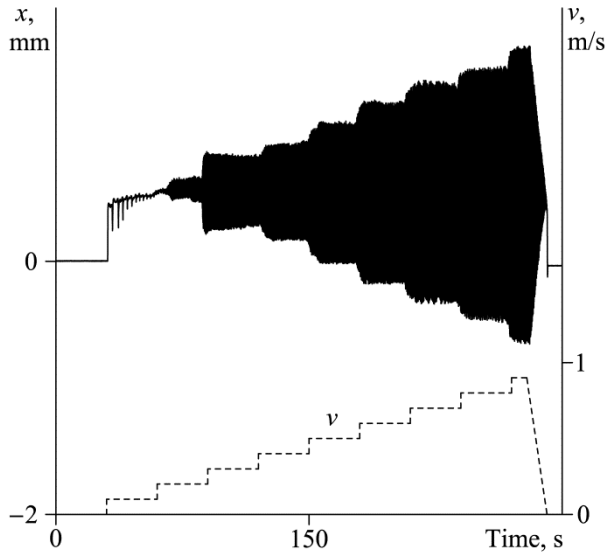

Fig. 5. Oscillation amplitude A increasing with the disc velocity v: 16×2.5 mm^2 beam, f =163 Hz, p =0.1 MPa, T =26–27 ºC

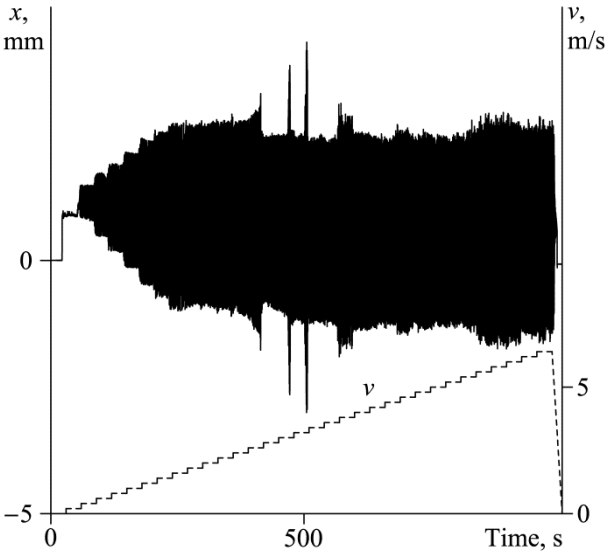

Fig. 6. Unpredictable change in the oscillation amplitude A at v >2 m/s: 16×2 mm^2 beam, f =126 Hz, p =0.2 MPa, T =29–37 ºC

The increase of A with increasing v is observed on the interval of small velocities. When v exceeds a value of about 2 m/s, there is no systematic relationship between v and A, as presented in Fig. 6. This result is testified for both 16×2 mm^2 and 16×2.5 mm^2 cross-section beams.

3.4. Temperature Effect

The influence of the temperature T on the oscillation occurrence is investigated. In the tests, v is constant, while T changes due to the heating / cooling of the friction pair.

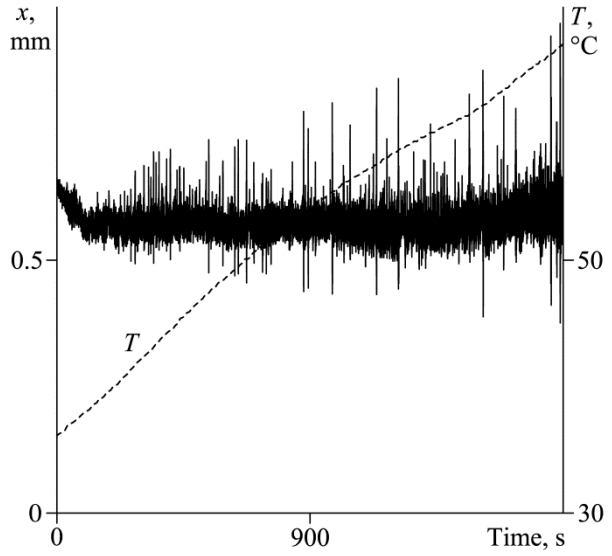

Fig. 7. Change in the sliding character with increasing temperature T: 16×2 mm^2 beam, p =0.2 MPa, v =4.4 m/s

For example, consider the experimental data depicted in Fig. 7. The test uses the 16×2 mm^2 cross-section beam. T increases from 36 to 64 °C. At the beginning of the test, the sliding is almost stable. The observable deviations of the pin sample are insignificant, as shown in Fig.8. In the course of time, T goes up and the instability of sliding in the form of oscillation is excited. At the end of the test, the oscillation occurs with A of the order of 100 μm, as shown in Fig.9.

A test similar to that above is conducted for the 16×2.5 mm^2 cross-section beam. The relation between T and the variation range of A is determined on the temperature interval of 20−56 °C. Fig.10 shows the obtained result. It is seen that at T = 20−29 °C $A = 0$, that is, the sliding is stable. When T = 29−48 °C, the oscillation may occur or decay unpredictably. Finally, if T exceeds 48 °C, the oscillation occurs continuously in time with A of the order of 20 μm. There is a clear trend of increasing A with T.

The two tests described are in agreement between each other. They reveal qualitative changes in the character of sliding caused by temperature variations. Note that these changes are reversible, i.e., at the stage of cooling, when T goes down, the oscillation amplitude A decreases and the oscillation can decay completely.

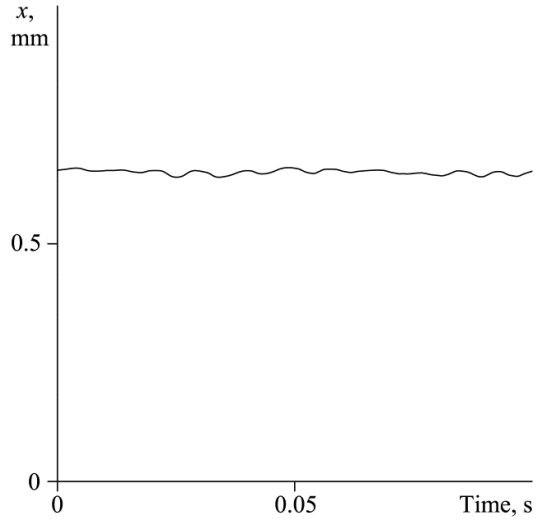

Fig. 8. Stable sliding with insignificant deviations at T =36 °C

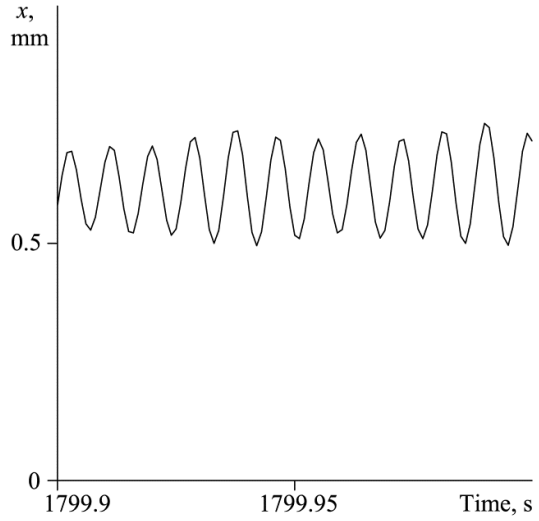

Fig. 9. Occurrence of oscillation at T =64 °C

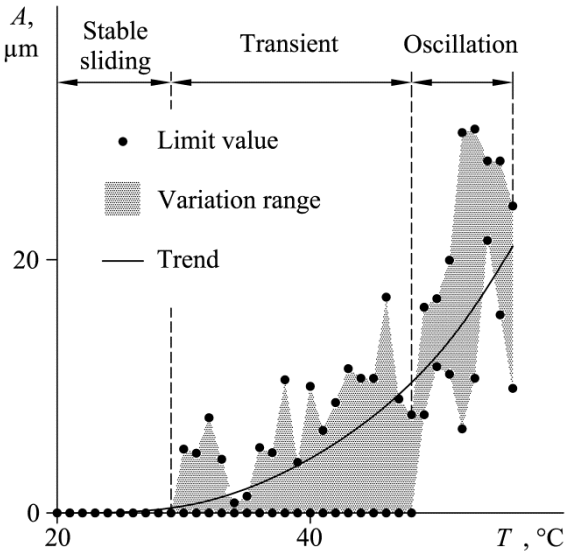

Fig. 10. Variation in the amplitude A depending on the temperature T: 16×2.5 mm^2 beam, p =0.2 MPa, v =4.4 m/s

DOI 10.1515/ama-2015-0014

4. CONCLUSIONS

An experimental study of friction-induced oscillations of a non-asbestos organic pin sample sliding on a steel disc has been done. The main results of the study are presented below.

1. The friction-induced tangential oscillation of the pin sample occurs at the first natural frequency of the supporting beam.
2. The oscillation amplitude increases with the disc velocity on the interval of velocities below 2 m/s. At higher velocities it changes unpredictably.
3. Temperature changes of several tens of degrees Celsius result in the oscillation occurrence / decay.

REFERENCES

1. **Adams G.G.** (1995), Self-excited oscillations of two elastic half-spaces sliding with a constant coefficient of friction, *Journal of Applied Mechanics*, 62, 867–872.
2. **Aronov V., D'Souza A.F., Kalpakjian S., Shareef I.** (1983), Experimental investigation of the effect of system rigidity on wear and friction-induced vibrations, *Journal of Lubrication Technology*, 105, 206–211.
3. **Barber J.R.** (1969), Thermoelastic instabilities in the sliding of conforming bodies, *Proceedings of the Royal Society of London Series A*, 312, 381–394.
4. **Bowden F.P., Leben L.** (1939), The nature of sliding and the analysis of friction, *Proceedings of the Royal Society of London Series A*, 169, 371–391.
5. **Dweib A.H., D'Souza A.F.** (1990), Self-excited vibrations induced by dry friction, part 1: experimental study, *Journal of Sound and Vibration*, 137 (2), 163–175.
6. **Earles S.W.E., Lee C.K.** (1976), Instabilities arising from the frictional interaction of pin−disk system resulting in noise generation, *Journal of Engineering for Industry*, 98, 81–86.
7. **Ishlinsky A.Y., Kragelsky I.V.** (1944), On jumps under friction, *Zhurnal Teknischeskoi Fiziki*, 14 (4–5), 276–283. (in Russian)
8. **Kajdanowsky N.L., Haykin S.E.** (1933), Mechanical relaxation oscillations, *Zhurnal Teknischeskoi Fiziki*, 3 (1), 91–109. (in Russian)
9. **Kinkaid N.M., O'Reilly O.M., Papadopoulos P.** (2003), Automotive disc brake squeal, *Journal of Sound and Vibration*, 267, 105–166.
10. **Mills H.R**. (1938), Brake squeak, *Institution of Automobile Engineers*, Report No. 9000 B.
11. **Nosko O.** (2013), *Effect of temperature on dynamic characteristics of a pad sliding on a disc*, Saitama University, Saitama. (dissertation)
12. **Sergienko V.P., Bukharov S.N., Kupreev A.V.** (2008), Noise and vibration in brake systems of vehicles. Part 1: experimental procedures, *Journal of Friction and Wear*, 29, 234–241.
13. **Sheng G.** (2008), *Friction-induced vibrations and sound: principles and applications*, CRC Press, Boca Raton, 141–248, 347–395.
14. **Spurr R.T.** (1961), A theory of brake squeal, *Proceedings of the Institution of Mechanical Engineers Automobile Division*, 15 (1), 33–52.
15. **Tworzydlo W.W., Hamzeh O.N., Zaton W., Judek T.J.** (1999), Friction-induced oscillations of a pin-on-disk slider: analytical and experimental studies, *Wear*, 236, 9–23.

The authors wish to thank Mr. Hisao Miura at Tokai Material Co., Ltd. for supplying friction materials.

THEORETICAL ANALYSIS OF MAGNETORHEOLOGICAL DAMPER CHARACTERISTICS IN SQUEEZE MODE

Bogdan SAPIŃSKI *

*Department of Process Control, AGH-University of Science and Technology,
Al. Adama Mickiewicza 30, 30-059 Kraków, Poland

deep@agh.edu.pl

received 21 April 2015, revised 20 July 2015, accepted 22 July 2015

Abstract: The paper summarises the theoretical study of a magnetorheological (MR) damper operated in squeeze mode, intended to be used as an actuator in a semi-active mount system in a car motor. The structural design and operating principle of the damper are described and a simplified model of the MR fluid flow in the gap is presented. The plots of the damper force generated by the MR damper are obtained for monoharmonic piston motion with respect to the centre point of the gap height and in the conditions of the control coil being supplied with direct current.

Keywords: MR Damper, Squeeze Mode, Gap, Force, Characteristic

1. INTRODUCTION

Vibrations of the drive unit in motor vehicles are typically caused by inertia force fluctuations due to the movements of unbalanced elements in the crank mechanism and to periodic variations of torque delivered from by the motor to the drive mechanism, also due to some random forces. Vibration reduction strategies usually include the use of passive elements in the form of either rubber or hydraulic systems.

Recently, the research efforts have been focused on semi-active or active actuators intended for use in vehicle mounts. An MR damper operated in squeeze mode can serve as an actuating element (Farjoud et al, 2011; Kim J. H., 2012; Sapiński and Krupa, 2013; Zhang et al, 2011). The distinctive feature of this damper is the variable gap height and that is why the magnetic flux linked with the control circuit is dependent both on the current level and on the gap height (Gong et al, 2014; Gołdasz and Sapiński, 2011; Kim K.-J., 2008; Sapiński et al, 2015). Incorporating such a damper in the mount system allows the adverse effects of motor vibrations to be effectively reduced (Snamina and Sapiński, 2014).

The paper summarises the theoretical studies of an MR damper operated in the squeeze mode, basing on a simplified model of the MR fluid flow in the gap. The damper characteristics are obtained assuming the monoharmonic piston motion with respect to the current gap height centre and for the control coil being supplied with direct current. Respective plots show the time histories of damper force and its dependence on the piston displacement.

2. DAMPER ASSEMBLY

A schematic diagram of the damper is revealed Fig. 1. The numeric symbols in the figure indicate all key components of the damper (1-8) and the key highlights materials used for manufacturing the device. The hardware features two concentric cylinders (1, 2). The inner non-magnetic cylinder (2) houses the piston (3), the core assembly (4), and the floating piston (5). The core assembly incorporates the coil (6). The outer cylinder (1) material is ferromagnetic. The distance between the lower surface of the piston and the upper surface of the core is referred to as the control (working) gap of time-varying height. The distance between the piston and the core varies according to the prescribed displacement (force) input (along the vertical z-axis). The floating piston below the core assembly separates the MR fluid from the coil spring located in the compensating chamber below the floating piston (5). The chamber incorporates a preloaded spring system (not shown in Fig. 1) for fluid volume compensation. Alternatively, the compensating chamber could be filled in with pressurized gas. The choice of the coil spring was due to convenience. The current in the control coil induces a magnetic field of the strength H. The magnetic flux that is generated by the current in the control coil (6) travels through the core and into the control gap, the outer cylinder, and back into the core through radially projected arms in the core base. The inner cylinder (2) of sufficient wall thickness is used to reduce the amount of magnetic flux bypassing the control gap, i.e. magnetic short circuit. All of the components ensure an efficient magnetic flux return path.

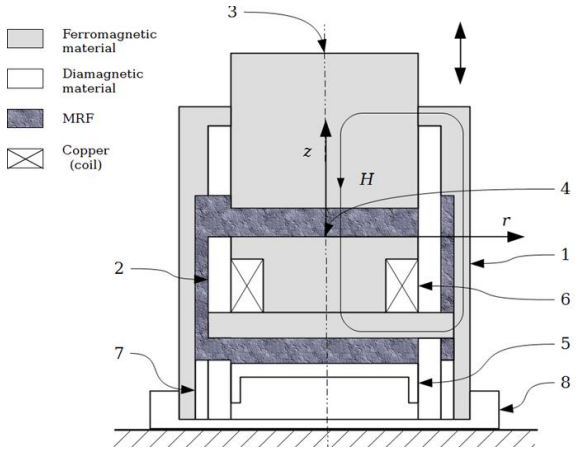

Fig. 1. Schematic diagram of the damper

DOI 10.1515/ama-2015-0015

The flux that is induced in the control gap upon the application of the coil current effectively modifies the yield stress of the fluid, and its resistance to flow. As the piston moves downward, the distance between the core and the piston decreases. The excess of MR fluid is squeezed out of the control gap into the fluid volume between the inner cylinder and the outer housing of the damper, and then into the compensating chamber. The additional fluid volume that enters the compensating chamber pushes the floating piston against the coil spring. The structure incorporates a non-magnetic ring (7), whereas the base cap (8) is used for fixing the assembly against the ground. The MR fluid type employed in the damper is BASF Basonetic 4035 (Kieburg, 2010). The outer cylinder length is 133 mm and the diameter is 102 mm.

3. MAGNETORHEOLOGICAL FLUID FLOW IN THE GAP

MR fluid in the damper flows in the closed-loop circuit comprising the gap where the MR fluid is exposed to the magnetic field and the container in the bottom section of the damper. The gap and the container are connected by channels placed inside an inner cylinder. Downward movement of the piston at the speed $vp = \dot{h}$ induces the fluid flow away from the gap whilst during its upward motion the fluid flows towards the gap. During the piston motion the surface area (the cylinder's side wall) through which the fluid flows in and out will be changed.

Velocity of fluid elements is related to the piston velocity and its position. At small gap heights, the velocity of fluid flow tends to increase significantly. Fluid velocity distributions $v(r,z)$ in the gap are shown schematically in Fig. 2 (for the downward motion of the piston). MR fluid flow is assumed to be governed by the Bingham model whereby yield stress increases linearly with the strain rate after exceeding the yield strength, related to the magnetic field strength H. This model is typically recalled to describe the behaviour of MR fluids under the action of magnetic field.

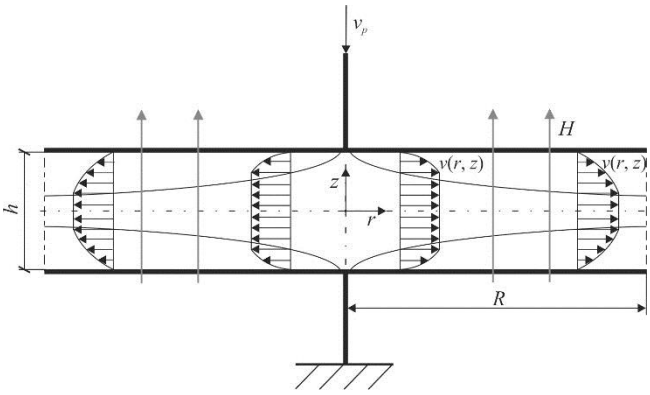

Fig. 2. Schematic diagram of MR fluid flow in the gap

Within the gap region (beneath the piston) there are three characteristic flow regimes. The first emerges near the piston surface, the second-near the cylinder bottom surface. In those regions fluid flows with the tangent stress exceeding the yield strength. As shown in velocity profiles (see Fig. 2), individual fluid layers move at speed being the function of the coordinate z. The third flow regime encompasses the gap's middle section, where the fluid layers do not move with respect to one another, their speed is not dependent on the coordinate z and the tangent stress is less than the yield strength. On interface surfaces between those flow regimes the tangent stress equals the yield strength. In the light of the relationship between the yield strength and magnetic field strength, the locations of those interface surface as well as their actual shape will vary depending on the magnetic field strength.

4. DAMPER CHARACTERISTICS

Taking into account the structure of the device (see Fig. 1), the force F generated by the damper has the following components:

$$F = F_\mu + F_\rho + F_{\tau_0} + F_s \tag{1}$$

where: F_μ – force associated with fluid viscosity, F_ρ – inertia force of the fluid motion, $(F_\rho = F_{\rho_1} + F_{\rho_2})$, F_{ρ_1} – force associated with piston acceleration, F_{ρ_2} – force related to the squared piston velocity, F_{τ_0} – force associated with the yield strength of fluid, F_s – resultant force from the spring system for fluid volume compensation.

The components of the force F can be expressed as:

$$F_\mu = -\frac{3\pi\mu R^4}{2h^3}\dot{h} \tag{2}$$

$$F_\rho = F_{\rho_1} + F_{\rho_2} = -\frac{\pi\rho R^4}{2h}\ddot{h} + \frac{\pi\rho R^4}{4}\left(\frac{\dot{h}}{h}\right)^2 \tag{3}$$

$$F_{\tau_0} = -\frac{\pi R^3 \tau_0}{4h}\operatorname{sign}(\dot{h}) \tag{4}$$

$$F_s = -k(h - h_0) \tag{5}$$

where: μ – fluid viscosity, ρ – fluid density, τ_0 – yield strength, R – piston diameter, k – stiffness coefficient of the spring system, h, $(\dot{h},\ \ddot{h})$ displacement (velocity, acceleration) of the piston, h_0 – neutral position of the spring system.

Damper characteristics are obtained basing on the geometrical data and materials specifications summarised in Sapiński (2015) and with the following assumptions:

- the gap height h can vary in the range from 6.26 to 0.5 mm,
- the piston moves with respect to the central point of the current gap height,
- piston excitation is sinusoidal with amplitude A and frequency $f(z = z0 + A\ sin2\pi ft)$; $(z_0 = h_0)$,
- control coil is supplied with direct current I.

The contribution of individual force components F_μ , F_ρ, F_{τ_0}, F_s is examined recalling Eq (2-5) and using the MATLAB calculation data underlying the damper characteristics shown in Figs. 3-9. A thorough analysis of those characteristics allows the contributions of individual force components to be assessed in quantitative terms.

Figs. 3a, 3b, and Fig. 4 plot the relationship between the damper force and piston displacement and time histories of (in relative time $t \times f$) of the damper force for fluctuating piston displacement frequency and for the control coil being supplied with the current I: 0.5 A, 2 A. The plots clearly indicate that the current level in the control coil is the major determinant of the damper force whereas for the given current level, the frequency of piston motion (piston velocity) plays a minor role, which is best seen at small gap heights.

To examine the contributions of particular force components

F_μ, F_ρ, F_{τ_0}, F_s to the damper force F, their time histories were obtained for various piston displacements and for different current levels in the control coil. Selected plots are shown in Fig. 5, for the current I = 0.5 A, revealing the dominant role of the force component F_{τ_0} associated with the yield strength of the fluid τ_0. This term is associated chiefly with the current level in the control coil (magnetic field strength in the damper) and, in a lesser degree, with the piston velocity. These findings are confirmed by plots in Fig. 6 which compares the generated force F for the current levels I 0.5 A and 2 A. It appears that the contribution of force components F_μ, F_ρ, F_s to the force F is rather minor. Time patterns of forces F_μ, F_ρ, F_s obtained for other current levels and for frequency f resemble the plots in Fig. 5. It is worthwhile to mention the term F_ρ. Fig. 7 and 8 plot the forces F_{ρ_1} and F_{ρ_2} in the function of piston displacement for various frequency and for the current I =0.5 A. It appears that those forces have unlike signs and are clearly dependent on frequency f (piston velocity). The contribution of these force components to the damper force F is the largest for small gap heights.

a)

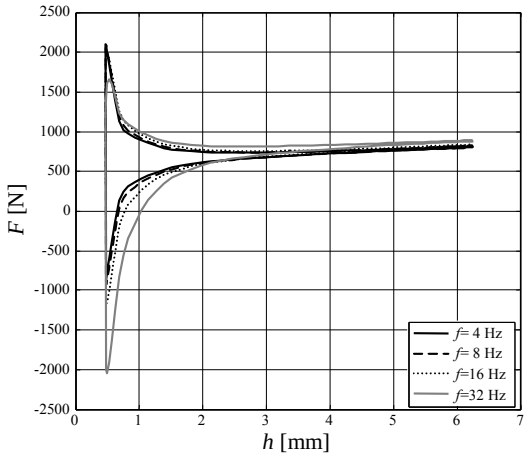

b)

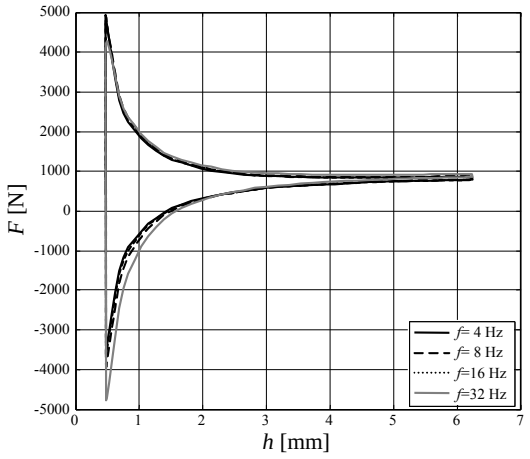

Fig. 3. Damper force vs gap height h for variable frequency f; a) I=0.5 A, b) I=2 A

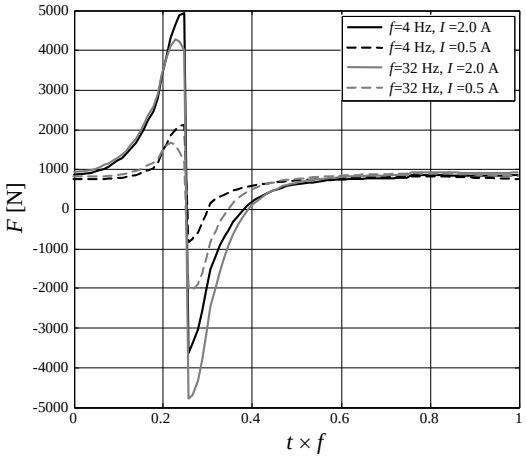

Fig. 4. Time histories of force F for variable frequency f and for the current I: A=1 mm

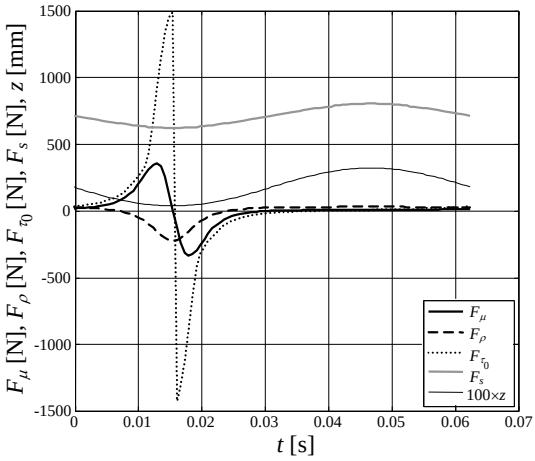

Fig. 5. Time histories of forces F_μ, F_ρ, F_{τ_0}, F_s; f=16 Hz, A=1 mm, I=0.5 A

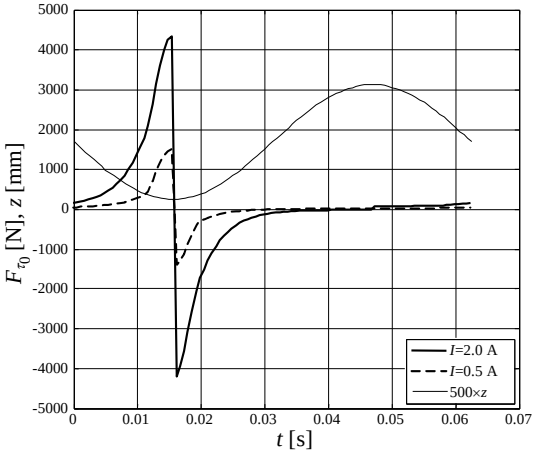

Fig. 6. Time histories of F_{τ_0} for various current levels I; f=16 Hz, A=1 mm

DOI 10.1515/ama-2015-0015

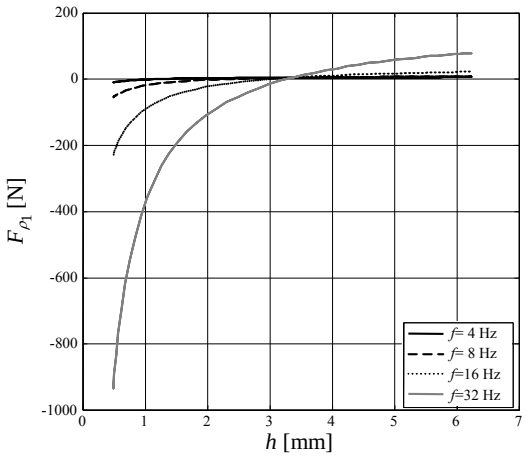

Fig. 7. Force F_{ρ_1} vs gap height for variable frequency f; I=0.5 A

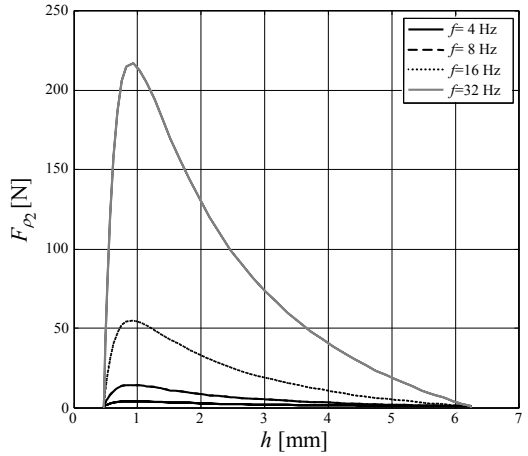

Fig. 8. Force F_{ρ_2} vs gap height for variable frequency f; I=0.5 A

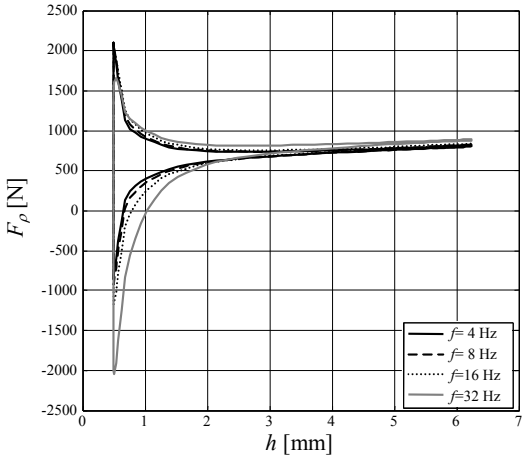

Fig. 9. Force F_ρ vs gap height for variable frequency f; I=0.5 A

5. CONCLUSIONS

The study is focused on theoretical characteristics of the MR damper operated in the squeeze mode. The analysis of those characteristics leads us to the following conclusions:

- of major importance is the contribution of the force component F_{τ_0} (associated with the fluid's yield strength and dependent on the current level in the control coil);
- for the given current level, the influence of the piston velocity on the force component F_{τ_0} is rather minor;
- for the given piston velocity and current level, the contribution of force components F_μ, F_ρ is minor, too;
- the influence of force components F_{ρ_1} and F_{ρ_2} is best revealed for small gap heights and high piston frequencies (see Figs. 7, 8).

Predicted damper characteristics will be verified by the damper prototype model testing on the tester machine.

REFERENCES

1. **Farjoud A., Craft M., Burke W., Ahmadian M.** (2011), Experimental investigation of MR squeeze mounts. *Journal of Intelligent Material Systems and Structures*, 22, 1645–1652.
2. **Gołdasz J., Sapiński B.** (2011), Model of a squeeze mode magnetorheological mount. *Solid State Phenomena*,177:116–124.
3. **Gong X., Ruan X., Shouhu X., Yan, Q., Deng H.** (2014), Magnetorheological Damper Working in Squeeze Mode, Hindawi Publishing Corporation, *Applications of Controllable Smart Fluids to Mechanical Systems*, *Advances in Mechanical Engineering*, Article ID 410158, 1–10.
4. **Kieburg Ch.** (2010), MR Fluid Basonetic 4035, *BASF Technical Information*.
5. **Kim J. H. (**2012), Damping control device with magnetorheological fluid and engine mount having the same, *United States Patent Application Publication* US 2012/0132492A1.
6. **Kim K.-J., Lee Ch.-W., Koo J.-H.** (2008), Design and modeling of semi-active squeeze film dampers using magnetorheological fluids, *Smart Materials and Structures*, Vol. 17, doi: 10.1088/0964–1726/17/3/035006, 1–12.
7. **Sapiński B. (**2015), Simulation of electromagnetic phenomena in a prototype MR damper in squeeze mode, *Modelling in Engineering*, (to be published).
8. **Sapiński B., Krupa S.** (2013), Vibration isolator with MR fluid in squeeze mode, *Notification of inventive design* No. P.406179, 37.
9. **Sapiński B., Krupa S., Matras A.** (2015), Simulation of a control circuit for an MR damper in squeeze mode, *Electrotechnical Review*, Vol. 2015, No. 8, 135–138 .
10. **Snamina J., Sapiński B.** (2014), Analysis of an automotive vehicle engine mount based on squeeze-mode MR damper, *Technical Transactions - Mechanics*, Cracow University of Technology Press, 2-M (13), 2014, 53- 63.
11. **Zhang X. J., Farjud A., Ahmadian M., Guo K. H., Craft M.** (2011), Dynamic Testing and Modelling of an MR Squezee Mount, *Journal of Intelligent Material Systems and Structures*, Vol. 22, 1717- 1728.

This research is supported by the National Centre for Research and Development under the grant No. PBS 1/A6/3/2012.

INTEGRATED MULTIMOTOR ELECTRICAL DC DRIVE FOR METALLURGICAL ROLLING TABLE

Marek Gała[*], Kazimierz JAGIEŁA[**], Andrzej JĄDERKO[*], Janusz RAK[*]

[*]Faculty of Electrical Engineering, Czestochowa University of Technology, Al. Armii Krajowej 17, 42-200 Częstochowa, Poland
[**]Faculty of Management, Czestochowa University of Technology, Al. Armii Krajowej 17, 42-200 Częstochowa, Poland

mgala@el.pcz.czest.pl, kazimierz.jagiela@gmail.com, aj@el.pcz.czest.pl, jrak@el.pcz.czest.pl

received 7 September 2014, revised 25 May 2015, accepted 28 May 2015

Abstract: A drive system of a section of a metallurgical rolling table consisting of six dc motors, 2220 amperes of total current, fed from a single ABB reversible thyristor converter has been described in this paper. Autonomous excitation circuits of the motors are fed from independent thyristor converters working in the so called MULTIFEX system linked with a supervisory high power converter. There are presented schemes of the DSL communication realized by FEX excitation cards of the motors using the SDSC card of the DCS-800-S02 converter and logic control system based on a PLC controller. The parameterization of the DCS-800 converter and the DCF 803 excitation systems was conducted using the DriveWindow software tool. Significant waveforms of voltages, currents and the estimated motor velocity are described and presented for the idle run as well as during transporting sheets discharged from a pusher furnace.

Key words: DC Drive System, Rolling Table, FEX Excitation System, Drivewindow Software

1. INTRODUCTION

Contemporary applications of complex drive systems are usually based on asynchronous squirrel-cage motors. Nevertheless, for technical and/or economical reasons, existing drives with DC motors are modernized by implementing highly specialized thyristor bridges with various control algorithms. Solutions presented in the literature include control systems based on the phase-locked loop synchronization (Abu-Rub et al., 2004; 2005) or on the mechanical vector reconstruction using a state variable observer (Guziński et al., 2009). In the Polish metallurgical and paper-making industry it is very common that after modernization the DC motors installed before remain in use adapted for powering from modern converters employing advanced control techniques, such as MASTER-FOLLOWER (Gała et al., 2009; Jagieła and Gała, 2008) or MULTIFEX (Multifex motor control for roller tables, 2008). Such solutions apply in principle to drives with electric motors of relatively high power. The reason is minimization of the drive modernization cost including installation of the power electronics supply system. Alternative replacement of a DC drive by an asynchronous drive with a frequency converter often entails mechanical and building modifications.

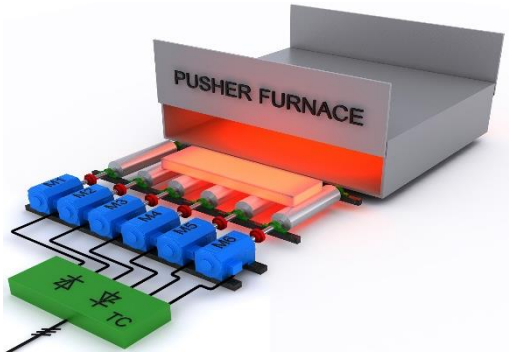

Fig. 1. Discharge rolling table with a separate drive of each roll

The subject of modernization described in this paper is discharge rolling table drive of a pusher furnace. There are many types and designs of components of such an electro-mechanical system, i.e. rolls, the mechanism of the torque transmission, a single motor or group of motors and a power electronics supply system. The two types of drives most often used in discharge rolling table systems are:

- multi-output reduction gear asynchronous drives with controlled angular velocity (Jagieła, 2003);
- separate drives of each roll with DC or AC motors.

A discharge rolling table with separate DC drives for the individual rolls is shown in Fig. 1.

The paper deals with an application of the ABB reversible thyristor converter type DCS800 S02, which feeds several to teens armature circuits of separately excited DC motors from a single DC circuit. The considered system is an original solution of the ABB (Multifex motor control for roller tables, 2008) dedicated for rolling table drives. The control of the multimotor MULTIFEX system is based on a PLC controller. The drive is a part of a complex automation system of heating and conveyance of slabs on a plate rolling line.

A similar system, but with different control scheme, has been described in Kolar and Friedli (2013), where a model of a four-motor DC unit that drives two drums of a papermaking machine has been presented.

2. MECHANICAL SYSTEM OF THE DISCHARGE ROLLING TABLE SECTION DRIVE

The drive of the discharge rolling table section is a group drive system fed from a single converter TC (Fig. 1). Electric motors M1 ÷ M6 are coupled by connecting links directly to the rolls conveying slabs or a metal strip (Fig. 2). The direct coupling of the motors to the rolls results from using high-power and slow-speed motors that ensure enough torque to cope with the static load as well

DOI 10.1515/ama-2015-0016

as with the impulse load due to eccentric impacts of the conveyed strip against the table rolls. The characteristics of the roll load torque versus time can be described by equation (1):

$$T_{L_i}(t) = T^{\varphi}(t) - T^{\varphi}(t-\Delta\tau) + T_S(t-\Delta\tau) - T_S(t-t_{1_i}) \quad (1)$$

where: $\Delta\tau = \frac{30\cdot\varphi[rad]}{2\pi\, n} = \frac{\varphi[^\circ]}{6\, n}$ s; $n \in \langle n_{\min}, n_{\max}\rangle$ rpm, $t_{1i} = \frac{v_1}{l_r+0.5D_z}\cdot i$, D_z – external diameter of the roll, l_r – distance between the rolls, v_1 – slab/strip speed, i – roll number.

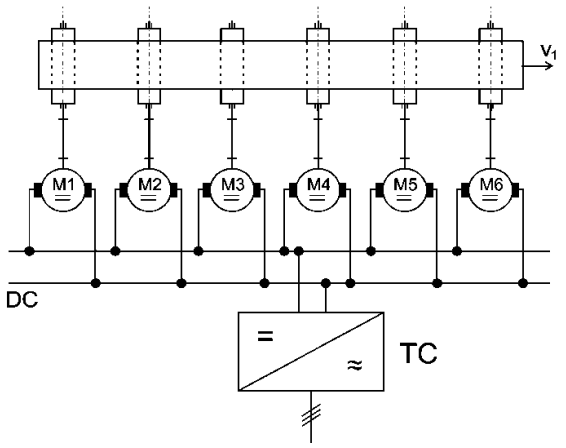

Fig. 2. Electromechanical system of the discharge rolling table drive

The static torque T_S from the mass of the conveyed slabs can be determined using formula (2):

$$T_S = \left[(m_c^* + m_b)\cdot f_t \cdot \frac{D_t}{2} + m_c \cdot f_r \cdot \frac{D_z}{2}\right]\cdot g \quad (2)$$

where: $m_c^* = \frac{m_c}{N}$ – mass of a conveyed slab per single roll, mb – mass of the roll drum, N – number of rolls, other quantities are given in Tab. 2.

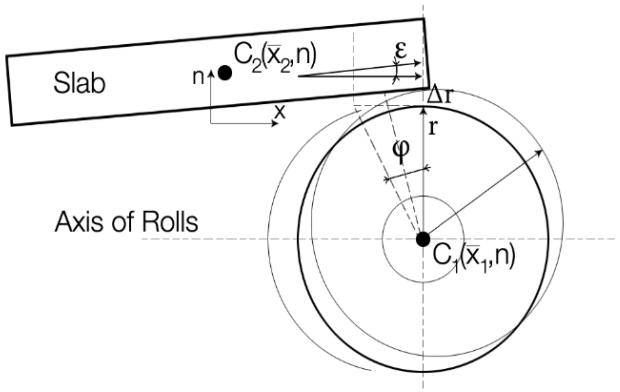

Fig. 3. Mechanism of eccentric movement of the roll (Dobrucki et al., 1991; Jagieła, 2003). Description: C_1 – centre of gravity of the roll, C_2 – centre of gravity of the slab, ε – inclination angle of the slab with respect to the roll axis, φ – angular displacement of the roll, r – roll radius, Δr – lift of the slab due to eccentricity of the roll

The second component of the load torque T_L is connected with geometry and buckling of the conveying rolls. The geometry of the rolls in the considered section of the rolling table depends mainly on two factors: 1) variation of diameters of the individual rolls due of wear off and 2) eccentric movement of the rolls due to deflection of the frame and the bearings (Dobrucki et al., 1991), termic buckling (Dobrucki et al., 1991) and impacts from the metal strip when its end is turned up (Jagieła, 2003). The mechanism of the eccentric movement of the roll with respect to the conveyed metal strip is illustrated in Fig. 3.

The eccentric movement of the rolls produces impulse load forces Q_1^{φ}, that can be determined using formula (3) (Dobrucki et al., 1991; Jagieła, 2003):

$$Q_1^{\varphi} = S^{\varphi}\cdot\sqrt{\frac{k_1}{m_1}}\cdot\frac{a}{\sqrt{a^2+\frac{1}{M}}} \quad (3)$$

where the impulse impact S^{φ} can be evaluated as:

$$S^{\varphi} = (1+R^*)\cdot(v_1-v_2)\frac{m_c m_1}{m_c+m_1} = (1+R^*)\cdot k_v\frac{m_c m_1}{m_c+m_1}\cdot v_1 \quad (4)$$

Explanation of quantities occuring in equations (3) and (4) and their values are collected in Tables 1 and 2. The load torque of the rolling table due to the impulse eccentric impact is:

$$T^{\varphi} = Q_1^{\varphi}\cdot\frac{D}{2} = S^{\varphi}\cdot\frac{D}{2}\cdot\sqrt{\frac{k_1}{m_1}}\cdot\frac{a}{\sqrt{a^2+\frac{1}{M}}} \quad (5)$$

For the assumed asymmetry k_v of the linear velocities the ratio of the eccentric impact torque T^{φ} to the nominal electric torque of the roll:

$$k^{\varphi} = \frac{T^{\varphi}}{T_M} = 2{,}13 \quad (6)$$

Tab. 1. Parameters of impact forces acting on the roller drum while conveying the steel strip

Parameter	Label and value	Relation ships
Coefficient of elasticity of the drum	k_1 = 94 MN/m q = 0.5	$k_1 = 48EJ/qL^3$ E = 2.1·10¹¹ N/m² $J = \frac{\pi\left(D_z^4 - D_w^4\right)}{64}$ m⁴ $q = f_1/f_0$ - ratio of deflections of the drum and the bar (Dobrucki et al., 1991)
Drum mass reduction	m_1 = 2.64 T β = 0.8	$m_1 = \beta\cdot m_b$ β – coefficient of the drums mass reduction depending on proportion of their dimensions (Dobrucki et al., 1991)
Parameters	A = 9.06 K = 6.5 M = 0.1	$a = \sqrt{\frac{K}{M}+1}$ $K = \frac{k_2}{k_1}$ $M = \frac{m_2}{m_1}$
Coefficient of restitution	R^* = 0.15	determined from the graf for steel in function of the slab temperature (Dobrucki et al., 1991).
Linear velocities	v_1. v_2	velocities of the masses in the n-x reference frame (Fig. 2); linear velocity of the strip v_1; linear velocity of the second motor roll drum $v_2 = \omega_2\cdot\frac{D_z}{2}$
Asymmetry of velocities	k_v = 0.02	$k_v = \frac{v_1 - v_2}{v_1}$

Tab. 2. Electric and mechanic parameters of the rolling table

Parameter	Designation and value
Roll parameters	
a) external diameter	D_z = 0.4 m
b) internal parameters	D_w = 0.3 m
c) roll pin diameter	D_t = 0.2 m
d) working length of the roll	L = 5.7 m
e) distance between rolls	l_r = 0.8 m
f) roll drum mass	m_b = 3.3 T
g) moment of inertia of the roll	Θ_r = 103 kgm^2
Strip parameters	
a) linear velocity of the strip	v_1 = 1.675 ms^{-1}
b) strip mass	m_c = 10.7 T
c) coefficient of strip-roll friction	f_r = 0.3
d) coefficient of friction in the roll bearings	f_t = 0.06 ÷ 0.08
Electro-mechanical system parameters	
a) moment of inertia of the coupling and the connectors	Θ_s = 28 kgm^2
b) moment of inertia of the motor	Θ_M = 30 kgm^2
c) motor torque	T_M = 1365 Nm

The ratio of the static torque to the electric torque for the rolls and the strip whose parameters are given in Tab. 2 is:

$$k^M = \frac{T_S}{T_M} = 0.98 \tag{7}$$

Taking into account formula (1) and the components of the load torque defined by formulas (2) and (5), the equation of the roll dynamics for start-up and braking is as follows:

$$\lambda T_M = \lambda[c_M \Phi I_M] = T_L(t) + T_D = T_L(t) + \lambda\left[(\Theta_\Sigma + m_c^* g \frac{D_z^2}{4}) \frac{d\omega}{dt}\right] \tag{8}$$

where: c_M – torque constant od the dc motor, Φ – field flux of the dc motor, I_M – armature current of the dc motor, λ = +1 for start-up, λ = -1 for braking, g = 9.81 m/s^2, $\Theta_\Sigma = \Theta_r + \Theta_s + \Theta_M$.

The change of the static load T_L due to variable force of the impulse load torque, whose resultant value is $(T_L + \Delta T_L)$, or due to change of the angular velocity $(\omega + \Delta\omega)$, causes response of the MULTIFEX control system resulting in change of the field flux $(\Phi + \Delta\Phi)$ that satisfies equation (8).

3. SUPPLY AND CONTROL SYSTEMS OF DISCHARGE ROLLING TABLES WORKING IN THE MULTIFEX MODE

The drive system of the discharge rolling table section of the conveyance line consists of six DC motors, which are directly engaged with the conveying rolls by short couplers (Fig. 1). The diagram of the power electronics supply system of the DC motors with high power control of the armature circuits and controlled field circuits is shown in Fig. 4. The choice of such a scheme of the supply and control was due to decision to remain the DC motors and necessity to maintain angular speeds of the individual motors that ensure equal linear speeds of all rolls, taking into account their geometric parameters.

The control of the thyristor systems that takes into account optimization of the THD coefficients and improvement of the power factor coefficient PFC (Friedli et al., 2014; Kolar and Friedli, 2013) is an important issue from the consumer power quality point of view. Therefore, the drive supply diagram shown in Fig. 4 includes the UPQ system for continuous monitoring and data acquisition.

The main parameters of the discharge rolling table drive with the separately excited DC motors are presented in Tab. 3.

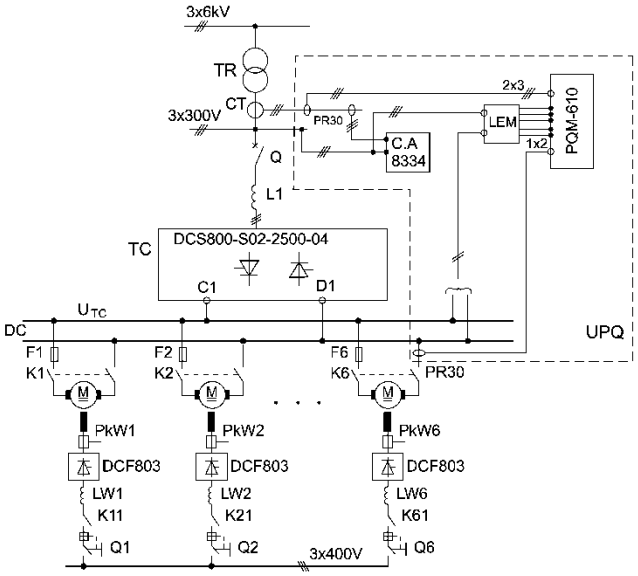

Fig. 4. Diagram of the drive supply system with outlined control system (UPQ) and pointed measurement points

Tab. 3. Main parameters of the discharge rolling table drive

Motor and converter parameters
Motor type: PXOm-74b/01; quantity: 6
P = 75/150 kW; U = 220/440 V; I = 370 A; n = 525/1040 rpm; I_F = 5 A; T = 1365 Nm
Control range of angular and linear speed: n_{min} = 80 rpm → n_{max} = 140 rpm v_{min} = 3.35 m/s → v_{max} = 5,86 m/s
Converter type: DCS800-S02-2500-04
U_{supp} = 3 × (230 …415) V AC I_{DC} = 2500 A; P_{DC} = 1038 kW

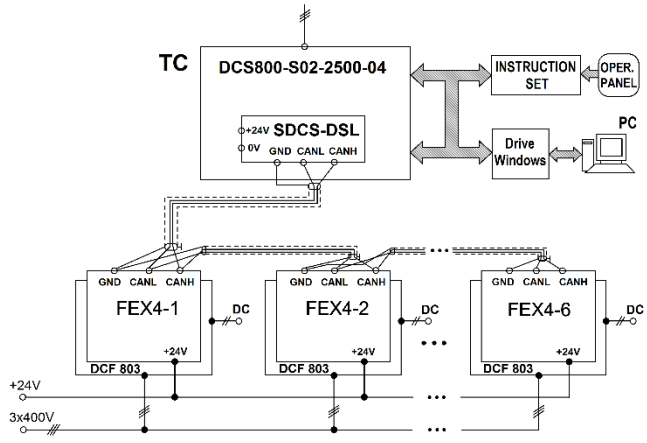

Fig. 5. Communication of the field circuit supply units DCF803 with the main DCS800 converter

The principal aim of the control is to eliminate shearing of the conveyed slabs by minimizing differences of linear speed of the individual rolls. To achieve this aim a drive system including six DC motors with armature circuits connected to a single reverse thyristor converter and making up the MULTIFEX network was applied. The

DOI 10.1515/ama-2015-0016

field circuits of the motors are supplied by separate 3T-3D thyristor-diode bridges DCF803 and controlled from the main DCS800 converter via the DSL serial communication link connected to the SDCS-DSL board of the converter – Fig. 5.

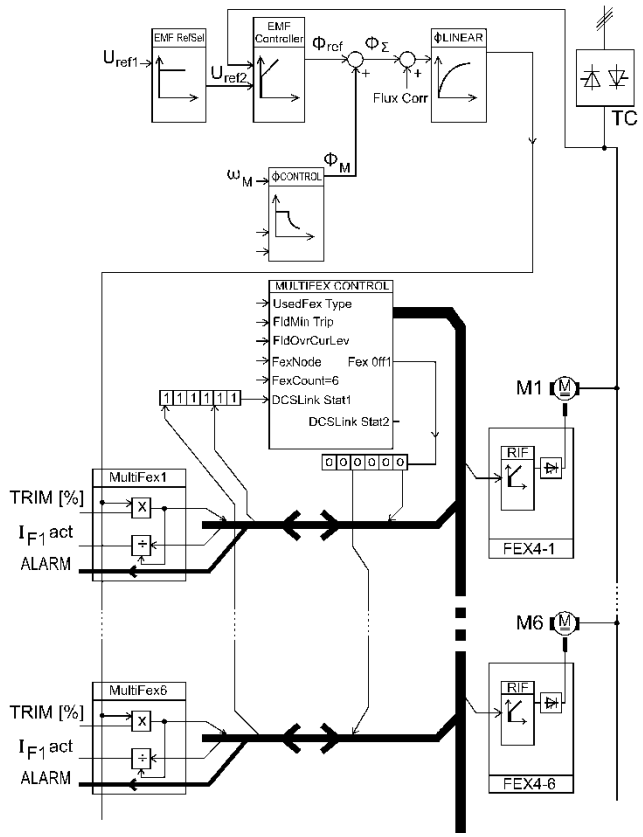

Fig. 6. Diagram of the MULTIFEX control

The control of the motor field circuits in the MULTIFEX system (Fig. 6) is based on H8 microcontrollers that control synchronization of the currents and handle errors. The microcontrollers communicate using the CAN serial interface. The control programs are stored in the FlashPROM memory and include:

- RIF PI control of the field current with the controller parameters,
- error handling and reset,
- synchronization and the PLL control,
- configuration of the current measurement channels.

The master loop in the MULTIFEX control diagram (Fig. 6) is the electromotive force (EMF) control loop. The output of the EMF controller is the reference input Φ_{ref} of the magnetic flux controller. The total flux Φ_{Σ} is the sum of Φ_{ref} and the second component Φ_M, which is the output of the flux weakening controller Φ CONTROL. The input of the Φ CONTROL block is the angular speed signal from the tachometer or encoder or, as in the described case, it uses an adaptive algorithm for estimation of the angular speed in the multimotor drive.

The final reference signal of the field current is obtained after linearization Φ LINEAR. In each MultiFex motor control unit it is corrected by multiplier TRIM [%] to achieve the required speed of each motor with minimum error. By applying the static correction TRIM, set separately for each field circuit, it is possible to minimize differences of linear speeds of the individual motors resulting from geometrical deviations of the roll sizes and deviations of the armature and field circuit resistances due to rewinding during the motors repair.

4. DRIVE COMMISSIONING AND RESULTS OF MEASUREMENTS

The presented multimotor drive system of the discharge rolling table is a part of the plate rolling line. Its task is to convey slabs and adapt the conveyance to the technological regime of the whole rolling line. The system has two modes of operation:

1. manual control by the operator;
2. automatic control cycle depending on operation of other discharge devices of the plate rolling line with control sequences planned online.

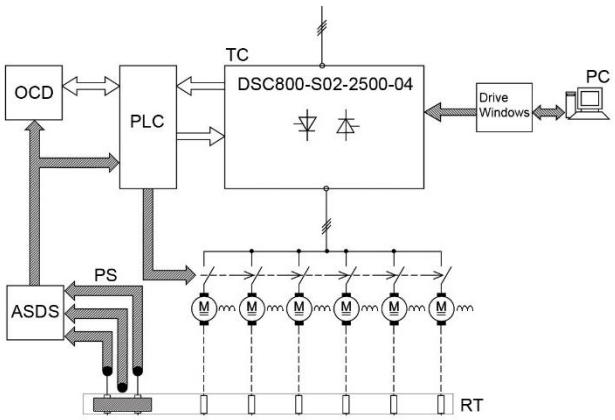

Fig. 7. Diagram of the DSC800 converter external control:
OCD – operator control desk, RT – rolling table,
PS – process signals, ASDS – automatic slab delivery system,
TC – thyristor converter

The discharge rolling table drive is controlled hierarchically taking into account correlations with other devices of the rolling line. The first level of control is realized by the PLC controller (Fig. 7) that receives information from the automatic slab delivery bus. The delivery control works in sequential cycles: it conveys slabs from the pusher furnaces towards the break-down rolling stand. The PLC controller receives signals carrying information about the current run of individual stages of the technological process. The second, master level of control are commands from the operator control desk and the emergency stop signal that are basic safety protections of the staff and devices.

The reverse thyristor converter PT (DCS800) with the assigned field units FEX4-DCF803 should be precisely parameterized at the stage of the drive commissioning or restarting. A helpful tool for these purposes is the DriveWindow tool (Gałą et al., 2009) (Fig. 5, Fig. 7). It is a multifunction application for: setting and adjusting control parameters, starting a drive, monitoring analog and digital quantities (signals) and controlling drives with DC or AC motors supplied respectively from DCS or ACS series converters and equipped with fiber-optic links.

In the considered system the application supervises simultaneous operation of the main DCS800 converter and six field circuit converters DCF803. It collects current values of signals and can present them, e.g. in the same graph for comparison.

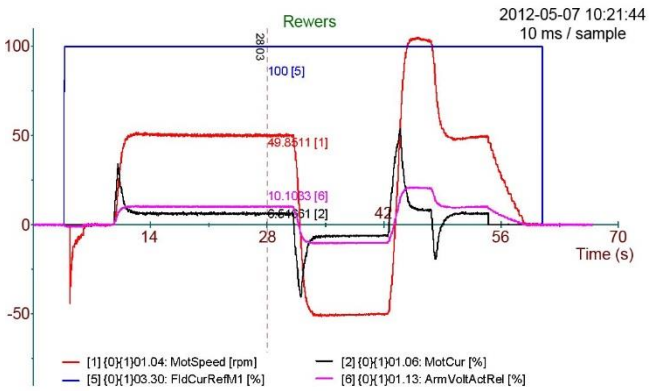

Fig. 8. Waveforms of electromechanical quantities of the discharge rolling table drive

All the monitored data and parameters can be saved in the files for further offline analysis or edition. The files with the drive settings, stored in the archive or edited offline, can be loaded to the converter memory which minimizes the time of starting the drive or restarting it after a failure. An example of the DriveWindow capabilities is presented in Fig. 8. The graph shows waveforms of the voltage and total current of the armature circuits as well as the estimated angular speed and field current of a single motor (they are the same for the other motors) recorded during the startup, reverse, rapid change of the angular velocity (commanded by the external controller) and finally the stop of the drive.

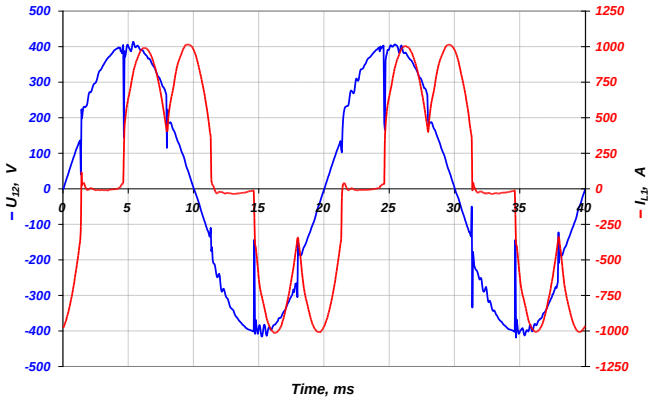

Fig. 9. Waveforms of the DCS800 converter supply voltage and current

Another tool for aiding the process of setting the drive operation parameters is the computer measurement unit PQM-610. It includes voltage and current transducers LEM, current measurement pincers PR-30 (Fig. 4) and the DASYLab software. The metrological parameters of the measurement unit ensure accuracy up to 0.1% as far as the higher-order harmonic content coefficients THD of the voltage and current are concerned. The complement of the PQM-610 unit is the power quality analyzer CA8334 connected to the low voltage network 3 × 300 V and to the secondary circuit of the current measuring transformer CT 4000A/5A (Fig. 4). Those two measurement devices make it possible to analyze the influence of the rolling table drive on the local internal medium and low voltage network, in particular arising of higher-order harmonics of the current. Example waveforms of the converter phase-to-phase supply voltage and the phase current are shown in Fig. 9.

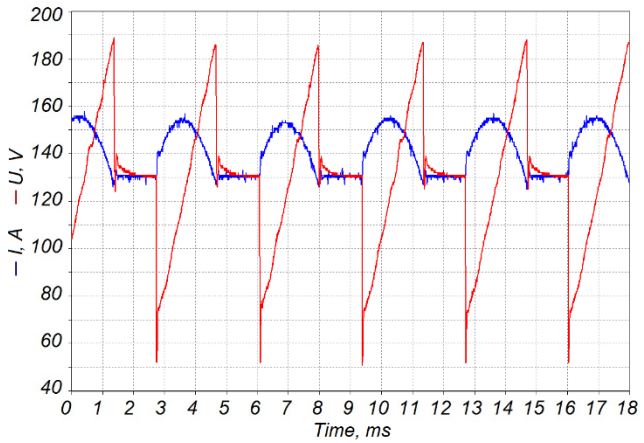

Fig. 10. Waveforms of the DCS800 converter output voltage and current at the idle run

The commissioning of the discharge rolling table drive gave opportunity to conduct series of measurements. One of them shows work of individual thyristors of the 2 × 6T bridge. The graph in Fig. 10 presents waveforms of the voltage (red line) and current (blue line) drawn by the six armature circuits of the separately excited motors. The graph in Fig. 10 shows deep decrease of the motors angular velocity down to 31 rpm, which is equivalent to voltage of 13 V on the converter DC bus. The load voltage and current measurement was carried out at the idle run of the motors with no slabs conveyed.

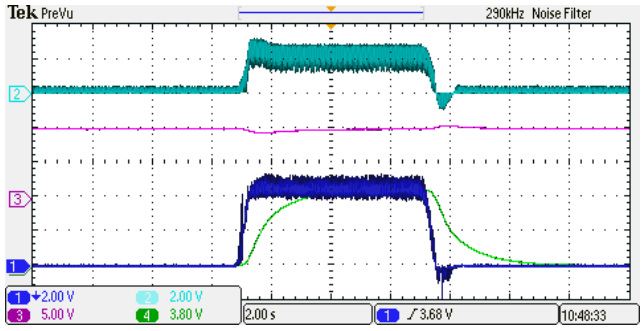

Fig. 11. Current waveform (I_M), angular speed (n), load torque (I_M) and estimated torque (T_{ES}) in the case of the first load

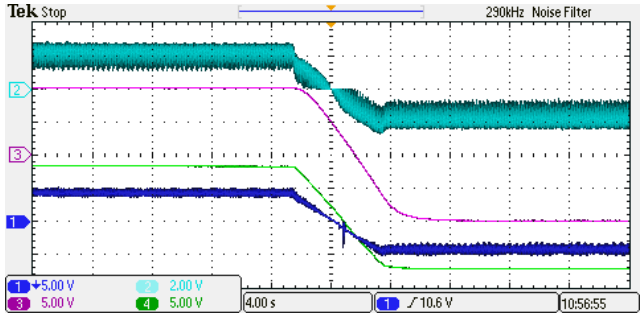

Fig. 12. Current waveform (I_M), angular speed (n), load torque (I_M) and estimated torque (T_{ES}) in the case of the second load

The measurements of the actual load torque and its corresponding estimated value of electromagnetic torque generated by the converter were conducted during the transport of hot slabs

DOI 10.1515/ama-2015-0016

to the break-down rolling stand. The results of experiment involved two tests:

1) pulse roller load during the slab transport (Fig. 11);
2) load of a roller in a rolling table at the time of the slab transport direction change (Fig. 12).

In both cases clear differences between the actual torque T_L and the estimated torque T_{ES} are visible. Such differences occur especially in transient states (load torque impact, slowdown and change of the motor rotation direction). In steady states both values are very close and the absolute error does not exceed 2 percent

$$\delta = \frac{|T_L - T_{ES}|}{T_L} \ 100 \ \% \leq \ 2\% \qquad (9)$$

5. SUMMARY

The drive system described in the paper was implemented in the modernized rolling line. It meets all technical requirements of a modern plate rolling process.

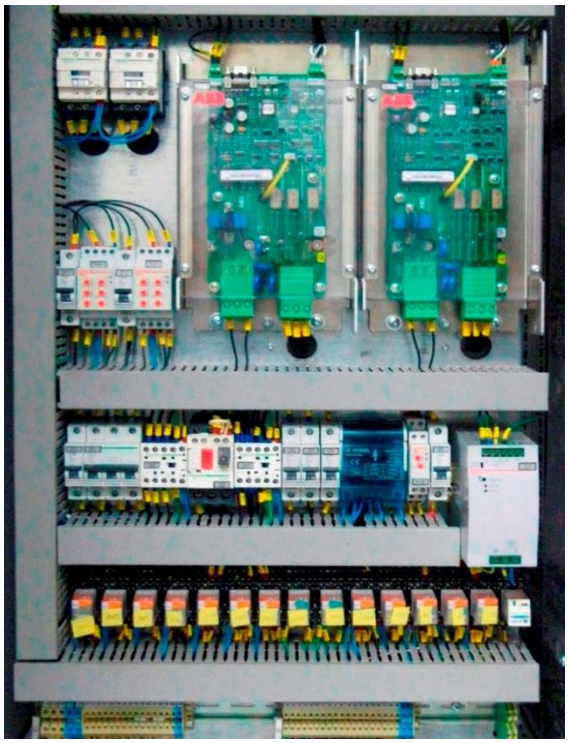

Fig. 13. Interior of the field circuits power supply cubicle with the FEX4 boards

The photo in Fig. 13 shows interior of the cubicle with six FEX4 boards for powering the field circuits of the rolling table drive motors. On the basis of the drive implementation tests it can be stated that it is possible to supply a group of separately excited DC motors from a single reverse thyristor converter connected with several separate controllers of the motors field currents. In the presented case those controllers communicate with the main converter via the DSL link. Such a scheme allows for correction of the field currents of individual motors which results in very good synchronization of the motors and rolls speeds.

The presented discharge rolling table drive has good dynamic properties. The change of the slab conveying direction for the angular speed setting of almost 50% of the full range takes 1 second (see Fig. 8) and the dynamic current peak during that reverse exceeds 5 times the steady state current.

The DriveWindow software (Gała et al., 2003) is a modern and effective tool that aids practical application of the drive and facilitates carrying out various tests necessary during commissioning of the DCS and ACS drive systems.

REFERENCES

1. **Abu-Rub H., Guziński J., Jąderko A., Krzemiński Z.** (2004), Practical Realisation of New Method of Synchronisation for Controlled Rectifier, *International Conference on Power Electronics, Intelligent Motions and Power Quality PCIM 2004*, Nuremberg, Germany, 533 – 538.
2. **Abu-Rub H., Guziński J., Jąderko A., Krzemiński Z.** (2005), Digital Implementation of a Novel Controlled Rectifier Synchronization Method, *Electric Power Components and Systems*, Vol. 33 (10), 1123 – 1135.
3. **Dobrucki W., Gregorczyk R., Świątoniowski A., Zawada S.** (1991), *Introduction to design and operation of rolling mills – Calculations and experiments,* Wydawnictwo AGH, Kraków, (in Polish).
4. **Friedli T., Hartmann M., Kolar J.W.** (2014), The Essence of Three-Phase PFC Rectifier Systems—Part II, *IEEE Transactions on Power Electronics*, Volume: 29 (2), 543- 560.
5. **Gała M., Rak J., Kępiński M., Jagieła K.** (2009), Application of Drive Window software for AC and DC drives operation states diagnostics, *Electric Machines - Problem Issues*, No.82/2009, BOBRME KOMEL Katowice, 33-38, ISSN 0239-3646, (in Polish).
6. **Guziński J., Diaguet M., Krzemiński Z., Lewicki A., Abu-Rub H.** (2009), Application of speed and load torque observers in high-speed train drive for diagnostic purposes, *IEEE Transactions on Industrial Electronics*, Vol 57(2), 565-574.
7. **Jagieła K.** (1997), Theoretical issues in calculation of load parameters of rolling table motors. Research Notes of Lvov State University of Technology – Electrical power engineering and electro-mechanical systems Systemy, № 340, 142-147, (in Ukrainian).
8. **Jagieła K.** (2003), Model of metallurgical discharge rolling table, *Electrical Review*, No.6/2003, 448- 452.
9. **Jagieła K., Gała M.** (2008), Setting screw electrical drive of the vertical milling cage using MASTER– FOLLOWER control, *IX Inter-national Scientific Conference „New Technologies in Metallurgy and Materials Engineering"*, Metallurgy Committee PAS, Czestochowa University of Technology, Vol. 1, 146-149 (in Polish).
10. **Kolar J. W., Friedli T.** (2013), The Essence of Three-Phase PFC Rectifier Systems—Part I, *IEEE Transactions on Power Electronics*, Volume: 28 (1), 176-198.
11. **Michael C.A., Safacas A.N.** (2007), Dynamic and Vibration Analysis of a Multimotor DC Drive System With Elastic Shafts Driving a Tissue Paper Machine, *IEEE Transactions on Industrial Electronics*, Vol. 54 (4), 2033-2046.
12. *Multifex motor control for roller tables DCS800 Drives (20 to 5200 A)*, ABB Automation Products, Germany, 05-2008.

DETECTION OF TWO-PHASE FLOW PATTERNS IN A VERTICAL MINICHANNEL USING THE RECURRENCE QUANTIFICATION ANALYSIS

***Romuald MOSDORF, *Grzegorz GÓRSKI**

*Faculty of Mechanical Engineering, Bialystok University of Technology, Wiejska 45 C, 15-351 Bialystok, Poland

r.mosdorf@pb.edu.pl, grzesgor@o2.pl

received 6 October 2014, revised 20 July 2015, accepted 22 July 2015

Abstract: The two-phase flow (water-air) occurring in square minichannel (3x3 mm) has been analysed. In the minichannel it has been observed: bubbly flow, flow of confined bubbles, flow of elongated bubbles, slug flow and semi-annular flow. The time series recorded by laser-phototransistor sensor was analysed using the recurrence quantification analysis. The two coefficients:Recurrence rate (RR) and Determinism (DET) have been used for identification of differences between the dynamics of two-phase flow patterns. The algorithm which has been used normalizes the analysed time series before calculating the recurrence plots.Therefore in analysis the quantitative signal characteristicswas neglected. Despite of the neglect of quantitative signal characteristics the analysis of its dynamics (chart of DET vs. RR) allows to identify the two-phase flow patterns. This confirms that this type of analysis can be used to identify the two-phase flow patterns in minichannels.

Key words: Two-Phase Flow, Recurrence Plot, Recurrence Quantification Analysis

1. INTRODUCTION

The identification of flow patterns in minichannels often depends on the subjective evaluation of the observer and used experimental technique (Zhao and Rezkallah,1993; Wongwises and Pipathattakul, 2006; Chen et al., 2006). Wang et. al in the paper (Wang et al., 2010) show that the non-linear analysis (Lempel–Ziv complexity and approximate entropy) of data from mini-conductance probe array and vertical multielectrode array conductance sensorenables the identification of flow patterns of the oil-gas-water mixture. The results of non-linear analysis of temperature and pressure fluctuations in microchannels are discussed by Mosdorf et.al in the paper (Mosdorf et al., 2005). The processes responsible for the appearance of pressure and temperature chaotic oscillations such as: nucleation, stability of bubbly flow, vapour core stability and vapour-phase flow stability are discussed. In the paper (Wang et al., 2003) it has been used the non-linear analysis of the pressure fluctuations to identify the flow patterns of air in water.Three kinds of flow patterns including bubble flow, churn flow and annular flow in the inlet tube were investigated by detecting time series of differential pressure. Hurst exponent, largest Lyapunov exponent and correlation dimensions have been used.In the paper (Zong et al., 2010) it has been shown that the methods characterizing the non-linear dynamics of the flow of oil-water are useful for identification of the flow patterns and for assessment of the complexity of these patterns. The recurrence quantification analysis and chaotic attractor geometry morphological description have been used for signal from vertical multi-electrode array. The results show that the proposed method of data analysis describes the flow structure complexity. Jin et al. in the paper (Jin et al., 2003) show that the correlation dimension and Kolmogorov entropy are sufficient to identify the flow patterns. Faszczewski et al.,(2012) used the recurrence plot method to analyse the flow patterns in a vertical mini channel.It has been shown that this method allows us to determine the parameters which define the borders between flow patterns.

The subject of the research is the development of method for identifying the types of flow patterns which occur during the movement of the gas-liquid mixture in the vertical minichannel. Usually the non-linear methods of data analysis require the long time series for calculation of different coefficients which characterize the system dynamics. In the present paper the proposed method is based on the recurrence quantification analysis. Such method does not require the analysis of long time series. Therefore,it can be useful for implementation in the sensors which automatically can identify the flow pattern. The main aim of the paper was the assessment if the signal, which qualitatively estimates the presence of air inside the minichannel, can be used for two-phase flow pattern identification. The laser– phototransistor sensor has been used for qualitative assessment of the presence of bubbles or slugs in the minichannel.

2. EXPERIMENTAL SETUP

In Fig. 1 the schema of experimental stand is presented. Due to the size of the minichannel the obtaining the bubbly flow inside it requires the usage of a special generator of mini bubbles (8 – Fig. 1a). The proportional pressure regulator (Metal Work Regtronic with an accuracy of 1 kPa) was used to maintain the constant overpressure in the supply tank (10 – Fig. 1a) - the overpressure was 50 kPa. Flow patterns were recorded with using the Casio EX-F1 digital camera at 1200 fps (336 x 96 pixels). Pressure difference between the inlet and outlet of minichannel was measured using the silicon pressure sensor MPX12DP (range 0–10 kPa, sensitivity 5.5 mV/kPa, response time 1 ms, accuracy ±0.05 kPa).

During the experiment it was analysed the data recorded for different flow patterns (water-air at 21^{o} C) in a square channel 3x3 mm.

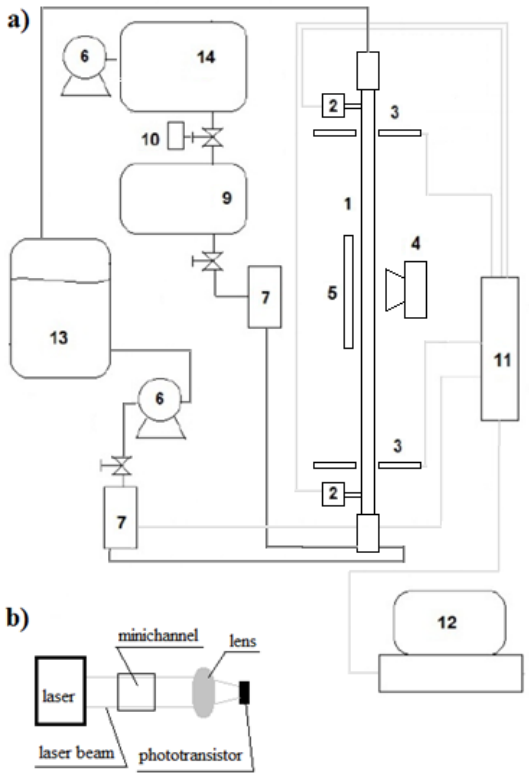

Fig. 1. Scheme of experimental stand. 1. minichannel, 2. pressure sensors (MPX12DP), 3. laser-phototransistor sensor. 4. Casio EX-FX1 camera, 5. lighting, 6. pumps (air or water), 7. flow meters. 8. mini bubbles generator, 9. air tank, 10. automatic valve to maintain a constant pressure in the tank 9, 11. data acquisition station (DT9800), 12. computer, 13. water tank, 14 air tank

The content of the minichannel (bubbles or liquid) has been qualitatively assessed using the laser–phototransistor sensor (3 – Fig. 1a). The schema of laser-phototransistor sensor is presented in Fig. 1b. The sensor consisted with a laser which generated the laser beam with a diameter of 3 mm, the lens and phototransistor sensor placed in focal point of lens. Bubbles inside the minichannel bend the light which modifies the light intensity on the phototransistor. Sampling frequency was equal to 1 kHz.

3. DATA ANALYSIS

In Fig. 2 it has been shown the map of two phase flow patterns recorded during the experiment for different air and water flow rates. In the minichannel it has been observed: flow of isolated bubbles, flow of confined bubbles, flow of elongated bubbles, slug flow and semi-annular flow. Isolated bubbles have been observed for q_a in the range from 0.001 l/min to 0.0254 l/min. For q_a equal to 0.0334 l/min and 0.0424 l/min the isolated bubbles are grouped. For q_a equal to 0.1 l/min and 0.2 l/min the confined bubbles appear in the minichannel. Slugs flow appears for q_a equal to 0.3 l/min and 0.4 l/min and semi-annular flow appears for q_a = 0.5 l/min.

In Fig. 3 it has been shown the examples of recorded signals for different air volume flow rates (q_a) and constant liquid volume flow rate (q_w). When the channel is filled with water, the sensor generates a high voltage signal (about 3.5 V). Such situation is visible in Fig.3a-h. Voltage drops below the maximum voltage level indicate that bubbles are in the minichannel. Such process is visible in Fig.3a and b (small bubbles are in the channel). The appearance of the large bubbles in minichannel causes the significant voltage drops. Such process is visible in Fig.3c-h. When the bubbles group, then between the groups of bubbles the minichannel is filled with water without bubbles. Such process is visible in Fig.3e-h. When the confined bubble or slug occurs inside the minichannel, then the sensor generates a low voltage signal (about 3 V). However, when the front of slug or confined bubble is passing through the laser beam, then the sensor voltage level drops to about 2 V. Such process is visible in Fig.3i, j. When the minichannel is filled in with long slugs, then the sensor generates the signal shown in Fig.1k-m. In this case the signal fluctuations are caused by the slug diameter fluctuations. The above properties of laser - phototransistor sensors allow use the signal from sensors for qualitative assessment of the presence of bubbles or slugs in the minichannel.

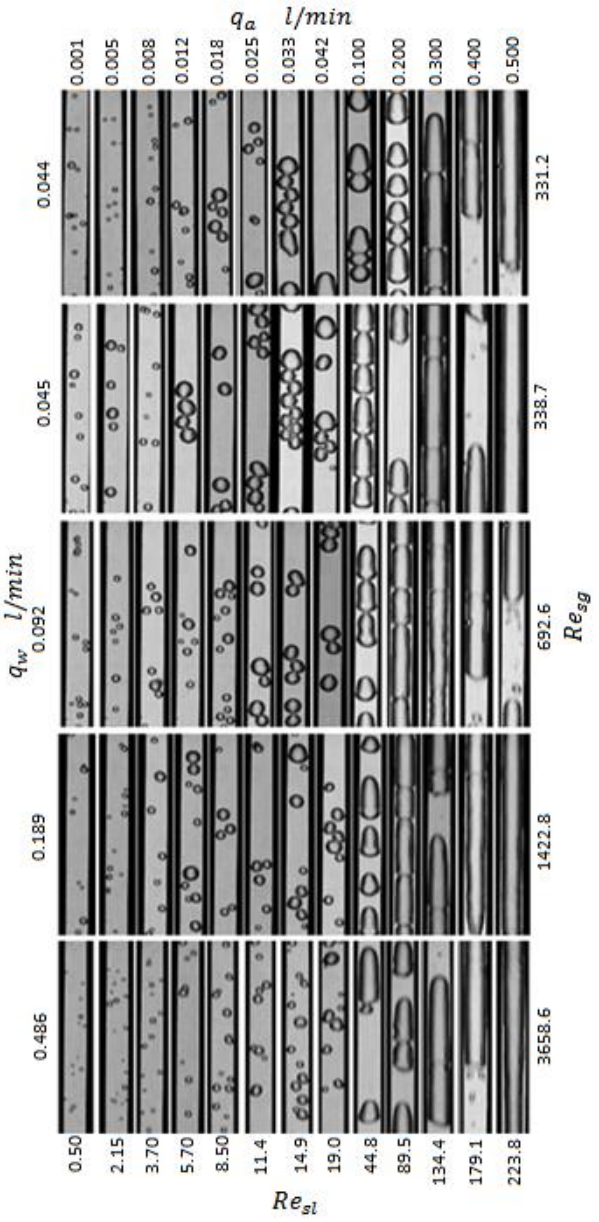

Fig. 2. The map of two phase flow patterns recorded during the experiment for different air and water flow rates

The identification of flow patterns in minichannels often depends on the subjective evaluation of the observer and used experimental technique. For parameters characterizing the transition between flow patterns the two phase flow is usually unsteady. In such situation the criteria based on average values of the various parameters are not suitable for identification the border between flow patterns. Fig 4 presents the mean values of recorded data for different water flow rates. Non-linear character of function $\bar{x}(q_a)$ makes impossible the identification of the two phase flow pattern in minichannel based on the sensor data. The same values of $\bar{x}$ occur for different flow patterns. Therefore, the flow pattern identification requires the analysis of signal dynamics.

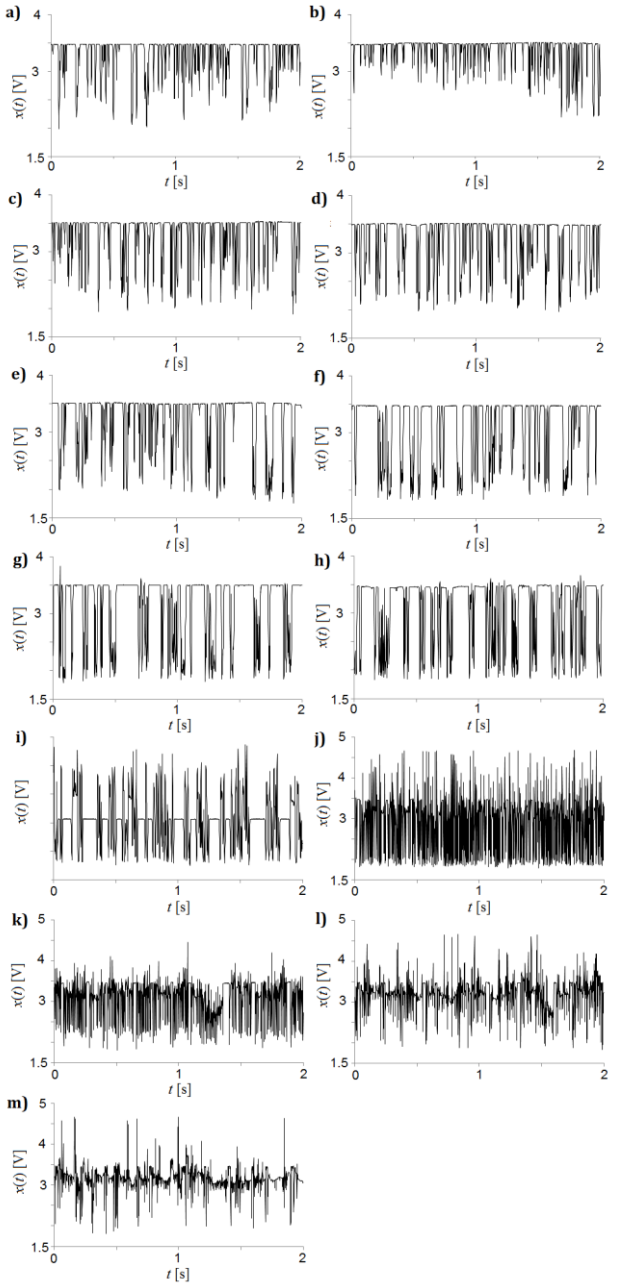

Fig. 3. Example of time series of pressure drop recorded during the experiment for q_w = 0.044 l/min. a) q_a = 0.001 l/min, b) q_a = 0.00478 l/min, c) q_a= 0.00827 l/min d) q_a = 0.0127 l/min. e) q_a= 0.0188 l/min, f) q_a= 0.0254 l/min, g) q_a= 0.0334 l/min h) q_a= 0.0424 l/min. i) q_a= 0.1 l/min, j) q_a = 0.2 l/min, k) q_a= 0.3 l/min l) q_a= 0.4 l/min. m) q_a = 0.5 l/min

4. RECURRENCE QUANTIFICATION ANALYSIS

The analysis of attractor reconstructed from single time series of experimental data generated by non-linear dynamical system gives us information about the properties of the system such as system complexity and its stability. In non-linear analysis the reconstruction of attractor in a certain embedding dimension is carried out using the stroboscope coordination (Marwan et al. 2007). In this method the subsequent co-ordinates of attractor points are calculated basing on the subsequent samples, between which the distance is equal to time delay. The time delay is a multiplication of time between the samples.

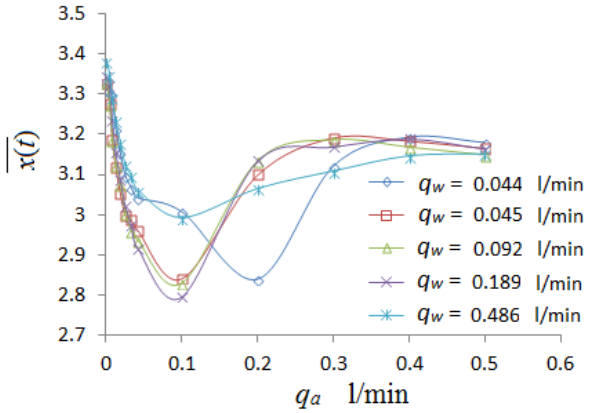

Fig. 4. The mean values of recorded data for different water flow rates

Recurrence plot is a technique of visualization of the recurrence of states x_i in m-dimensional phase space. The states x_i are points of attractor reconstructed in the m-dimensional phase space. The recurrence of states at time i and at a different time j is marked with black dots in the 2D plot, where both axes are time axes. The recurrence plot is defined as (Marwan et al. 2007):

$$R_{i,j} = \Theta\left(\varepsilon - \left\|x_i - x_j\right\|\right),\ x_i \in \Re^m,\ i,j - 1 \ldots N \qquad (1)$$

where N is the number of considered states x_i, ε is a threshold distance, $||\cdot||$ is a norm and $\Theta(\cdot)$ is the Heaviside function.

The researches based on the concept of recurrence plot are widely used for analyses of complex systems, especially for multiphase flow systems. In the paper (Zbilut, 2008) it has been shown that the Fourier transformation based on the recurrence plot can be used for the analysis of dynamics of higher dimensional spaces. Such analysis cannot be carried out by standard Fourier transformation. In the paper (Gaoet al.; 2013) the signals from multisector conductance sensor has been used for analysis of two different horizontal oil-water stratified flow patterns. The multivariate recurrence networks method and cross-transitivity has been used for recorded data. It has been shown that proposed method identifies the transition from a stable to an unstable state. In the paper (Yang al.,2015) the combustion instabilities in a diesel engine have been analysed. The combustion complexity has been analysed using the: delay-coordinate embedding, recurrence plot, Recurrence Quantification Analysis, correlation dimension, and the largest Lyapunov exponent. It has been found that the combustion system of diesel engine is a low-dimensional chaotic system. In the paper (Mosdorf et al., 2015) the pressure drop fluctuations in two-phase flow (water-air) in square minichannel (3x3 mm) has been analysed. The two coefficients of Recurrence Quantification Analysis: recurrence period density entropy and

DOI 10.1515/ama-2015-0017

transitivity have been used for identification of differences between the dynamics of two-phase flow patterns. It has been shown that the recurrence network analysis of dynamics of pressure drop fluctuations can be used for identify the two-phase flow patterns in minichannels.

In the paper, the time delay has been calculated based on the mutual information algorithm (Marwan et al., 2007). Embedding dimension has been estimated using the False Nearest Neighbours algorithm (Marwan et al., 2007).

The quantitative recurrence analysis generates the coefficients which describe the dynamics of two-phase flow patterns. Recurrence rate, RR, is a measure of the percentage of recurrence points in the recurrence plot. The value of *RR* corresponds to the correlation sum. It is defined as follows (Marwan et al. 2007):

$$RR = \frac{1}{N^2}\sum_{i,j=0}^{N} R_{i,j} \tag{4}$$

The number of points which appears in the recurrence plot depends on the value of ε. Recurrence rate is a non-linear function of ε. In Fig. 5 it is presented the function *RR*(ε) obtained for time series under consideration. Strong nonlinearity of function *RR*(ε) is visible for the small value of ε. For higher value of ε the nonlinearity becomes smaller (the function becomes quasi linear). It has been assumed that the lowest value of ε in the linear part of function *RR*(ε) is a proper value of ε for the reconstruction of recurrence plot. For time series under consideration it is equal to 3.

In Fig. 6 it has been shown the examples of recurrence plots of recorded data for different flow rates. The calculations have been made using the Matlab Toolbox (Marwan 2014). The used algorithm normalizes the analysed time series before calculating the recurrence plots. Therefore, in the analysis the quantitative signal characteristics was neglected.

In the recurrence plot a line parallel to main diagonal line occurs when a segment of the trajectory runs parallel to an another segment and the distance between trajectories is less than ε. The length of this diagonal line is determined by the duration of this phenomenon. A vertical (horizontal) line indicates a time in which a state does not change or changes very slowly. The diagonal lines (structures) periodically occurred in the recurrence plot are characteristic for periodic system (Marwan et al., 2007).

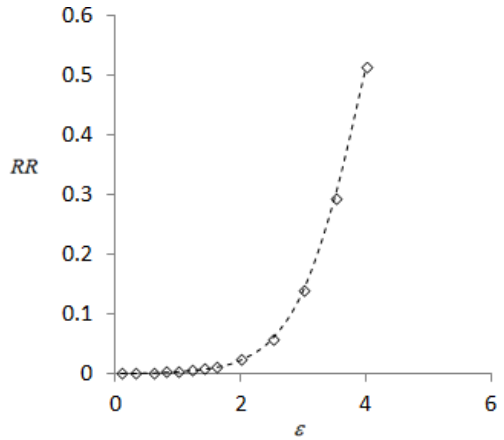

Fig. 5. Recurrence rate, RR, vs ε for the time series recorded from the laser-phototransistor sensor for q_w = 0.059 l/min, q_a= 0.0127 l/min. The calculations have been made using the Matlab Toolbox (Marwan,2014)

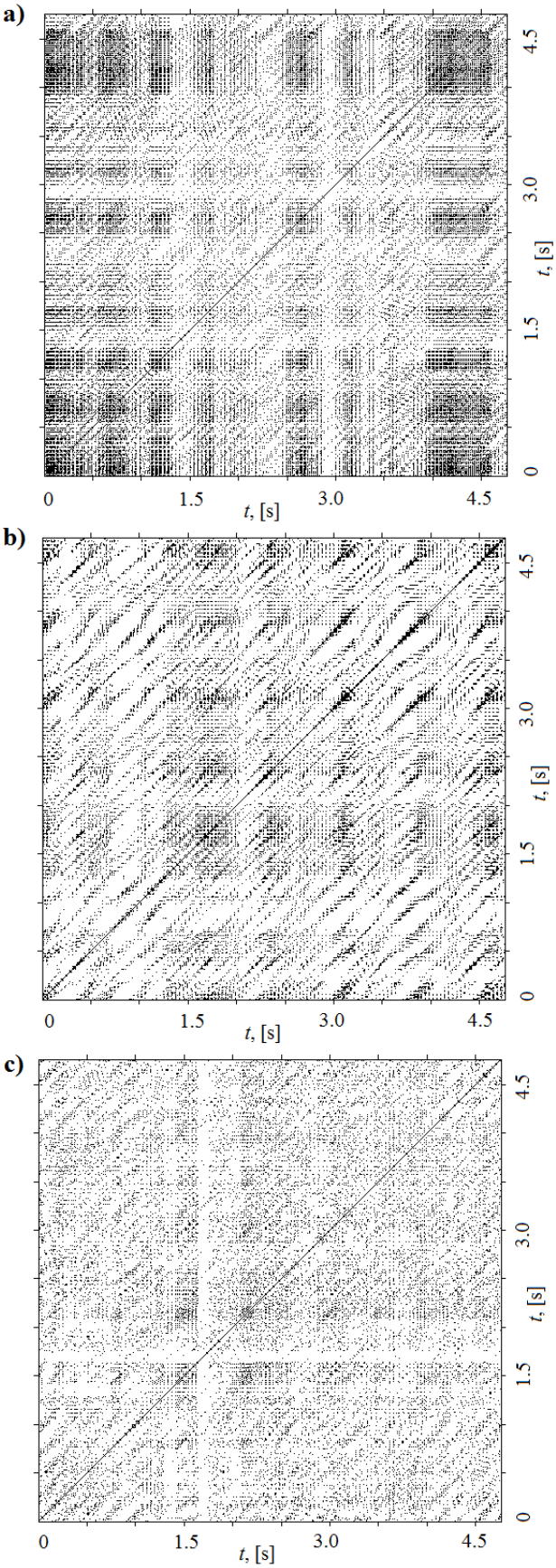

Fig. 6. Recurrence plots for embedding dimension 6 and time delay 1 q_w = 0.044 l/min, a) q_a = 0.001 l/min, b) q_a = 0.0424 l/min, c) q_a = 0.1 l/min.The calculations have been made using the Matlab Toolbox (Marwan,2014)

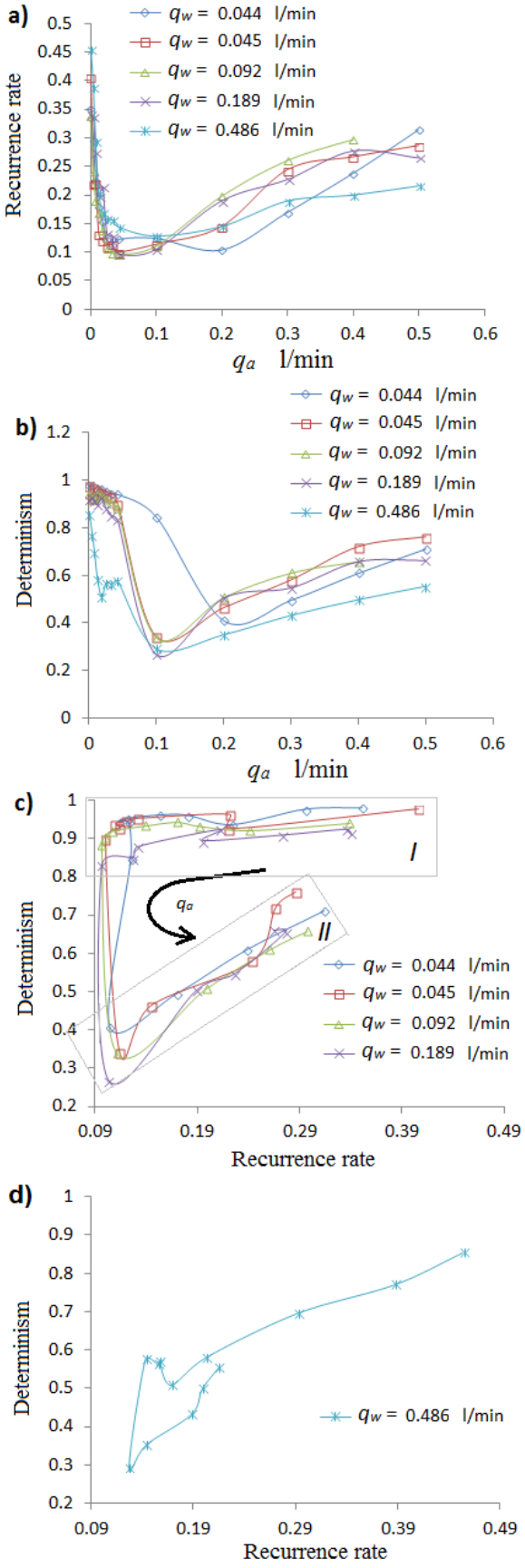

Fig. 7. Recurrence rate and Determinism for the different air and water flows. a) Recurrence rate. b) Determinism. c) Determinism vs. Recurrence rate. d) Determinism vs. Recurrence rate for q_w = 0.486 l/min. The calculations have been made using the Matlab Toolbox (Marwan,2014)

The characteristics of diagonal lines are described by Determinism (DET) coefficient:

$$DET = \frac{\sum_{l=lmin}^{N} lP^{\varepsilon}(l)}{\sum_{i,j}^{N} R_{i,j}^{m,\varepsilon}} \tag{5}$$

where $P(l)$ is the distribution of the lengths of diagonal structures and N is the absolute number of diagonal lines;

The 13 coefficients characterizing the dynamics of the recorded signal were determined with using the Matlab Toolbox (Marwan;2014). The analysis of changes of those coefficients values together with flow pattern changes allows us to choose the two coefficients, whose values vary significantly over the considered range of parameters and unambiguously characterize two-phase flow patterns. These two coefficients (RR, DET) have been used for identification of differences between the dynamics of recorded data.

The functions of $RR(q_a)$ and $DET(q_a)$ are shown in Fig.7a and b. In Fig.7c the chart of DET vs. RR for q_a in the range from 0.044 l/min to 0.189 l/min is presented. The lines indicate the order of points, black arrow indicates the direction of q_a increase. The two rectangles marked with numbers (I, II) identify the two types of different flow patterns.

In the rectangle I there are located the points which characterize the bubbly flow. In the right side of the rectangle I there are located the points which characterize the bubbly flow with small isolated bubbles. In the left side of rectangle there are located points which are created by flow of grouped bubbles. In all cases under considerations the bubble diameters are less than the channel size.

In the rectangle II there are located the points characterizing the flow patterns where the bubbles fulfill the channel. Here there are located the points created by: confined and elongated bubbles flow, slug flow and semi-annular flow. In the left side of the rectangle II there are points characterising the flow of confined bubbles, but in the right side of the rectangle there are located points created by semi-annular flow.

The chart DET vs. RR for q_w = 0.486 l/min is presented separately in Fig.7d because the points of this chart do not lie within the rectangles presented in Fig.7c. This is probably caused by too low sampling frequency for flow velocity for q_w = 0.486 l/min. Therefore, we can conclude that for the water flow rates in the range from 0.044 to 0.189 l/min the chart DET vs. RR (presented in Fig. 7c) can be used for two phase flow identification.

5. CONCLUSIONS

The proposed method for identifying the two-phase flow patterns is based on the analysis of the dynamics of the measurement signal.

The Recurrence Rate which has been used in the analysis is a measure of the probability of the recurrence. Such probability decreases with the increase of the air volume flow rate (Fig.7c). Such decrease is accompanied by increase of bubblediameters. For the slug flow the increase of air volume flow rate causes the increase of recurrence rate. It means that the number of recurrences increases.

The determinism (DET) is a measure of predictability of the system. For deterministic and periodic system, all points of RP belong to the diagonal lines. For white noise all points of RP are isolated points. Increase of the DET means that the system becomes more predictable. In bubble flow the predictability of the

system does not change significantly (Fig.7c). The slug flow appearance in the minichannel rapidly decreases the predictability of the system (the length of the slugs and distance between them change chaotically). Further increase of the air volume flow rate makes the system more predictable (the length of the slugs and distance between them become more predictable). In the paper it has been shown that the simple laser– phototransistor sensor which can qualitatively assess the presence of bubbles or slugs in the minichannel can be used for identification of two phase flow patterns.

The RP analysis normalizes the signal so the average values of the signal do not affect the results of the analysis. Despite of the neglect of quantitative signal characteristics the qualitative analysis of its dynamics allows us to identify the two-phase flow patterns. This confirms that this type of analysis can be used to identify the two-phase flow patterns in minichannels in the relatively wide range of liquid and air flow rates. The final verification of the proposed method requires much larger number of analyses of different types of two-phase flows.

REFERENCES

1. **Chen L., Tian Y.S., Karayiannis T.G.** (2006), The effect of tube diameter on vertical two-phase flow regimes in small tubes, International *Journal of Heat and Mass Transfe*r, vol. 49, 4220-4230.
2. **Faszczewski M., Górski G., Mosdorf R.** (2012), A*pplying recurrence plots to identify borders between two-phase flow patterns in vertical circular mini channel*, Acta Mechanica et Automatica, Vol. 6, No.1, 31-36.
3. **Jin N.D., X.B. Nie, Y.Y. Ren, Liu X. B.**(2003), Characterization of oil/water two-phase flow patterns based on nonlinear time series analysis *Flow Measurement and Instrumentation*, Vol. 14, 169-175.
4. **Zbilut J. P., Marwan N.**(2008), The Wiener-Khinchin theorem and recurrence quantification, *Physics Letters* A 372, 6622–6626.
5. **Marwan N.,** (2014), *Cross Recurrence Plot Toolbox for Matlab*, Ver. 5.15, Release 28.10, http://tocsy.pik-potsdam.de.
6. **Marwan N., Romano M. C., Thiel M., Kurths J.**. (2007), *Recurrence Plots for the Analysis of Complex Systems*, *Physics Reports*, 438 (5-6), 237-329.
7. **Mosdorf R., Cheng P., Wu H.Y., Shoji M.** (2005), Non-linear analyses of flow boiling in microchannels, *International Journal of Heat and Mass Transfer*, 48, 4667–4683.
8. **Mosdorf R., Górski G.** (2015), Detection of two-phase flow patterns using the recurrence network analysis of pressure drop fluctuations, *International Communications in Heat and Mass Transfer*, Vol.64 , 14-20.
9. **Wang S.F., Mosdorf R., Shoji M.** (2003), Nonlinear analysis on fluctuation feature of two-phase flow through a T-junction, *International Journal of Heat and Mass Transfer*, 46, 1519–1528.
10. **Wang Z.Y., JinN.D., GaoZ.K., ZongY.B., WangT.** (2010), Nonlinear dynamical analysis of large diameter vertical upward oil–gas–water three-phase flow pattern characteristics, *Chemical Engineering Science*, 65, 5226–5236.
11. **Wongwises S., Pipathattakul M.** (2006), Flow pattern, pressure drop and void fraction of two-phase gas–liquid flow in an inclined narrow annular channel, *Experimental Thermal and Fluid Science*, 30, 345-354.
12. **Yan-Bo Zong, Ning-De Jin, Zhen-Ya Wang, Zhong-Ke Gao, Chun Wang**, (2010, Nonlinear dynamic analysis of large diameter inclined oil–water two phase flow pattern, *International Journal of Multiphase Flow*, 36, 166–183.
13. **Yang L. P., Ding S. L., Litak G., Song E. Z., Ma X. Z.** (2015), Identification and quantification analysis of nonlinear dynamics properties of combustion instability in a diesel engine, *Chaos*, 25(1), 013105
14. **Zhao L., Rezkallah K.S.** (1993), Gas–liquid flow patterns at microgravity condition,International Journal Multiphase Flow, 19, 751-763.
15. **Zhong-Ke Gao, Xin-Wang Zhang, Ning-De Jin, Reik V. Donner, Norbert Marwan and Jürgen Kurths (**2013), Recurrence networks from multivariate signals for uncovering dynamic transitions of horizontal oil-water stratified flows, *Europhysics Letters*, 103 (5), 1-7.

Acknowledgement: The project was funded by the National Science Centre, Poland - the number of decision: DEC-2013/09/B/ST8/02850

COMPARATIVE ANALYSIS OF TWO METHODS OF ASSESSMENT WEAR OF DENTAL MATERIALS

Sylwia M. WOJDA*

*Białystok University of Technology, Faculty of Mechanical Engineering
ul. Wiejska 45C, 15-351 Białystok, Poland

sylwia.wojda9@gmail.com

received 12 October 2014, revised 23 July 2015, accepted 24 July 2015

Abstract: Wear of dental materials used for permanent dental fillings has a significant impact on their lifetime. Wear products generated during chewing process involving direct tribological contact between a composite and tooth enamel can cause damage not only to enamel itself but also to the entire tooth structure thus affecting the patient's the health. It is essential therefore to assess the process of wear rates as well as the usefulness and effectiveness of the method used to measure these values. As there are a number of different methods used to quantify the loss of dental materials subjected to friction, eg.: scanning digital 3D models of dental casts, confocal microscope scanning or profilographometer measurements, the authors chose to analyze two selected research methods using confocal microscopy and profilographometer to assess their effectiveness. Two commercially available composite dental materials, i.e. ES and FFE previously subjected to friction tests in contact with human dental enamel, were used for the analysis.

Key words: Tooth Enamel, Dental Material, Wear, Friction, Profilografometer, Confocal Microscope

1. INTRODUCTION

Research on dental materials, in the context of their tribological properties, has been playing an extremely significant part in prolonging their durability or lifetime. Despite numerous modifications to their composition and emergence of new composite materials on the market, they still fail to match the working properties of natural enamel (Lambrechts et al., 2006). This is the main reason why research is being continued to develop new and better dental materials. Currently fillings of dental hard tissues used for in natural contact with the opposing teeth are subject to abrasion, chipping and even falling out. They can also cause excessive wear of the tooth enamel remaining antagonistically to be filled. As a result the wear products penetrate into the human organism posing a health risk. Research work on the wear of permanent dental filling materials is of substantial importance for the development of effective methods used to measure wear rates (Ferracane, 2006). The materials such as dental composites are characterized by porosity that gives them a certain absorbency of liquids (Malacarne et al., 2006), for example, human saliva in the oral cavity conditions. As we know, absorbency determines the absorption of the material, i.e. the ability to absorb liquids. Thus, for example, the mass methods, which are also used to evaluate the loss of such materials, are not reliable. That is why new research methods are being developed to assess wear values. To determine the usefulness of the applied method, we use specific statistical procedures to analyze the obtained information on dental materials. There are measurements of volumetric loss of dental materials making use of such methods as 3D digital scanning of dental casts (Park et al., 2014), confocal microscope, profilographometer (Paepegaey et al., 2013) and another.

In this paper the authors analyse tribological wear of two composite dental materials: Estelite Sigma and FulFil Extra in contact with human enamel. The volumetric loss of the samples has been measured using a confocal microscope and profilographometer. The accuracy of the applied the methods is evaluated.

2. MATERIALS

In tribological tests samples of dental composite materials shaped in the form of a truncated cone and countersamples made of human dental enamel were used (Fig. 1). The analysis involved two dental materials used for permanent fillings, namely Estelite Sigma (ES) (Tokuyama Dental, Japan) - light-cured composite containing fillers in the form of spherical particles of submicron size (0.2 - 5 μm) and and FulFil Extra (FFE) (DENTSPLY International Inc., USA) – micro-hybrid, light-cured composite with filler of the particle size varying from 0.04 to 5 μm. In all 20 samples of each of the materials were tested. The materials had been previously formed in layers in aluminum-rimmed frames and cured with a polymerization lamp. Next, they were grinded with upward gradation abrasive paper and finally polished using an emulsion containing aluminum oxide.

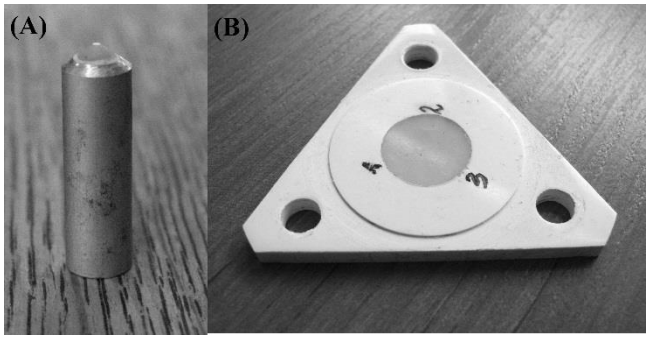

Fig. 1. View of A) countersample, (B) sample

DOI 10.1515/ama-2015-0018

3. METHODS

The tests were conducted at the Faculty of Mechanical Engineering of the Białystok University of Technology on a specially constructed pin on disc type tribometer designed for studies involving friction in vitro (masticatory simulator) (Fig. 2). The tribometer made it possible to subject the samples to both half-sine cyclic load tests and also reversing movements of the countersample. A detailed description of the device can be found in the authors' another work (Sajewicz and Kulesza, 2007).

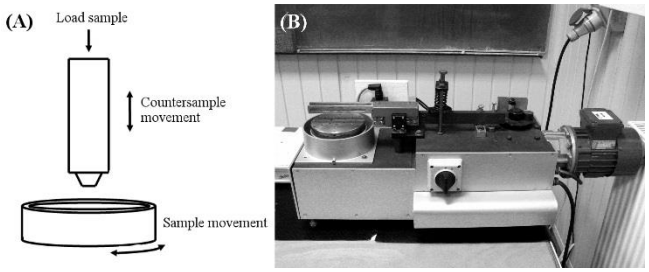

Fig. 2. View of (A) sample and countersample movements, (B) tribometer type of pin on disc

3.1. Evaluation of Wear with Profilografometer

In order to assess the wear rate of the researched material, a special method of measuring the loss in the material was used. The measuring device Surftest SJ-500 (Fig. 3) manufactured by Mitutoyo was mounted on a solid granite basis with a column.

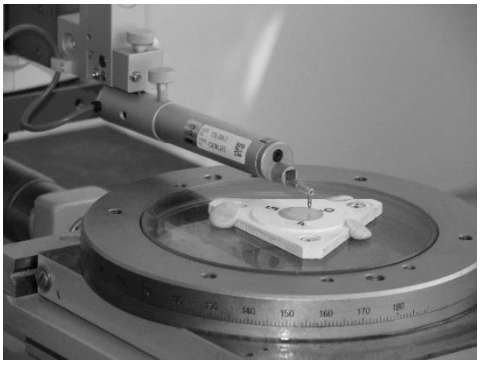

Fig. 3. Profilografometer Surftest SJ-500 Mitutoyo with visible micrometer table and mounted sample of dental material

Surftest SJ-500 is a very high-precision instrument for measuring surface texture. The accompanying software-Formtracepack made it possible to control the device and setup measurements to ensure efficient automation of the measurements. During the tests the needle deflection was measured with respect to the precision drive track. Because the profilographometer's arm moves only in X and Z directions, it was necessary to use additional equipment in the form of a micrometer table, which made it possible to perform a manual shift towards Y. During the measurements the tested material was rigidly mounted on the micrometer table. First a great number of measurements of sample profiles with a step 0.05mm was carried out (Wróblewska, 2014). Due to the fact that the profilographometer performs no automatic operations in the Y-axis, every single record of a profile in Formtracepack program has the Y coordinate equal zero. To avoid profile overlapping and obtain spatial data, it is required to replace zero coordinates on Y axis with the actual manual shift values. Thus the adopted step is added to the Y value in the program's text editor, increasing the value by 0.05 for each subsequent profile. In order to compress data of one wear track (for many profiles) in one file, they were imported into CATIA software using digitized shape editor environment. Next the data were saved in the IGES format. The obtained data in the form of a point cloud were imported into the Rhinoceros program in which the patch operation from the menu was used. The patch, with suitably chosen parameters, was laid over the point cloud so that the created surface did not differ too much from the profiles. Next the file was saved in the IGES format and opened in Solid Works software .Here a base surface was created on the vertices of the imported surface. Then another surface was created, this time by moving it by 0.1mm from the base surface. Next a sketch on the edges of the base area was drawn and base adding operation was performed choosing the direction: to the surface (select the surface imported from tree operation). Then another sketch on the edges of the base area was created using the command of extruded cut in two directions: A – 0.1mm and B – 0.098mm towards the imported surface (the set value should make it possible to see the wear track). The imported surface was covered to see which part was left after cutting out (Fig. 4). Finally the volume of material loss was calculated using the option: measure from the menu.

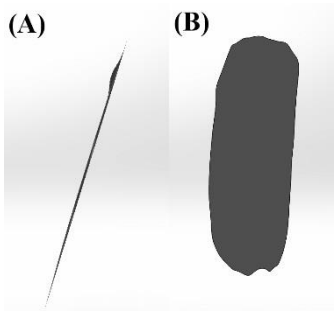

Fig. 4. View of (A) profile of wear trace in the material realized in SolidWorks, (B) top view

3.2. Evaluation of Wear with Confocal Microscopy

The fundamental principles of confocal imaging were patented by Marvin Minsky in 1961. In the confocal microscope the laser light reflects off a dichroic mirror. From there it hits the scanning mirrors and is focused by the lens at one point. The laser beam excites a dye-marked sample, which results in the emission of a longer light wave. Then the light returns along the same path through the scanning and dichroic mirrors hitting a diaphragm with a small hole in it. Finally, the focused beam reaches the detector where it is converted by the analog-to-digital converting device is and analyzed by computer (Cox, 2002). Confocal microscopy compared with conventional optical microscopy has a high resolution and contrast. The light that is excited in the regions lying outside the focus is eliminated by a system of pinholes and is not involved in creating the image. The result is an image containing no components from other than the focal plane. Confocal microscopy makes it possible to reconstruct 3D images and allows us to record images of the sample's thin layers at its different depths. Modern confocal microscopes enable us to analyze the topography of any surface with

high accuracy. Advanced optical devices are used for the observation of very thin layers of material (with a thickness of 1 μm even) in extremely high resolution and contrast. This is possible by using a laser as a light source. The achievable resolution is getting better generated images (resolution below 35 nm in XY), increasing the sensitivity of the light detection (detection of even single photons), and getting faster to create images of the samples tested (scanning speed of up to several tens of optical sections per second) (Korczyński, 2013) .

In the research microscope OLS 4000 Lext Olympus with 20-fold magnification was used (Fig. 5). The microscope produced topographical 3D images of the investigated surfaces. The samples were placed on the microscope stage, leveled and scanned by a laser beam. As a result, it was possible to obtain the data of the sample's selected area in the form of a spatial topography map of the wear track (Fig. 6). The LEXT software, compatible with the microscope, made it possible to fully analyze the acquired images.

Fig. 5. Confocal microscope Olympus OLS 4000 Lext

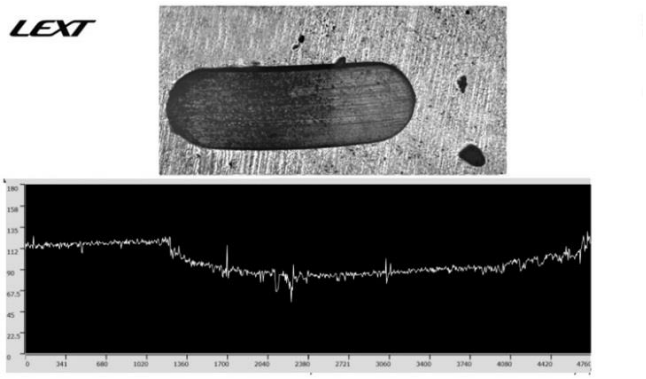

Fig. 6. Program LEXT report of the surface of the sample (visible trace of friction, wear values, longitudinal profile of trace friction)

4. RESULT

Figs. 8 and 9 present the values of volumetric wear of the dental materials subjected to friction in the friction couple composite – enamel. The two methods were used to compare the results obtained for each material. The measurement results are presented in the function of friction work. The data show slight differences in the method of evaluating the wear, as far as the matching of the linear regression model is concerned. There are a number of different diagnostic statistics methods used to assess the matching of the model to experimental data. The most commonly used is the determination coefficient denoted by R^2. Its value, approaching 1, indicates a better matching of the regression curve. The coefficient R^2 is a measure of the quality of matching of the model. It takes values from the range (0, 1). The closer the values come to 1, the better the matching of the model to the data is. The regression curves for the two methods are not identical and indicate higher wear rates obtained using the profilographometer.

As can be seen by comparing the curves, there is a much better matching of the regression curve for the measurements of wear rates for FFE material using confocal microscopy rather than the profilographometer. The determination coefficient assumes a value of 0.894, and is higher by 0.194 than that of the profilographometer. However, in the case of ES, these differences disappear so it is hard to say which of the two methods offers greater effectiveness (R^2 coefficient for profilographometer measurements is equal to 0.832 and for the confocal microscope 0.815).

In addition, the values of Pearson correlation coefficient r (Tab. 1) were calculated. The correlation analysis is used to test if there is a relation between two variables thus providing information on the strength and direction of the relation and whether the result is statistically significant. The correlation coefficient always takes values in the range (-1,1). The higher the absolute value of the coefficient, the higher the linear relation exists between the variables. In our case the sign of correlation coefficient is positive, which means that the relation between the variables is positive, i.e. if the wear increases, the value of the work done also increases. The values of the r coefficients confirmed the presence of a strong positive correlation between the specific wear energy and the value of wear for the ES and FFE materials using different measurement methods. According to A. Stanisz (2006), wear measurements for ES using confocal microscope and for ES using profilographometer and also for FFE using confocal microscope for $r \geq 0.9$ there is almost a complete correlation, while for FFE using profilographometer (for $r < 0.7, 0.9$) the correlation is very high.

Tab. 1. Values of coefficient of Pearson correlation r (p – significance level, N - importants)

Methods	r	p	Valid n
ES - confocal microscope	0.903	0.907	13
ES - profilographometer	0.9123	0.907	13
FFE - confocal microscope	0.9456	0.265	11
FFE - profilographometer	0.8367	0.265	11

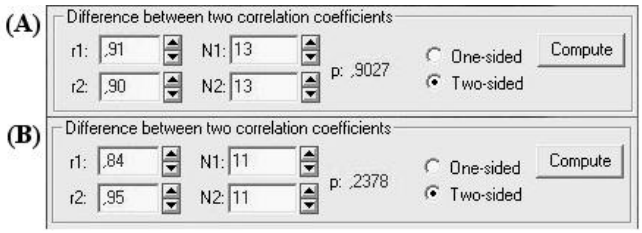

Fig. 7. Window with the results of the test for two correlation coefficients: A) ES ; B) FFE

Moreover, a test was performed to compare the statistical significance of differences between two Pearson correlation coefficients for each material (Fig. 7). Significance level p for ES was equal to 0.90 and for FFE $p = 0.24$, which confirms the previous

DOI 10.1515/ama-2015-0018

statistical interpretations that the correlation coefficients for the two methods used for both ES and FFE materials are the same. Thus, there are no significant differences in the wear values measured with the use of either confocal microscopy or the profilographometer.

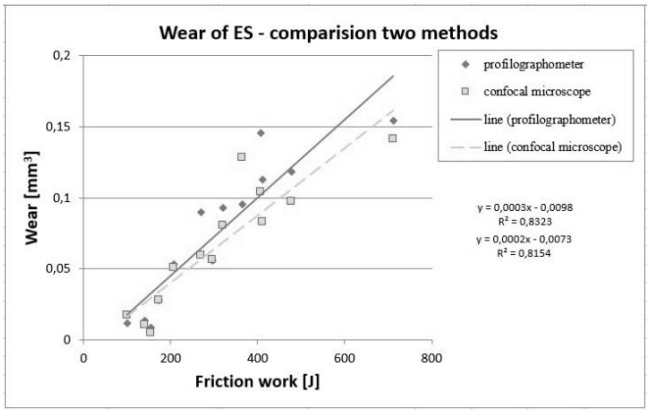

Fig. 8. Wear of ES materials in contact with the enamel in the function of friction work for two measuring methods

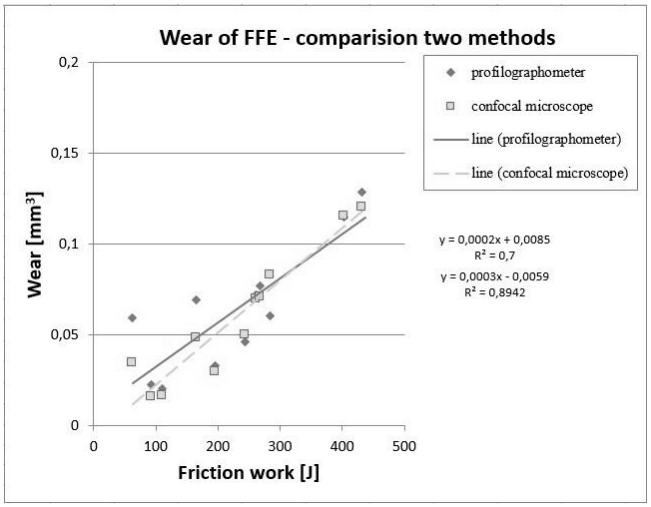

Fig. 9. Wear of FFE materials in contact with the enamel in the function of friction work for two measuring methods

In the research values of specific wear energy were calculated for each measurement (Sajewicz, 2007). Their averages are presented in Tab. 2. As the wear values of the investigated composites calculated with the prifilogrphometer were higher than those obtained with the use of the confocal microscope, specific wear energy, which is essential in the study of wear intensity of dental materials, assumed smaller values for the profilographometer measurements.

The paper also provides data concerning the standard deviation, which determines the degree of dispersion of results around the specific work energy. As can be seen in Table 2 the standard deviation for the FEE composite calculated with either method, i.e. confocal microscopy or the profilographometer is practically identical and amounts to 1409 and 1498 respectively. In the case of the ES material the standard deviation is twice the value for the microscopic measurements than profilographometer measurements, and amounts approx. to 8.000. This indicates that individual results obtained by confocal microscopy are farther from the average making them less typical. Thus, more accurate result are obtained for wear measurments in the case of the FFE material.

Tab 2. Average values of specific wear energy of tested composite materials and standard deviations

Materials	Specific wear energy (J/mm³); average values, standard deviations		
Estelite Sigma	Confocal microscope	7 491.365	8 015.584
	Profilographometer	6 006.887	4 331.477
FulFil Extra	Confocal microscope	4 264.377	1 498.094
	Profilographometer	3 890.394	1 408.803

For a more detailed comparative analysis of the two methods STATISTICA computer program was employed. Using the option of descriptive statistics, an average value of volume wear, standard deviation as well as standard error were calculated (Tab. 3). Higher measurement values using the profilographometer were observed, i.e.: for ES the average values are higher by 0.009mm³, and for FFE by 0.0043mm³. The standard deviation shows higher values for ES measurements. The standard error specifying the degree of accuracy with which the value of the arithmetic mean is determined, appears to be roughly the same for all measurements, yielding the highest values for ES materials. (confocal microscopy – 0.0123, profilographometer – 0.014). A smaller standard error for FFE proves better predictability of the measurement.

Tab. 3. Sheet results for descriptive statistics

Variable	Descriptive statistics			
	Valid n	Mean	Std. dev.	Std. error
ES confocal microscope	13	13	0.0663	0.0442
ES profilographometer	13	13	0.0754	0.0507
FFE confocal microscope	11	11	0.0597	0.0362
FFE profilographometer	11	11	0.0640	0.0346

In order to provide a more detailed comparative analysis of the two wear measurement methods a non-parametric Mann-Whitney U test available in STATISTICA was used (Tab. 5). The immediate reason for carrying out the comparison were some observations of the results. Namely it was observed the data scatter diagram from experiment for ES and FFE material (Fig. 8-9) strongly deviates from the normal distribution (i.e. the assumption of t-test is not fulfilled), which may indicate a lack of significant difference in arithmetic averages. So in this case, zero hypothesis assumes that the tested groups come from the same population, i.e. data distributions of the analyzed groups do not differ significantly.

Tab. 4 above provides in the header the adopted probability level of the test. The results are significant for $p < 0.05$. As shown in Tab. 4 p-value for ES material is high ($p = 0.343$), and, as a result, on this significance level, there is no good reason for rejecting the output (zero) hypothesis on equal impact of the two methods on the results. The results of the analysis ($p = 0.343$) lead to the conclusion that the research methods have a statistically insignificant effect on the value of the volumetric wear of the tested composites.

Tab. 4. Sheet results for Mann-Whitney U test for the data of experiments using material ES anf FFE

Variable	Mann-Whitney U test by variable method Marked tests are significant at $p < 0.05$ Methods: I – confocal microscope, II – profolographometer				
	Rank sum I	Rank sum II	p	Valid n I	Valid n II
ES	194	157	0,3428	13	13
FFE	134	119	0,6224	11	11

For the FFE composite the Mann-Whitney U test indicates the significance levelequal to 0.622 (Tab. 4), and also $p > 0.05$. So there is no justification to reject the hypothesis that the observed difference is accidental.

5. SUMMARY AND CONCLUSIONS

Evaluation of the wear of dental materials is crucial in view of their wear resistance in contact with tooth enamel. Susceptibility to wear determines the quality of dental materials and hence their cautious choice for permanent dental fillings determines the success of damaged tooth reconstruction. Because the wear values of tooth enamel exposed to friction are very small, of the order 10^{-2} (Sajewicz, 2007; Wojda et al., 2015), selection of an appropriate measurement method is extremely important for obtaining accurate and reliable results. In the present study two measurement methods assessing the loss of dental materials, i.e. confocal microscopy and profilographometer are analyzed. The statistical analysis of the results has clearly shown that the two methods do not show any significant differences as far as measurement accuracy is concerned. Hence both methods can be used interchangeably for the measurement of volumetric wear of dental materials. Guidelines for choosing of a specific method are certain advantages in the way of its application, namely availability of required equipment, graphics programs, the time needed for measurements, ease of taking measurements and use of software compatible with the measurement device.

In view of the research conducted by the author, it was the confocal microscopy method that proved to be easier and faster. The procedure requires placing the analyzed sample on the microscope stage and subjecting it to laser beam scanning. The data are automatically entered into the compatible software. At this stage, determining the value of wear requires uncomplicated knowledge of the program and it only a matter of minutes to obtain the needed data for further analysis. Unlike confocal microscopy, the profilographometer method requires a time-consuming measurements of investigated surface profiles involving manual-shift of the micrometer table and laborious further processing with the use of such computer tools as Catia, Rhinoceros or SolidWorks.

REFERENCES

1. **Cox G.** (2002), Biological confocal microscopy, *Materials Today*, 5, 34-41.
2. **Ferracane L. J.** (2006), Is the wear of dental composites still a clinical concern?: Is there still a need for in vitro wear simulating devices?, *Dental Materials*, Vol. 22 (8), 689-692.
3. **Korczyński J.** (2013), A new dimension of microscopy - laser scanning confocal microscope, Cosmos. *Problems in Biological Sciences*, Polish Society of Naturalists name of Copernicus Vol. 62 (2), 149-160 (in Polish).
4. **Lambrechts P., Goovaerts K., Bharadwaj D., De Munck J., Bergmans L., Peumans M., Van Meerbeek B.** (2006), Degradation of tooth structure and restorative materials: A review, *Wear*, Vol. 261 (9), 980-986.
5. **Louwerse C., Kjaeldgaard M., Huysmans M. C. D. N. J. M.** (2004), The reproducibility of ultrasonic enamel thickness measurements: an in vitro study, *Journal of Dentistry*, Vol. 32 (1), 83-89.
6. **Malacarne J., Carvalho R. M., De Goes M. F., Svizero N., Pashley D. H., Tay F. R., Yiu C. K., De Oliveira Carrilho M. R.** (2006), Water sorption/solubility of dental adhesive resins, *Dental Materials*, Vol. 22 (10), 973-980.
7. **Paepegaey A.-M., Barker M. L., Bartlett D. W., Mistry M., West N. X., Hellin N., Brown L. J., Bellamy P. G.** (2013), Measuring enamel erosion: A comparative study of contact profilometry, non-contact profilometry and confocal laser scanning microscopy, *Dental Materials*, Vol. 29 (12), 1265-1272.
8. **Park J., Choi D. S., Jang I., Yook H. T., Jost-Brinkmann P. G., Cha B. K.** (2014), A novel method for volumetric assessment of tooth wear using three-dimensional reverse-engineering technology: A preliminary report, *The Angle Orthodontist*, Vol. 84 (4), 687-692.
9. **Sajewicz E.** (2007), Tribological aspects of human dental organ, *Hearing Science 150,* Technical University of Bialystok, Bialystok (in Polish).
10. **Sajewicz E., Kulesza Z.** (2007), A new tribometer for friction and wear studies of dental materials and hard tooth tissues, *Tribol. Int,* 40, 885-895.
11. **Stanisz A.** (2006), Accessible statistics course using STATISTICA PL's at-examples medicine, Volume 1. Basic Statistics, Krakow (in Polish).
12. **Wojda S., Szoka B., Sajewicz E**., Tribological characteristics of enamel-dental material contacts investigated in vitro, *ABB*, Vol. 17 (1), 25.
13. **Wróblewska J.** (2014), Rating consumption volume of samples tested friction, Bialystok (in Polish).
14. http://www.microscopyu.com/articles/confocal/confocalintrobasics.html

DOI 10.1515/ama-2015-0019

ACCURACY ASSESSMENT FOR CAD MODELING OF FREEFORM SURFACE DESCRIBED BY EQUATION

Grzegorz GOLBA*

*Faculty of Mechanical Engineering, Department of Production Engineering, Bialystok University of Technology, ul. Wiejska 45C, 15-351 Białystok, Poland

g.golba@doktoranci.pb.edu.pl

received 14 July 2014, revised 21 July 2015, accepted 22 July 2015

Abstract: This paper presents the results of comparative analysis of modeling accuracy the freeform surface constructed by using a variety of algorithms for surface modeling. Also determined the accuracy of mapping the theoretical freeform surface described by mathematical equation. To model surface objects used: SolidWorks 2012, CATIA v5 and Geomagic Studio 12. During the design process of CAD models were used: profile curves, fitting parametric surface and polygonal mesh. To assess the accuracy of the CAD models used Geomagic Qualify 12. On the basis of analyse defined the scope of application of each modeling techniques depending on the nature of the constructed object.

Key words: B-Spline, CAD Model, Cloud of Points, Reverse Engineering, NURBS, Surface Reconstruction, Triangulation

1. INTRODUCTION

Due to the higher requirements of constructed elements, designers are forced to construct products containing freeform surfaces. CAD models are used at all stages of the production process – from design to evaluation of the manufacturing accuracy. To investigate the manufacturing accuracy of the element or preparing technical documentation is carried out by process called digitalization. The aim of this process is obtaining a cloud of points which representing the geometry of the object. Scanning devices are different in structure, principle of operation, accuracy and the nature of the generated results. The measurement data may be gained by contact method using the coordinate measuring machine (CMM) or non-contact method using optical scanners, etc. CMM generates clouds with a small number of regularly located points. Non-contact scanners have worse measurement accuracy compared with CMM, and the measurement results are represented by clouds with large numbers of irregularly located points. Taking into account the number of points in the cloud received by digitizing an object it is possible to apply different modeling techniques. In the case of modeling on a small number of regularly located points are used profile curves (Section 2.1). In the case of a cloud of points generated by non-contact scanning method cannot use this method for constructing the CAD model. For this reason, the process of preparing the CAD model is based on the generation of parametric surfaces on a cloud of points or a polygonal mesh (see section 2.2). Errors created in all these steps of manufacturing are included in the manufacturing accuracy. Required accuracy is directly related to the area of application of the element. The surfaces of optical components require the highest accuracy of manufacturing (10^{-3} – 10^{-6} mm). In the case of the most common applications, such as automotive, airplane, etc. the highest precision of manufacturing is smaller (10^{-1} – 10^{-3} mm) (Savio and De Chiffre, 2007).

Analyzing the available literature it can be concluded that, there are many publications which described the mathematical nature of curves (Hylewski, 2010; Piegl, 1989), and the parametrical surfaces used in freeform modeling (Hoffmann and Joan-Arinyo, 2002; Nyirenda et al., 2006; Paulos et al., 2008; Van den Berg et al., 2003). An important factor in the process of design models are a class of continuity used in design and styling of CAD surfaces (Putz, 2004). The process of modifying the curves and NURBS surfaces (Non-Uniform Rational B-Spline) by modifying the control points and weighting factors described in (Piegl and Tiller, 1997). More practical character has articles in which researchers describe the techniques used in the design of CAD models (Hoffmann and Joan-Arinyo, 2002). In position (Van den Berg et al., 2002) described the process of parameterization, and attempt to invent a system for the recognition of freeform shapes. Construction digital models of scanned objects used in the process of reverse engineering de-scribed in (Gawlik and Wójcik, 2003; Hylewski, 2009; Kruth and Kersterns, 1998; Wróbel, 2010). Evaluation the accuracy of the reconstruction process containing the step of freeform surface modeling is described in (Werner, 2012).

In the available literature, there are no accuracy analysis of CAD modeling based on a cloud of points. For this reason is justified to try to compare modeling techniques which are presented in this article. The article presents the process of modeling the surface of irregular shape described by a mathematical formula enabling subsequent analysis of the accuracy of modeling, dependent of the type of design techniques. Were compared the three most popular freeform surface modeling techniques in CAD programs used to design or reverse engineering. The results of the analysis described in this article allows to choose the appropriate modeling techniques matched to a specific category of surface, taking into account the nature of its geometry, application and required accuracy of manufacturing. will be possible to initial estimate of modeling deviations occurring during the CAD

model design resulting from the application of the techniques described in this article

2. THEORETICAL BASIS

Choosing the proper techniques of freeform surface modeling must take into account application, and hence the required manufacturing accuracy of the element (Savio and De Chiffre, 2007). Modeling procedure can result in errors, which values exceed the requirements established during manufacturing. In the case of modeling which is based in a cloud of points approach to the process of generate the CAD model may be different. It is determined by the number, and nature of the location of points in the cloud. In most engineering programs during the construction of CAD model on a cloud of points with a small number of regularly located points are used profile curves. For this purpose, the curves B-spline (Basis spline) forming profiles that are the backbone for future extrude of the parametric surface (Section 2.1). Profile curves interpolate points called nodes (points included in the curve) (Piegl and Tiller, 1997). B-spline Curves in case of modeling based on theoretical cloud of points are interpolate curves expressed using spline functions, i.e. functions defined by polynomials on a coherent sum of sub-intervals. The process of interpolation for parametric curves consists in determining the interpolation function within the range defined by the theoretical cloud of points. Searched function returns certain values at points which are nodes of curves (theoretical points in cloud). In other words, interpolation function passes through all the nodes, and the error of interpolation nodes must be unconditionally equal to 0. Interpolation error can be reduced by increasing the number of nodes which are part of the curve. In order to improve approximations of interpolation function are used additional conditions of smoothness at the connection point of polynomials for ensuring the continuity of the second derivative of the spline function. In case of generate freeform surface based on cloud with a lot of irregularly located points can be used triangulation and parametric surfaces called NURBS (see section 2.2, 2.3). In the case of modeling using a triangle mesh is used approximation process of triangle mesh by the parametric surface. The task of approximation is to find the parametric surfaces that reflect as accurately as possible the nature of the modelled geometry. Looking for solutions close as possible to ideal during modeling freeform surface is used the method of least squares which minimizing the sum of squared errors occurring during the generation of the surface. In other words, this method fits surface to the data in the form of theoretical points or profile curves in such a way that the overall estimation error (for all points or curves) was as small as possible.

In the article the basis for modeling was a cloud of theoretical points generated by mathematical equation. In the case of the CAD model constructed using the profile curves, these points are as nodes. Then on the skeleton constructed by profile curves extruded a parametric surface.

2.1. B-spline Curves

This type of curves used in CAD modeling determines a string of control points enabling local control of the shape. The curve is determined by the interval parameter divided into sub-intervals called nodes. In the case of equidistant nodes curve is called uniform. The division of the range of the curve in a non-uniform way creates NURBS curve. The main advantage of B-spline curves is the ability to modify any part of the curve without affecting the shape of the remainder (Piegl, 1989). Thanks to these properties of B-spline curves it is possible to modeling profile curves for extrude the parametric surface. To designate any point on the curve B-spline is used the following equation (Piegl and Tiller, 1997):

$$p(\mathrm{t}) = \sum_{\mathrm{i}=0}^{\mathrm{m}-\mathrm{n}-1} p_i N_i^n(t) \text{ for } t \in [\mu_n, \mu_{m-n}] \quad (1)$$

where: n – degree of the curve, $m + 1$ – number of nodes, p_i – control points, $N_i^n(t)$ – normalized B-spline function of n degree, t – parameter of interval, u_n, u_{m-n}– nodes of the curve.

2.2. Triangulation

Non-contact scanning techniques used in reverse engineering generate clouds with a huge number of irregularly located points. This creates a serious problem when editing a cloud of points consisting thousands of measurement points. The problem is caused by increase the main memory of the computer which needs during the process of constructing a CAD model. Many of specialist software which enables processing large amounts of data were created to prevent this problem. The process of constructing a CAD model has become simple, and completely automated through the use of triangulation. This process involves a connection of points in clouds by using the curves so that each point will be a vertex of the triangle. To make this possible a cloud of points is subjected to pre-treat to remove unwanted noise and distortion. In a subsequent step the number of points in areas with a small shape variation is reduces. Then, in order to obtain a uniform triangle mesh model is subjected to appropriate transformations, such as mesh simplification, editing and deleting an overlap of meshes.

The final step of the construction of a CAD model is to generate parametric surface on a triangular mesh. This process uses a global algorithm of approximation to fit the geometry of the parametric surface to the triangle mesh (Piegl and Tiller, 1997).

2.3. NURBS Surfaces

The NURBS surfaces are the most flexible, taking into account the design of CAD objects, because faithfully reflects the nature of freeform shapes. It is possible to extrude the surface on profile curves (approach applied to cloud with a small number of points). The second method generates the surface on a cloud of points or a triangular mesh (this method is used for clouds with large numbers of irregularly located points). Considering NURBS surfaces can be seen, that each modification of number, and position of control points in the control grid causes a local change in the shape of the generated surface (Piegl and Tiller, 1997).

The shape of B-spline surface is described by equation (2):

$$B(u, v) = \sum_{i=0}^{n1} \sum_{j=0}^{m} d_{i,j} N_{i,s}(u) N_{j,r}(v) \quad (2)$$

where: $d_{i,j}$ – vertices of control grid, $N_{i,s}(u)$, $N_{j,r}(v)$ – basis functions of B-spline curve.

In the case of the representation of the real object using parametric surfaces, points defining the geometry of the object should be given in homogeneous coordinate system. NURBS

DOI 10.1515/ama-2015-0019

surface is generating by using internal mathematical tools to approximate the input data in the form of a cloud of points or triangular mesh. Approximation in this case approximates the cloud of points or triangular mesh by parametric surface.

3. DESIGN OF CAD MODELS

In studies of the accuracy of modeling were constructed three CAD models by using different techniques of modeling the freeform surface. The basis of the models was a cloud of theoretical points which was determined by equation (3), describing a mathematical model of the freeform surface. Generated 2 600 points on the regular grid X × Y of size 1 × 1 mm in range of 50 × 50 mm (Fig. 2). Constructed CAD models compared with cloud of theoretical points described by mathematical equation (3).

$$z = 5 \cdot \sin(\frac{x}{12}) + \cos(\frac{y}{12}) \quad (3)$$

where: $x - x$ – coordinate of point $x \in (0.50)$, $y - y$ – coordinate of point $y \in (0.50)$, $z - z$ – coordinate of point.

Further in this chapter described three modeling techniques used while constructing CAD models of the surface at the theoretical cloud of points. The first model, which used a profile curves called MWPC. Other models were designed using: fitted parametrical surface (MWPS) and the triangular mesh (MWTM).

3.1. Model with profile curves

MWPC was constructed in SolidWorks using the B-spline curves run through a series of points in cloud. The process of generating curves was made accordance with the following scheme: all the points in a "0" row of cloud was combined with a single curve. Another row of points, that is, "1" row was left in the form of points, and the "2" row was also connected by means of the curve. This approach makes it possible to verify the accuracy of the modeling not only at the points belonging to the curve, but also at intermediate points. This allows determining the accuracy of approximation the changes of geometry in cloud of points by the parametric surface. In this manner generated 25 profile curves, every other row in the cloud of theoretical points. The nodes in curve were points belonging to the theoretical cloud of points. Therefore modeling errors, at all points belonging to the curves compared to the theoretical cloud of points should be 0 (Piegl, 1989). In a further step of modeling, profile curves were used in the process of create the parametric surface by extrude the profiles. MWPS was constructed in CATIA v5. On the theoretical cloud of points created parametric surface matched to the characteristics of the cloud. For this purpose was used the power fit option which contains the approximation by method of least squares to fit the shape of the surface to the cloud of points. MWTM was built in three stages. In the first stage, on the cloud of theoretical points was carried out the triangulation process, the result of which was triangular mesh (see section 2.2). Points in cloud were combined in segments in such a manner that each point of cloud has become a vertex of the triangle. In a second step was focused on modify, and remove the overlap of meshes in order to obtain a single model. In the last stage extruded the NURBS parametrical surface. The next stage of preparation for the analysis was to determine the reference component and test component.

4. ACCURACY ANALYSIS OF MODELING

Verification of the accuracy of the developed CAD models designed by using different modeling techniques was performed by using Geomagic Qualify 12. Using the procedure deviation determined the modeling errors between the reference object and test object. Before analysing, it was necessary to import the cloud of points and CAD models to the program. As a reference model adopted cloud of points and test object (subjected analysis) CAD models of the freeform surface.

4.1. Analysis of the Accuracy of MWPC

As first was conducted an analysis of the accuracy MWPC (Fig. 1).

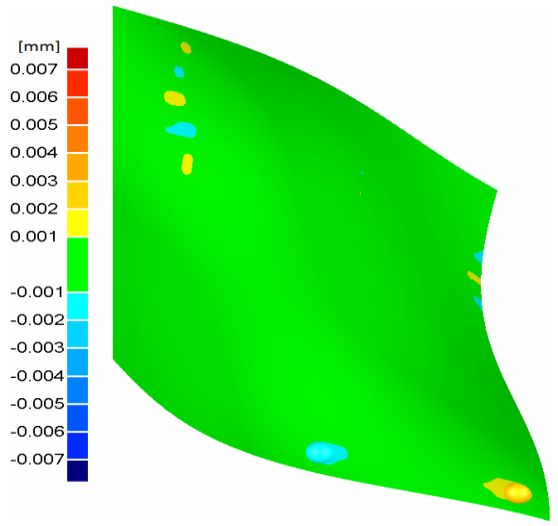

Fig. 1. Error map of MWPC

Analysing the map can be concluded that modeling errors are small. 99% of the analysed model points coincide with the theoretical cloud of points. This is because was used of interpolation curves which connecting the consecutive points during the process of constructing a CAD model (see sect. 2.1). The greatest value to the modeling error (+0.001 mm) appeared in the area of greatest slope surface.

Considering the percentage distribution of modeling errors of MWPC, it is clear that the percentage participation of errors with the same values , but with opposite signs is very close to each other (Fig. 2).

MWPC modeling technique except high-accuracy mapping contains one major drawback, which is the time-consuming process of constructing the profile curves passing through all the points in the cloud. This fact practically disqualifies this method of constructing in modeling of objects with large sizes for example reconstructions castles. Another disadvantage of this modeling technique is the inability to use of the data in the form of a cloud of points obtained by contactless scanning, where generated a large number of irregularly spaced points. In this case, during the construction of the profile curves program which was used to constructed CAD model would generate a huge demand in the operating memory of the computer.

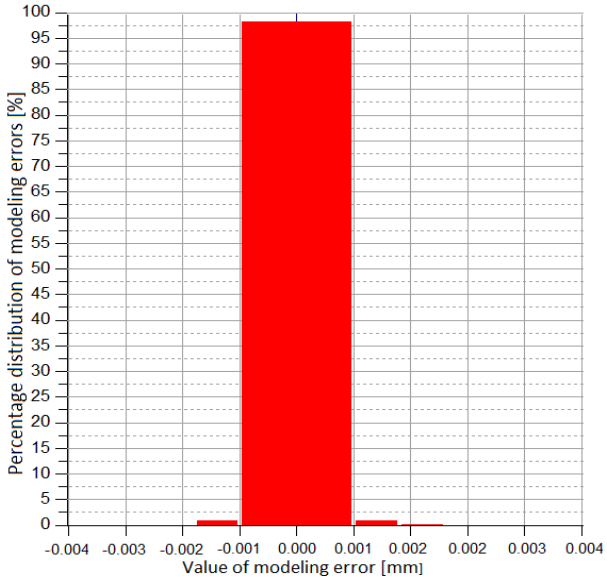

Fig. 2. Percentage distribution of errors MWPC

4.2. Analysis of the Accuracy of MWPS

Another model under review in terms of the accuracy of modeling was a MWPS (Fig. 3).

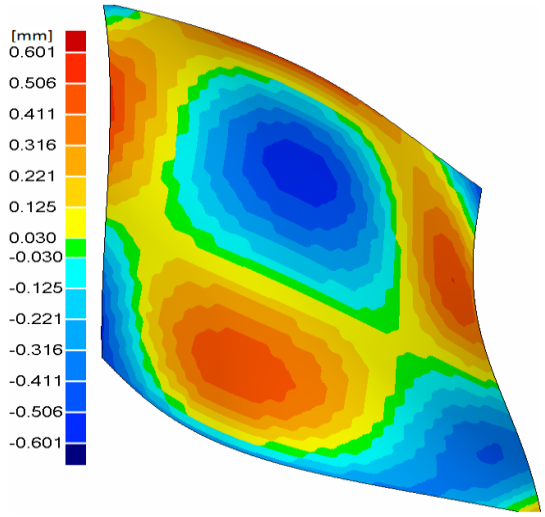

Fig. 3. Error map of MWPS

Large values of errors in MWPS, reaching of value ± 0.601 mm, occurred in the areas of the largest peaks and depressions, while the smallest errors occurred in the areas of change the curvature. This distribution modeling errors results from the fact that parametric surface which approximate the shape of theoretical cloud of points was used to generate CAD model. It introduces significant errors in the process of construction of a CAD object. Taking into account the distribution of errors MWPS can be concluded, that this technique is the best to modeling objects characterized by low volatility of shapes. Percentage distribution of errors MWPS clearly shows the considerable variation of the values and the percentage of occurrences (Fig. 4). Most errors (13.5%) which were occurred during the construction of a CAD model reached a value of +0.120 mm, which indicate a low accuracy MWDP. Taking into account graph shown in figure 10 it can be concluded that this modeling technique is propose to be used in the design of large-scale CAD models of objects, where the modeling errors of 0.3 mm does not have a major impact on the final result of the project. Proper application of this modeling technique would be reconstruction of sculptures and castles, where inaccuracy of mapping object reaching of tenths part of a millimetre is the most acceptable.

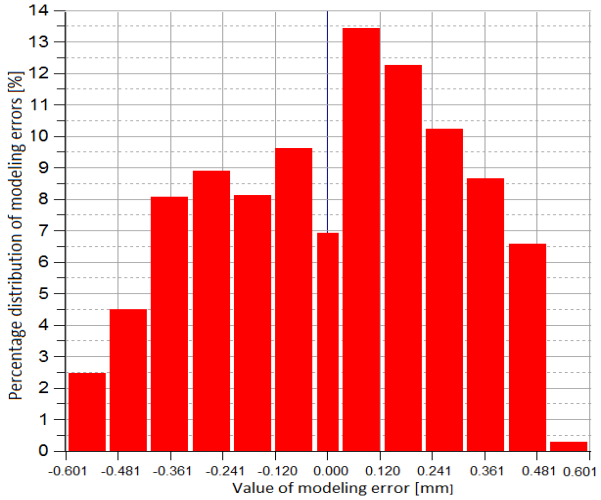

Fig. 4. Percentage distribution of errors MWPS

4.3. Analysis of the accuracy MWTM

Third analysis of accuracy was subjected MWTM (Fig. 5). Mesh of triangles made it impossible an accurate reconstruction of geometry the clouds of points in areas with significant elevations and depressions. Triangles are flat, so that an accurate representation of complex geometry, characterized by the freeform shape was not possible.

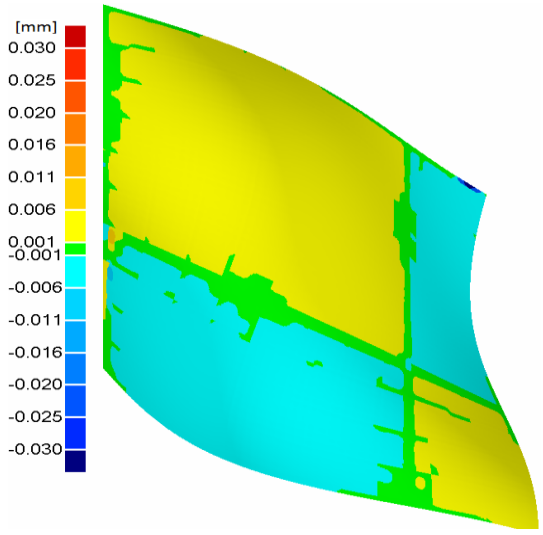

Fig. 5. Error map of MWTM

Errors which made during the process of generating a CAD model are result of using the parametric surfaces. NURBS surface is fitted to the surface of a triangle mesh, which as previously mentioned does not reflect all the changes shape. Percentage distribution of errors MWTM was shown in figure 6. The largest

DOI 10.1515/ama-2015-0019

percentage of instances (27%) was recorded for the error value of +0.006 mm. The highest values of errors reaching +0.030 mm occurred in 0.2% of the freeform surface. The accuracy of the mapping model is not as high as in the case of the model made MWPC technique. This results from the fact that the CAD model is the result of approximation process (generation of parametric surface) instead of interpolating (profile curves which goes through a points in cloud of points) as in the case MWPC model. Due to the possibility of easy processing of large amounts of data in the form of clouds with a large number of points this method is recommended for processing of data generated by noncontact digitization.

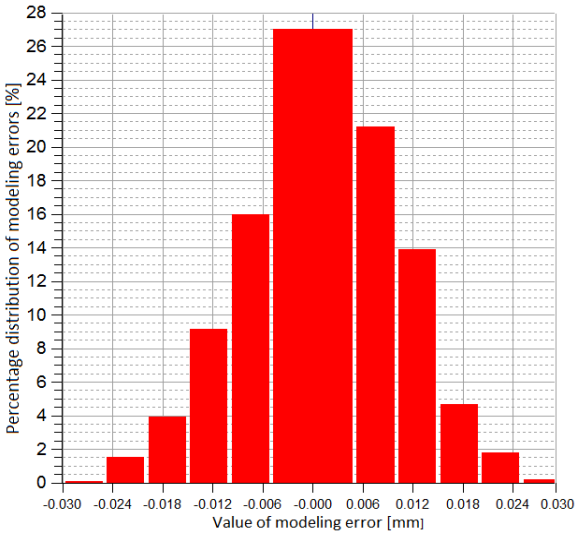

Fig. 6. Percentage distribution of errors of MWTM

5. CONCLUSIONS

Analysing the maximum modeling errors arising from the technique used to construct the CAD model can be seen a clear advantage in favour of the model MWPC. The maximum error values reach +0.007 mm, and are almost one hundred times smaller than those resulting from the application of modeling techniques MWPS (+0.601 mm). MWPC technique is suit for modeling the freeform surface, and the flat surface because of the high accuracy of mapping the shape of the cloud of points. In the case of design objects, in which the accuracy of the mapping is very important, MWPC modeling technique is most recommended. The only serious limitation in terms of use it is the difficulty, which appears when modeling is based on a cloud with a lot of points. This is caused by considerable demand of the CAD program in operational memory. The maximum modeling error (+0.030 mm) resulting from the application of MWTM modeling techniques is twenty times smaller than the modeling error of in MWPS. Taking this fact into account MWTM technique should be used to modeling objects with large dimensions, or in the case of constructing a CAD model based on a cloud with a very large number of irregularly spaced points. The highest accuracy of mapping the shape of the object by using this technique of modeling obtained in case of surface with a small variation of the shape. These results from the fact that the triangles are planar figures, which less illustrate the local variation of geometry. Taking into account the use of freeform surfaces, and hence the required precision of manufacturing (Savio and De Chiffre, 2007) can be analysed to evaluate the possible application of modeling techniques. Errors arising at the stage of digitalization, modeling and production are a part of manufacturing error, which should be taken into account in the selection of appropriate modeling techniques. MWPC technique can be successfully used for modeling small turbine blades, and automotive parts (acceptable manufacturing error 0.020 mm - 0.001 mm). MWTM is suitable for construction of objects such as aircraft components (maximum manufacturing error 0.500 mm - 0.020 mm). Castles elements, aircraft wings, large-scale sculptures and objects without large changes in the shape it is best to design using the technique MWPS.

Worth considering during the design elements with significant size containing complex surfaces is to use a combination of two modeling techniques. The MWPC technique will enable high accuracy in constructing the model with complex shape. MWTM technique could be applied in areas where local changes in the geometry of the shape are small.

REFERENCES

1. **Gawlik J., Wójcik A**. (2003), Modeling and assessing the accuracy of the freeform surfaces in the wmp-cad-cam system (in Polish), *Prace Naukowe Instytutu Technologii Maszyn i Automatyzacji Politechniki Wrocławskiej*, Vol. 84, 173-182.
2. **Hoffmann CM., Joan-Arinyo R**. (2002), Parametric modeling, In: Farin G, Hoschek J,Kim MS (editors), *Handbook of CAGD*, *Elsevier*, 519-541.
3. **Hylewski D**. (2009), Representation of curves in CAD systems – Bezier curves (in Polish), *Prace Naukowe Katedry Budowy Maszyn Politechniki Śląskiej,* Vol. 1, 273-282.
4. **Hylewski D**. (2012), Attempt to verify the method for selecting the parameters of digitizing the freeform surface for the purpose of reverse engineering in Catia v5 system (in Polish), *Inżynieria Maszyn*, Vol.3, 128-146.
5. **Kruth JP., Kersterns A**. (1998), Reverse engineering modeling of free-form surface from point clouds subject to boundary condition, *Journal of Materials Processing Technology*, Vol. 76, 120-127.
6. **Nyirenda PJ., Mulbagal M., Bronsvoort WF.** (2006), Definition of freeform surface feature classes, *Computer-Aided Design and Applications*, Vol. 3(5), 665-674.
7. **Paulos J., Nyirenda., Willem F. Bronsvoort.** (2008), Numeric and curve parameters for freeform surface feature models, *Computer-Aided Design*, Vol. 40 (8), 839-851.
8. **Piegl L.** (1989), Modifying of rational B-spline. Part 1: Curves, *Computer Aided Design*, Vol. 21, 509-518.
9. **Piegl L., Tiller W.** (1997), *The NURBS book*, 2nd ed., Springer, New York.
10. **Putz B.** (2004), From G0 to G3 – class of smoothness in the design and styling surface (in Polish)*, Mechanik*, Vol. 11, 759-764.
11. **Savio E., De Chiffre L.** (2007), Metrology of freeform shaped parts, *CIRP Annals - Manufacturing Technology*, Vol. 56 (2), 810-835.
12. **Van den Berg E., Bronsvoort W. F., Vergeest J. S. M.** (2002), Freeform feature modeling: concepts and prospecs, *Computers in Industry*, Vol. 49 (2), 217-233.
13. **Van den Berg E., Van der Meiden H. A., Bronsvoort W. F.** (2003), Specification of freeform features. In: Elber G, Shapiro V (editors*), Proceedings of the eighth ACM symposium on solid modeling and applications*, New York: ACM Press, 56-64.
14. **Werner A.** (2012), Assessment of accuracy in the process of reverse engineering the spatial object (in Polish), *Pomiary, Automatyka, Robotyka*, Vol. 5, 86-90.
15. **Wróbel I**. (2010), Reverse engineering as a method of creating digital models of objects with complex shapes (in Polish), *Mechanik*, Vol. 3, 212–214.

ANTIPLANE DEFORMATION OF A BIMATERIAL CONTAINING AN INTERFACIAL CRACK WITH THE ACCOUNT OF FRICTION I. SINGLE LOADING

Heorhiy SULYM[*], Lyubov PISKOZUB[**], Yosyf PISKOZUB[**], Iaroslav PASTERNAK[***]

[*]Faculty of Mechanical Engineering, Bialystok University of Technology, 45C, Wiejska Str., 15-351 Bialystok, Poland
[**]Ukrainian Academy of Printing, Pidgolosko Str. 19, 79020 L'viv, Ukraine
[***]Lutsk National Technical University, Lvivska Str. 75, 43018 Lutsk, Ukraine

h.sulym@pb.edu.pl, piskozub@pancha.lviv.ua, piskozub@uad.lviv.ua, pasternak@ukrpost.ua

received 3 March 2015, revised 22 July 2015, accepted 23 July 2015

Abstract: The paper presents the exact analytic solution to the antiplane problem for a non-homogeneous bimaterial medium containing closed interfacial cracks, which faces can move relatively to each other with dry friction. The medium is subjected to the action of normal and arbitrary single loading in a longitudinal direction. Based on the discontinuity function method the problem is reduced to the solution of the system of singular integral-differential equations for stress and displacement discontinuities at the possible slippage zones. Influence of loading parameters and the effects of friction on the sizes of these zones is analyzed. The stress intensity factors, stress and displacement discontinuities, energy dissipation are determined for several characteristic types of external loading.

Keywords: Friction, Interfacial Crack, Energy Dissipation, Stress Intensity Factor, Antiplane Deformation, Longitudinal Shear, Bimaterial, Discontinuity Functions

1. INTRODUCTION

The study of the contact phenomena with the account of friction effect is one of the most actual problems in mechanical engineering (Goryacheva, 2001; Panasiuk et al., 1976; Sulym and Piskozub, 2004; Johnson, 1985; Hills et al.,1993; Herrmann and Loboda, 1999; Ulitko and Ostryk, 2006) etc. To a greater or lesser extent the contact phenomena both at macroscopic and microscopic levels are always accompanied with friction.

Fracture mechanics studies mainly problems for cracks with traction-free faces. Rarely the problems for cracks with uniformly distributed tractions (internal pressure) or concentrated forces applied at their faces are considered. The solution of the problems of first kind are important in the analysis of stress strain state near the oil or gas layers (Kit et al., 2003; Evtushenko and Sulym, 1981), mechanical influence of hydrogen, which due to high permeability and mobility migrates into the material cavities, thus, creating there high pressure and debond adhesive joints in the material, increasing defects size. The solution of the second kind has not only the applied value, but also serve as Green's functions, thus allows deriving the solutions of the problems with loadings arbitrarily applied at crack faces.

The problem of crack faces contact, which account for contact interaction, is less studied. Main achievements in this direction belong to the theory of interface cracks in a bimaterial within the framework of 2D elasticity, which uses different models of local crack face contact for elimination of physically incorrect oscillating behavior (Comninou, 1977, 1980; Schmueser, 1980; Aravas and Sharma, 1991; Herrmann and Loboda, 1999; Kharun and Loboda, 2001, 2003; Sulym and Piskozub, 2004).

Kundrat (2003) developed the two-phase model, when between the plastic bands (first phase of prefracture zone) at the continuation of the axis of a thin inclusion there develops a short zone of crumby material (the second phase), where the shear stress of adhesive interaction linearly decrease from zero at the tip to the value at the beginning of the plastic band, thus removing the singularity of the solution.

Among other directions of the account of friction in crack face interaction one can refer to the publication of Cherepanov (1966). The referred paper formulates two types of boundary conditions for overlapping faces of the mathematical cut (crack), at which discontinuities of normal stress, displacement and tangent traction are defined, and mechanical interaction of opposite faces of the cut can be arbitrary.

Sekine (1982) studied mechanics of deformation of inclusion-stringer in the infinite isotropic medium, which is stretched along the axis of inclusion. It was assumed, that the central zone of a perfect contact of materials was accompanied at both sides with two-phase zones of imperfect contact, moreover, the first one addressed smooth contact (without friction), and that at the tip of the inclusion (the second one) addressed friction (here normal stress was compressive, and the material of a matrix in the contact zone of inclusion did not depart from it in the normal direction).

The wide range of problems on the influence of friction on contact stress between half-planes with superficial smooth surface notches were studied by Martynyak et al. (2000, 2005, 2007).

The growth of delaminating crack (actually mutual slippage of the materials) at the interface of rigid fibrous inclusion was studied by Brussat and Westmann (1974) with the account of friction between components. In this relation it is necessary to pay attention to the works by Antipov (1995), Arkhipenko and Kryvyy (2008), Ulitko and Ostryk (2002, 2006), Weertman et al. (1983).

The problem of crack faces contact accounting for friction

is less studied in the case of antiplane shear (Sulym, 2007; Pasternak et al., 2010).

This paper presents the technique for studying the influence of friction during the out-of-plane deformation (antiplane problem) of a solid with a closed crack on the formation of slippage zones and energy dissipation in the case of quasi-static (slow) application of single monotonously increasing loading. In the general case of= loading type and position with respect to closed cracks one can assume that the loading at the beginning is low enough to cause slippage. Then it is enough to cause slippage, but the slippage zones do not reach the size of the cracks, and thus the stresses are finite at their ends. And finally for enough big loading the cracks' sizes bound the growth of slippage zones, and thus, at one or both of its tips stress singularity arises.

The discontinuity function method (Sulym et al., 2007, 2008, 2010) and the singular integral-differential equation approach are the base of the proposed technique. It is assumed that the loading applied to the piecewise-homogeneous medium with interface strip-like (tunnel) crack can be divided into two types: the first one satisfies the plane strain conditions, and the second one performs the out-of-plane deformation of a medium. Thus one can formulate two problems, one of which (the antiplane one) is further called the primary problem, and the second (the plane one) is auxiliary as it allows to determine the distribution of compressive traction at the contact surfaces of half-spaces and layers. Thus, due to the independent separation of in-plane and out-of-plane problems in the linear elasticity of isotropic materials, the solution of the primary problem does not influence the solution of auxiliary one.

2. PROBLEM STATEMENT

Consider the infinite isotropic matrix consisting of two half-spaces with the elastic constants $E_k,\ \nu_k,\ G_k \quad (k = 1,2)$, which interface L contains N coaxial strip-like cracks. In this extent, it is possible to consider contact defects with different rheological properties. Everything depends on the models used for simulating their behavior (Sulym et al. 2004, 2007, 2008, 2010).

The fixed reference Cartesian coordinate system $Oxyz$ is considered, which xOz plane coincides with the material interface, and Oz axis is directed along the longitudinal axes of cracks.

Consider the stress strain state of the solid's cross-section with the xOy plane, which is perpendicular to the shear direction z. The cross-sections of the bimaterial perpendicular to the interface form two half-planes $S_k \ (k = 1,2)$, and the material interface correspond to the abscissa $L{\sim}x$. The latter contains median lines of cracks' sections, which mold a line $L' = \bigcup_{n=1}^{N} L'_n = \bigcup_{n=1}^{N} [b_n^-;\ b_n^+]$ (Fig. 1). The application of similar traditional notation for an axis z and a complex variable $z = x + iy$ should not cause misunderstanding in the solution of the problem.

Contact between the bimaterial medium components along a line $L'' = L \backslash L'$ is supposed to be mechanically perfect, and the contact along defects' (cracks') faces L' is assumed to be performed according to the laws of tangential mechanic contact, at which bodies contact mechanically perfect until the moment, when relative sliding of crack surfaces may start in some areas $\gamma_n \subset L'_n$ at the material interface (Johnson, 1985; Goryacheva, 2001; Sulym and Piskozub, 2004). Outside the lines γ_n the value of tangential traction at the places of the slippage absence does not exceed the level of maximal admissible traction, and the mutual displacement of crack faces is not observed (the displacement discontinuity $[w]_n$ is zero). The sign (an action direction) of tangent traction is chosen depending on a sign of a difference of displacement at both sides of a cut γ_n at the considered point. The following notations are used hereinafter: $[\phi] = \phi(x,-0) - \phi(x,+0)$, $\langle\phi\rangle = \phi(x,-0) + \phi(x,+0)$.

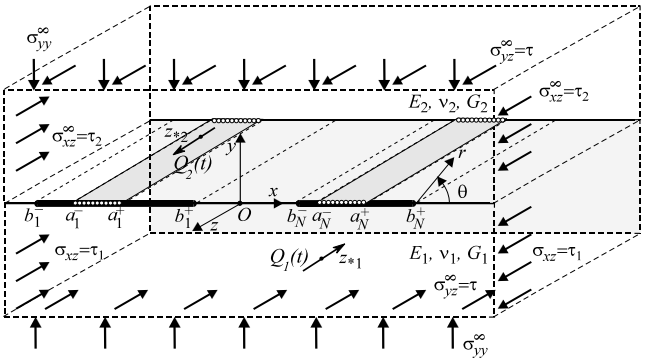

Fig. 1. The loading and geometric scheme of the problem

The medium is loaded with the mechanical load (stress at the infinity, the concentrated forces, etc.) such that their action causes the quasi-static stress strain state in a bimaterial solid. Simultaneously with the main loading, which defines the out-of-plane deformation, the medium is subjected to the additional in-plane (xOy) compressing loading, which causes the plane strain deformation. Its influence on the solution of the primary problem of longitudinal shear occurs only in the case when at the contact lines $\gamma_n \subset L'_n$ of crack faces contact the perfect mechanical contact is violated, where the normal stress σ_{yyk} is negative and the pressed surfaces of contacting materials move relatively to each other in the z direction.

The contact conditions with the possibility of slippage with friction at the closed crack provide that at the achievement by tangent traction σ_{yz} at the lines γ_n of a certain critical value $\tau_{yz}^{\max}$ the slippage occurs, and the tangent traction cannot exceed this threshold. Thus, within the classical Amontons' law of friction (Goryacheva, 2001; Johnson, 1985; Hills et al., 1993; Comninou, 1977, 1980), consider a variant of a contact problem according to which the tangent traction (friction traction) is constant along the lines γ_n:

$$\sigma_{yzn}^{\pm} = -\operatorname{sgn}([w]_n)\tau_{yz}^{\max}, \quad \tau_{yz}^{\max} = -\alpha\sigma_{yy} \ \left(\sigma_{yy} < 0, \ \ |w^- - w^+| \neq 0\right)' \tag{1}$$

where α is a coefficient of dry friction. Outside the lines γ_n the tangent traction at the crack points without slippage does not exceed the possible admissible level

$$\left|\sigma_{yzn}\right| \leq \tau_{yz}^{\max} \quad \left(\sigma_{yy} < 0, \ \ [w]_n = 0\right) \tag{2}$$

and the mutual crack face displacement (displacement discontinuity) is absent. The sign (an action direction) of tangent traction is chosen depending on a sign of the difference of displacements $[w]_n$ at a considered point of γ_n. At those points of L'_n, where $\sigma_{yyk} \geq 0$, the classical conditions of a traction-free crack are formulated:

$$\sigma_{yzk} = 0. \tag{3}$$

Application of the law of friction in the form of (1) allows to simplify the boundary conditions for the primary problem, however, a choice of more difficult models of friction incorporating Eqs (1), (2) (Goryacheva, 2001; Sulym and Piskozub, 2004; Pasternak et al., 2010; Popov, 1966; Johnson, 1985; Hills et al., 1993), which account for wear and thermal emissions (Bogdanovich and Tkachuk, 2009; Pyrjev et al., 2012; Datsyshyn and Kadyra, 2006; Goryacheva et al., 2001), will not essentially complicate the solution process.

Following the approach of Refs (Panasyuk et al., 1976; Piskozub and Sulim, 2008; Sulym, 2007), consider that the influence of defects of contact is possible to model with the stress and displacement discontinuities at L'_n:

$$[\Xi]_{L'_n} \equiv \Xi^- - \Xi^+ = \mathbf{f}^n, \tag{4}$$

where $\Xi(z,t) = \left\{\sigma_{yy}, \sigma_{xy}, \sigma_{yz}, \frac{\partial u}{\partial x}, \frac{\partial v}{\partial x}, \frac{\partial w}{\partial x}\right\}(z,t)$ is a state vector; $\mathbf{f}^n(x,t) = \{f_1^n, f_2^n, f_3^n, f_4^n, f_5^n, f_6^n\}(x,t)$ is a discontinuity vector; t is time as a formal monotonously increasing parameter related with the convertible force.

The solution of the auxiliary problem for the case of arbitrary mechanical loading and a perfect contact is presented by Panasyuk et al. (1976), Pasternak et al. (2010), Piskozub and Sulim (2008), Sulym (2007). To illustration the considered approach, consider its elementary applications, assuming that half-spaces are compressed by a uniform pressure

$$\sigma_{yyk} = -P \ \ (k = 1,2; \ \ x \in L). \tag{5}$$

For the primary problem with the account of Hook's law, Eq (4) writes as:

$$\begin{aligned}
&\left[\sigma_{yz}\right]_{L'_n} \equiv \sigma_{yz}^- - \sigma_{yz}^+ = f_3^n(x,t),\\
&\left[\frac{\partial w}{\partial x}\right]_{L'_n} \equiv \frac{\partial w^-}{\partial x} - \frac{\partial w^+}{\partial x} = \left[\frac{\sigma_{xz}}{G}\right]_{L'_n} \equiv\\
&\equiv \frac{\sigma_{xz}^-}{G_1} - \frac{\sigma_{xz}^+}{G_2} = f_6^n(x,t), \ x \in L'_n;\\
&f_3^n(x,t) = f_6^n(x,t) = 0, \text{If} x \notin \gamma_n.
\end{aligned} \tag{6}$$

Assuming that the magnitude and a direction of action of the mechanical loads, which perform longitudinal shear, change quasistatically (so slowly that there is no necessity to consider inertial terms) and change under the certain law, which can be arbitrary. Thus, external loading of the primary problem is defined by the stress $\sigma_{yz}^{\infty} = \tau(t), \sigma_{xz}^{\infty} = \tau_k(t)$ uniformly distributed at the infinity, the concentrated forces of intensity $Q_k(t)$ and screw dislocations with Burgers vectors $b_k(t)$ applied at the points $z_{*k} \in S_k (k = 1,2)$. According to Eq (20.5) of (Sulym, 2007) stresses at the infinity at arbitrary time should satisfy the condition

$$\tau_2(t)G_1 = \tau_1(t)G_2, \tag{7}$$

which provides the straightness of the material interface at the infinity.

After the antiplane problem is solved accounting for friction and for each contact lines γ_n the displacement discontinuity is determined, it is possible to calculate the work of friction forces. This work, and hence, and the energy dissipation at γ_n for a single step of change in external loading from zero to the maximum value, is calculated by means of the integrals

$$W_n^d = -\int_{\gamma_n} \tau^{\max} |(w^- - w^+)| dx. \tag{8}$$

3. THE PROBLEM SOLUTION

Applying the results of sec. 20.2 (Sulym, 2007) to the solution of the primary problem, one can obtain the following relations, which state that components of stress tensor and derivatives of displacement at the line L of infinite plane S, and inside the latter are equal to

$$\begin{aligned}
&\begin{cases}
\sigma_{yz}^{\pm}(x,t) = \mp p_k f_3^n(x,t) - C g_6^n(x,t) + \sigma_{yz}^{0\pm}(x,t),\\
\sigma_{xz}^{\pm}(x,t) = \mp C f_6^n(x,t) + p_k g_3^n(x,t) + \sigma_{xz}^{0\pm}(x,t),
\end{cases}\\
&\left(z \in S_k; r = 3,6; k = 1,2; \ j = 3-k\right);\\
&g_r^n(z,t) \equiv \frac{1}{\pi} \int_{L'_n} \frac{f_r^n(x,t)dx}{x-z},\\
&p = \frac{1}{G_1 + G_2}, \ p_k = G_k p, \ C = G_1 G_2 p,\\
&\sigma_{yz}(z,t) + i\sigma_{xz}(z,t) = \sigma_{yz}^0(z,t) + i\sigma_{xz}^0(z,t) +\\
&+ip_k g_3^n(z,t) - C g_6^n(z,t).
\end{aligned} \tag{9}$$

The superscript "+" corresponds to $k = 2$ and "- " corresponds to $k = 1$. The values denoted with superscript "0" characterize corresponding quantities in a continuous medium without cracks under the corresponding external loading (the homogeneous solution):

$$\begin{aligned}
&\sigma_{yz}^0(z,t) + i\sigma_{xz}^0(z,t) = \tau(t) + i\{\tau_k(t) +\\
&+D_k(z,t) + (p_k - p_j)\overline{D}_k(z,t) + 2p_k D_j(z,t)\},\\
&D_k(z,t) = -\frac{Q_k(t) + iG_k b_k(t)}{2\pi(z - z_{*k})} \quad \begin{pmatrix} z \in S_k, \\ k = 1,2; \ \ j = 3-k \end{pmatrix}.
\end{aligned} \tag{10}$$

Using Eqs (9), (10) and the condition (1) of presence of limiting friction force at the crack slippage lines γ_n under the mutual displacement of faces in the out-of-plane direction z (at other crack zones friction forces corresponds to the value defined by a condition of a perfect mechanical contact) one obtains the system of $2N$ singular integral-differential equations

$$\begin{cases}
f_3^n(x,t) = 0, \ \ (x \in L')\\
g_6^n(x,t) = \frac{1}{2C}\left(\left\langle\sigma_{yz}^0(x,t)\right\rangle + 2\text{sgn}[w]\tau_{yz}^{\max}\right),
\end{cases} \tag{11}$$

which solution is known (Sulym, 2007).

For the detailed analysis of the solution of the problem consider a special case of presence of a single $(N = 1)$ crack (contact defect) with $L'_1 = [-b; \ b]$ and the slippage line arising at $\gamma_1 = [-a; \ a] \ \ (a \le b)$ under symmetric $(z_{*k} = \pm id)$ loading. The solution of the integral equation (11) after calculation of corresponding integrals is as follows

$$\begin{aligned}
&f_6(x,t) = \frac{1}{\pi C\sqrt{a^2 - x^2}}\left\{\pi\left(\tau(t) + \text{sgn}[w]\tau_{yz}^{\max}\right)x +\right.\\
&+\sum_{k=1}^{2} p_{3-k}\left(Q_k(t)\text{Im}\frac{\sqrt{z_{*k}^2 - a^2}}{x - z_{*k}} +\right.\\
&\left.\left.+\left(G_k b_k(t)\text{Re}\left(\frac{\sqrt{z_{*k}^2 - a^2}}{x - z_{*k}} + 1\right)\right)\right\} \ \ (x \in [-a; \ \ a]).
\end{aligned} \tag{12}$$

The function $X(z) = \sqrt{z^2 - a^2}$ is understand as a branch, satisfying the condition $\sqrt{z^2 - a^2}/z \to 1$ as $z \to \infty$. Similar reasoning is used for a choice of branches of functions $\sqrt{z_{*k}^2 - a^2}$ and $\sqrt{\bar{z}_{*k}^2 - a^2}$, $k = 1, \ 2$.

Expression for displacement discontinuity $[w]$ is received with

integration of Eq (12):

$$[w](x,t)=\int_{-a}^{x} f_6(x,t)dx=-\frac{1}{C}(\tau(t)+ \\ +\mathrm{sgn}[w]\tau_{yz}^{\max})\sqrt{a^2-x^2}+ \\ +\frac{1}{\pi C}\{\sum_{k=1}^{2} p_{2-k}\,(Q_k(t)\mathrm{Im}I(x,z_{*k})+ \\ +G_k b_k(t)\left(\pi+2\arcsin\frac{x}{a}+\mathrm{Re}I(x,a,z_{*k})\right)\Big)\} \tag{13}$$

where

$$I(x,a,z)\equiv\sqrt{z^2-a^2}\int_{-a}^{x}\frac{dx}{\sqrt{a^2-t^2}(x-z)}= \\ =i\ln\frac{a(z-x)}{a^2-xz-i\sqrt{a^2-x^2}\sqrt{z^2-a^2}}. \tag{14}$$

Introducing the stress intensity factor (SIF) with the relation

$$K_3=\lim_{r\to o\ (\theta=0)}\sqrt{\pi r}\sigma_{yz}, \tag{15}$$

it is simple to obtain analytical expression for SIF in the case of a crack with a slippage line $\gamma_1=[-a;\ a]\ \ (a\le b)$:

$$K_3^{\pm}(t)=\frac{1}{2\sqrt{\pi a}}\int_{-a}^{a}\sqrt{\frac{a\pm x}{a\mp x}}\big(\langle\sigma_{yz}^0(x,t)\rangle+ \\ +2\mathrm{sgn}[w]\tau_{yz}^{\max}\big)dx=\frac{1}{\sqrt{\pi a}}\{\pi a(\tau(t)+ \\ +\mathrm{sgn}[w]\tau_{yz}^{\max})-\sum_{k=1}^{2}p_{2-k}\Bigg(Q_k(t)\mathrm{Im}\frac{a\pm z_{*k}}{\sqrt{z_{*k}^2-a^2}}+ \\ +b_k(t)G_k\mathrm{Re}\left(\frac{a\pm z_{*k}}{\sqrt{z_{*k}^2-a^2}}\mp 1\right)\Bigg)\Bigg\}. \tag{16}$$

Let's address the question on the size a of a slippage zone. In the course of increase in loading it is possible to allocate three phases essentially different from the point of view of the development of crack face slippage under the longitudinal shear:

1. The applied loading is still so small, that the condition (2) holds everywhere along L, i.e. slippage does not arise in general.
2. The applied loading is already sufficient for conditions (1) to hold at least at some small line $\gamma_1=[-a;\ a]\ \ (a\le b)$, but its size is less than established size $L'_1=[-b;\ b]$ of a crack. Loading at which the slippage first occurs is further named the first critical loading. While loading at a stage of the first phase of its change has not reached the first critical size, existence of a crack will not have any influence on the stress strain state of a solid. Everything occur the same as if two half-spaces pressed to each other are the object of research. In case of transition to the second loading phase, for determination of the size a of a slippage zone it is possible to use a condition of equality to zero of stress intensity factor given by Eq (22) in (Cherepanov, 1966).
3. If the loading increases such that the size of a crack (natural cohesive or adhesive forces of half-spaces outside the cracks) limits the slippage zone (in the absence of restrictions, a tends to exceed b), then at the crack tips singular stresses are present, and hence, SIF is nonzero. In this case the slippage zone γ_1 coincides with a crack L'_1. The minimal loading, for which the slippage line equals to the crack length thus initiating stress singularity at its tips, is further called the second critical loading.

Presence of the analytical solution for all parameters of stress strain state, and in particular, for SIF allows to calculate analytically the work of friction forces at the line L'_1 of slippage for any considered kind of loading. This work, and hence, energy dissipated on L'_1 due to change in external loading at certain time t is determined through the integral

$$W_1^d(t)=-\int_{-a}^{a}\tau_{yz}^{\max}|[w](x,t)|\,dx= \\ =-\frac{\tau_{yz}^{\max}}{C}\Big|\frac{\pi a^2}{2}\big(\tau(t)+\mathrm{sgn}[w]\tau_{yz}^{\max}\big)+ \\ +\sum_{k=1}^{2}p_{2-k}\Big(Q_k(t)\mathrm{Im}\Big(\sqrt{z_{*k}^2-a^2}-z_{*k}\Big)+ \\ +G_k b_k(t)\mathrm{Re}\Big(\sqrt{z_{*k}^2-a^2}-z_{*k}\Big)\Big)\Big|. \tag{17}$$

Let's analyze expressions (12- 13), (16- 17) for the most indicative variant of loading by concentrated force $Q_2(t)$, which changes monotonously from zero to its maximum value $Q_{\max}$. The force is applied at the point $z_{*2}=id$ of an upper half-space. Then from expression

$$K_3(t)=-\sqrt{\pi a}\tau_{yz}^{\max}+\sqrt{\frac{a}{\pi}}\frac{p_1Q_2(t)}{\sqrt{a^2+d^2}} \tag{18}$$

accounting for the fact that $\mathrm{sgn}[w]=-1$ under the monotonous increase in loading, one obtains the slippage condition

$$Q_2(t)\ge Q_2^*=\frac{\pi d\tau_{yz}^{\max}}{p_1} \tag{19}$$

and the size of a slippage zone

$$\boldsymbol{a(t)=\sqrt{\frac{p_1^2Q_2(t)^2}{\pi^2\tau_{yz}^{\max 2}}-d^2}=d\sqrt{\frac{Q_2(t)^2}{Q_2^{*2}}-1}.} \tag{20}$$

Hereinafter Q_2^* is the first critical value of the force, at which slippage starts at certain time t^*. Assuming that $a=b$ in (20) one can obtain the second critical value for the concentrated force loading, which induces nonzero SIF and stress singularity at crack tips,

$$Q_2^{**}=\frac{\pi\tau_{yz}^{\max}}{p_1}\sqrt{d^2+b^2}=Q_2^*\frac{\sqrt{d^2+b^2}}{d}. \tag{21}$$

Hence, accepting for a generality, that $Q_{\max}\ge Q_2^{**}$, the following values are obtained for the stress strain state parameters for $Q_2(t)\le Q_2^*$:

$$f_6(x,t)=[w](x,t)=g_6(z,t)\equiv 0; \tag{22}$$

for $Q_2^*\le Q_2(t)\le Q_2^{**}$:

$$f_6(x,t)=\frac{x}{C\sqrt{a^2-x^2}}\big(-\tau_{yz}^{\max}+ \\ +\frac{p_1Q_2(t)\sqrt{a^2+d^2}}{\pi(x^2+d^2)}\big), \\ [w](x,t)=\frac{p_1Q_2(t)}{2\pi C}\ln\frac{\sqrt{a^2+d^2}-\sqrt{a^2-x^2}}{\sqrt{a^2+d^2}+\sqrt{a^2-x^2}}+ \\ +\frac{1}{C}\tau_{yz}^{\max}\sqrt{a^2-x^2}\ \ (|x|\le a); \tag{23}$$

$$W_1^d(t)=\frac{\pi a^2\tau_{yz}^{\max 2}}{2C}- \\ -\frac{\tau_{yz}^{\max}}{C}p_1Q_2(t)\big(\sqrt{a^2+d^2}-d\big) \tag{24}$$

or accounting for Eq (19)

$$W_1^d(t)=-\frac{{p_1}^2}{2\pi C}(Q_2(t)-Q_2^*)^2; \tag{25}$$

for $Q_2^{**}\le Q_2(t)\le Q_{\max}$ one should replace a with b in Eqs (18), (23) and (24).

In case of identical materials of half-spaces ($G_1 = G_2 = G$) one should use in the abovementioned equations the following parameters: $C = G/2,\ \ p_1 = p_2 = 1/2$.

At a smooth contact between crack edges (friction coefficient is zero) one should assume that $\tau_{yz}^{\max} = 0$ in the abovementioned equations. In this case at arbitrary magnitude of the considered variants of loading the slippage zone instantly grows to the size of a crack.

For solution of the problem for various combinations of loading it is necessary to consider that superposition of solution for variants of loading can be not always used due to the nonlinearity of the problem considered.

4. THE NUMERICAL ANALYSIS

On an example of the aforementioned variant of loading let us illustrate the application of the proposed approach to determination of the size of a slippage zone, the displacement discontinuity at L'_1, and energy dissipation depending on the basic parameters of stress strain state (the magnitude and remoteness of the applied force, friction coefficient, material properties). Based on Eqs (20)–(25) the following dimensionless values are further considered: $\tilde{a} = a/b$, $\tilde{x} = x/b$, $\tilde{d} = d/b$, which are normalized length of slippage line, x coordinate and remoteness of a force application point, respectively; $\tilde{Q}_2(t) = Q_2(t)/\pi bP$, $\tilde{Q}_2^* = Q_2^*/\pi bP = \tilde{d}\alpha/p_1$, which are normalized magnitudes of acting force and the first critical force; and $\widetilde{w}(x,t) = [w]C/bP$, $\widetilde{W}_1^d = W_1^d C/\pi b^2 P^2$, $\tilde{K}_3 = K_3/\sqrt{\pi b}P$, which are normalized displacement discontinuity, dissipation energy and SIF, respectively.

Fig. 2 shows the dependence of the dimensionless length $\tilde{a}$ of a slippage zone on the ratio $\tilde{Q}_2(t)/\tilde{Q}_2^*$ in the range from zero to $\tilde{Q}_{\max}/\tilde{Q}_2^* \geq \tilde{Q}_2^{**}/\tilde{Q}_2^* = \sqrt{1+\tilde{d}^2}/\tilde{d}$ for various values of the remoteness parameter $\tilde{d}$. It is well noticed that with remoteness of a force application point together with natural increase in the first critical force the relative slippage zone growth rate also essentially increases.

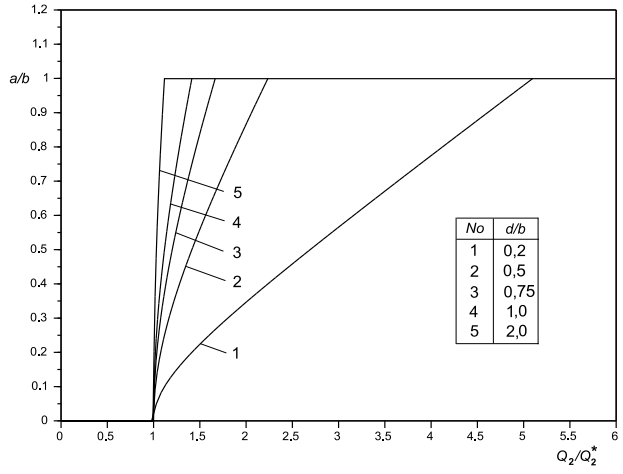

Fig. 2. Dependence of the size of a slippage zone on the loading parameter

Figs 3 and 4 depict the change of the displacement discontinuity function $\widetilde{w}(x,t)$ depending on the x/b for various cases of change in the magnitude and remoteness of the applied force $\tilde{Q}_2(t)$, and friction coefficient α. Predictably, the increase in force magnitude leads to growth of displacements, and increase in α contrarily decrease them. Presence of the loading concentrated force renders considerably greater influence on the displacement discontinuity, if it is applied in the less rigid medium (Fig. 5).

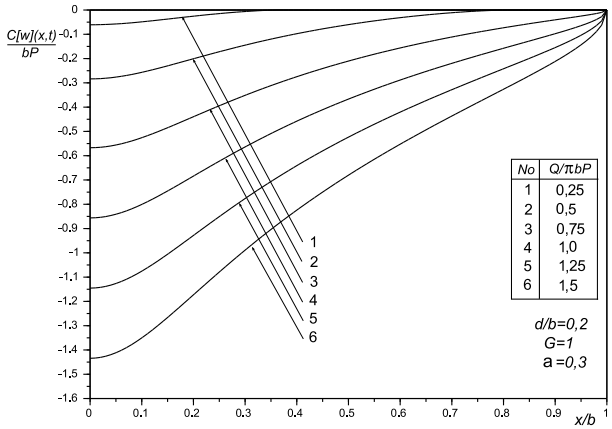

Fig. 3. Displacement discontinuity dependence on the magnitude of the applied force

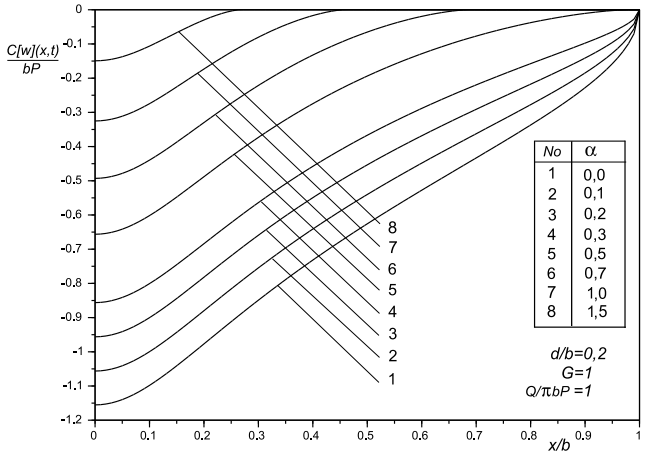

Fig. 4. Influence of friction coefficient on the displacement discontinuity

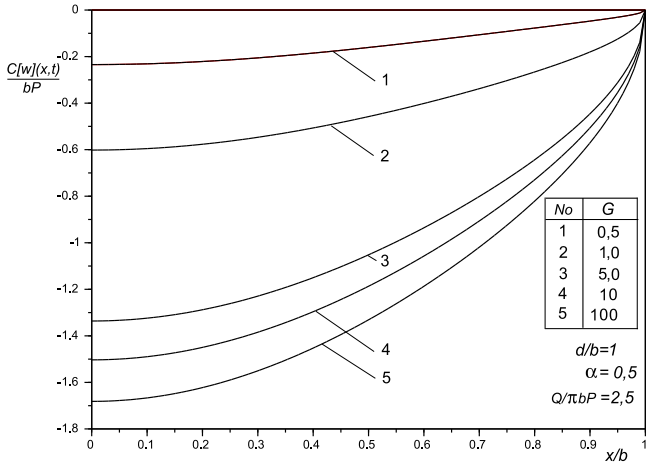

Fig. 5. Influence of shear modulus ratio of the materials on the displacement discontinuity

Figs 6 and 7 plot the dependence of the dissipated energy $W_1^d C/\pi b^2 P^2$ on the magnitude and remoteness of the applied force $\tilde{Q}_2(t)$ at various combinations of parameters G_1/G_2,d/b,

and friction coefficient α. In the plots the continuous line corresponds to energy dissipation at the second stage of loading, and das-dot one corresponds to the third stage of loading. The general tendency of the energy dissipation change can be formulated as follows: the less is relative distance d/b of the force application point and the greater is the friction coefficient, the bigger is the energy dissipation.

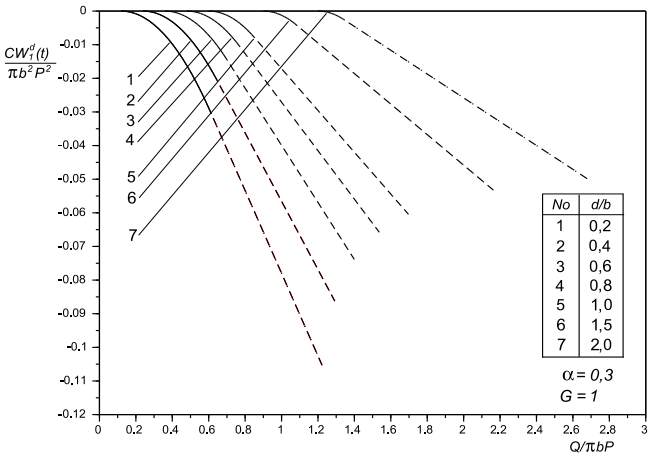

Fig. 6. Influence of the remoteness of the force application point on the energy dissipation

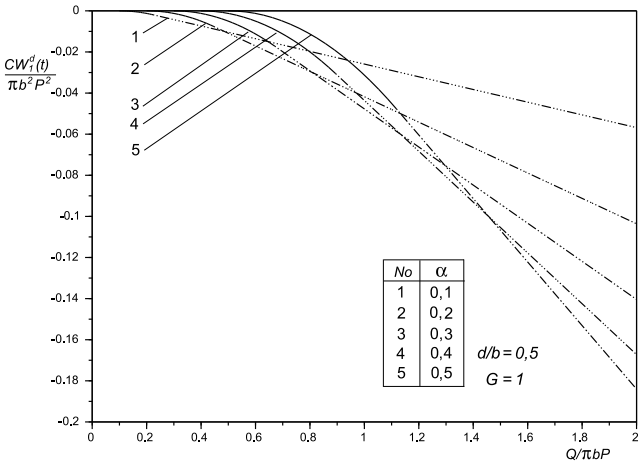

Fig. 7. Influence of the friction coefficient on the energy dissipation

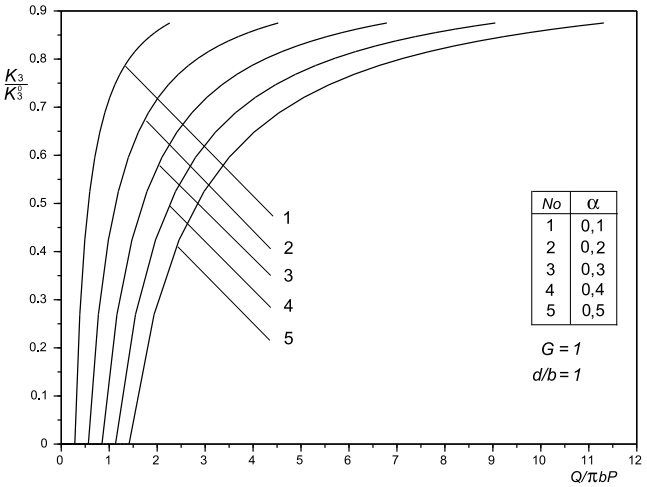

Fig. 8. Friction influence on SIF for a crack (here K_3^0 is SIF in the absence of friction)

Figs. 8-10 illustrate the influence of friction on the reduction of SIF K_3 arising at the third phase of loading, comparing to classic SIF K_3^0 calculated in the absence of friction. Dependence on the magnitude and remoteness of the applied force $\tilde{Q}_2(t)$ is studied for various combinations of parameters G_1/G_2 and d/b. The general qualitative tendency of influence of these parameters on SIF is the same as those for energy dissipation.

Doubtless interest of the further research is in the study of influence of friction slippage under the multiple, in particular cyclic, loading of a medium containing crack-like defects of contact at the interface.

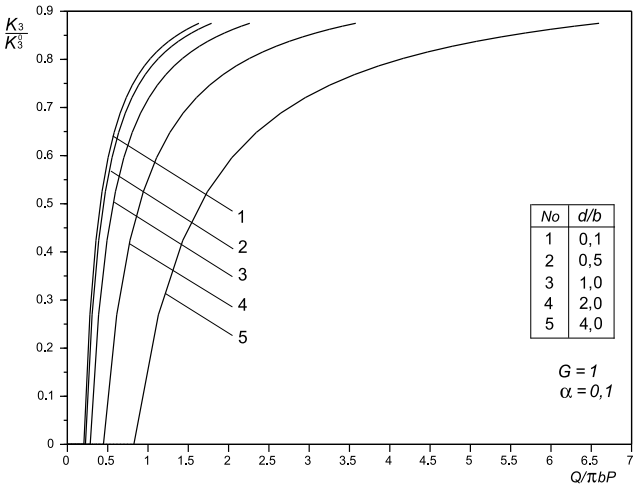

Fig. 9. Influence of remoteness of the force application point on SIF for a crack (here K_3^0 is SIF in the absence of friction)

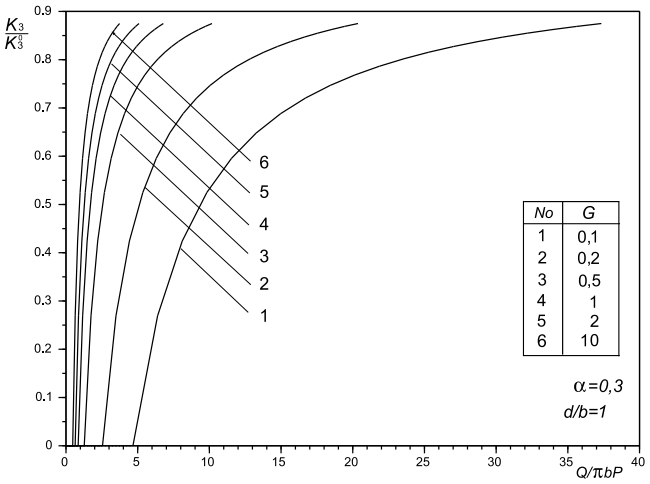

Fig. 10. Influence of shear modulus ratio of the materials on SIF for a crack (here K_3^0 is SIF in the absence of friction)

REFERENCES

1. **Antipov Yu.A. (**1995), The crack in the line section of elastic media in the presence of dry friction (in russian), *Prikl. matematika i mehanika*, 59, Vyp. 2, 290-306.
2. **Aravas N., Sharma S.M.** (1991), An elastoplastic analysis of the interface crack with contact zones, *J. Mech. Phys. Solids,* 39**,** 311–344.
3. **Arhipenko K.M., Kriviy O.F**. (2008), Interfacial beam at different types of contact interaction with inhomogeneous anisotropic plane (in ukrainian), *Mashinoznavstvo*, 8, No 3 (129), 16–21.

4. **Bogdanovich P.N., Tkachuk D.V.** (2009), Thermal and thermo-mechanical effects in sliding contact (in russian), *Treniye i iznos*, 30, No 3, 214-229.
5. **Brussat T.R., Westmann R.A. (**1974), Interfacial slip around rigid fiber inclusion, *Journal of Composite Materials,* 8, No. 4, 364–377.
6. **Cherepanov G.P.** (1966), On the development of cracks in compressed bodies (in russian), *Prikladnaya matematika i mehanika*, 30, No 1, 82–93.
7. **Comninou M.** (1977), The interface crack, *J. Appl. Mech.,* 44**,** 631–636.
8. **Comninou M., Schmueser D. and Dundurs J.** (1980), Frictional slip between a layer and a substrate caused by a normal load, *Int. J. Engn. Sci.*, 18**,** 131–137.
9. **Datsyshyn O.P., Kadyra V.M. (**2006), A fracture mechanics approach to prediction of pitting under fretting fatigue conditions, *Int. J. of Fatigue,* 28, No 4, 375–385.
10. **Evtushenko A.A., Sulim G.T.** (1981), Stress concentration near a cavity filled with a liquid, *Soviet Materials Science*, 16**,** No. 6, 546–549.
11. **Goryacheva I.G.** (2001), *Mechanics of frictional interaction* (in russian), Moskva, Nauka.
12. **Goryacheva I.G., Rajeev P.T. and Farris T.N.** (2001), Wear in partial slip contact, *J. Tribology,* 123**,** 848–856.
13. **Herrmann K.P., Loboda V.V.** (1999), On interface crack models with contact zones situated in an anisotropic biomaterial, *Archive of App. Mech.*, 69**,** 317–335.
14. **Hills D.A, Nowell D. and Sackfield A.** (1993), *Mechanics of elastic contact,* Butterworth-Heinemann, Oxford.
15. **Johnson K.L.** (1985), *Contact mechanics*, Cambridge: Cambridge University press.
16. **Kharun I.V., Loboda V.V.** (2003), A set of interface cracks with contact zones in combined tension-shear field, *ActaMechanica*, 166**,** 43–56.
17. **Kit G.S., Martynyak R.M. and Machishyn I.M.** (2003), The effect of fluid in the contact gap on the stress state of conjugate bodies, *Ibid*, 39, No 3, 292–299.
18. **Kundrat M.M., Sulym H.T.** (2003), Prefracture zones in the composition of high-modulus elastic inclusion with symmetric and antisymmetric load (in ukrainian), *Matematychni problem mehaniky neodnoridnyh struktur*, Lviv, 322–324.
19. **Loboda V.V., Kharun I.V.** (2001), Plane Problem of a Crack on the Interface of Orthotropic Plates with Friction of Crack Lips, *Materials Science*, 37, Issue 5, 735–745.
20. **Malanchuk N. et al.** (2007), Local sliding of bodies surface inhomogeneities caused by the actions of power and heat loads (in ukrainian), *Mashinoznavstvo*, No 7, 15–20.
21. **Martynyak R.M., Kryshtafovych A.** (2000), Friction contact of two elastic half-planes with local recesses in boundary, *J. Friction and Wear*, 21, No 4, 6–15.
22. **Martynyak R.M. et al.** (2005), Elastic interaction of two half-planes shear in the local area borders on contact gap (in ukrainian), *Mat. Metody ta fiz.-meh. polya*, 48, No 3, 101–109.
23. **Ostryk V.I., Ulitko A.F.** (2006), *Wiener-Hopf method to contact problems of theory of elasticity* (in russian)*,* Kiev, Naukova dumka.
24. **Panasyuk V.V. et al.** (1976), *Distribution tense neighborhood of cracks in the plates and shells* (in russian), Kiev, Naukova dumka.
25. **Pasternak Ya.M., Sulym H.T., Piskozub L.G.** (2010), Models of thin inclusion with the account of imperfect contact with the medium (in russian), *Proc. of VI International symposium on Tribo-Fatigue MSTF 2010 (Minsk, 25 oct. – 1 nov. 2010) in 2 parts, part 2.*, Minsk, BGU, 399–404.
26. **Piskozub J.Z., Sulim G.T.** (2008), Thermoelastic equilibrium of piecewise homogeneous solids with thin inclusions, *Journal of Engineering Mathematics*. *Special Issue Thermomechanics*, 61**,** 315–337.
27. **Popov G.Ya.** (1966), Plane contact problem of the theory of elasticity with the forces of adhesion and friction (in russian), *Prikladnaya matematika i mehanika*, 30, No 3, 551–563.
28. **Pyriev S.Yu.** et al. (2012), Thermomechanical wear during quasi-stationary frictional heating (in russian), *Treniye i iznos,* 33, No 5, 435–443.
29. **Schmueser D., Comninou M., Dundurs J.** (1980), Separation and slip between a layer and substrate caused by a tensile load, *Ibid,* 18**,** 1149–1155.
30. **Sekine H.**(1982), Mechanics of debonding along the surfaces of dispersed flat inclusions in composite materials (A model of debonding along the surface of a flat inclusion), *Trans. ASME. Journal of Applied Mechanics,* 48A, No. 11 (435), 1415–1420.
31. **Sulym H.T.** (2007), *Fundamentals of the mathematical theory of thermoelastic equilibrium of deformable bodies with thin inclusions* (in ukrainian), Lviv, Doslidno-vydavnychyy tsentr NTSh.
32. **Sulym H.T., Piskozub Y.Z.** (2004), Conditions of contact interaction (review) (in ukrainian), *Mat. metody i fiz.-meh. polya*, 47, No 3, 110–125.
33. **Ulitko A.F., Ostrik V.I.** (2002), Interfacial crack subjected to frictional contact (in ukrainian), *Visnyk Kyiv. un-tu., Ser. fiz.-mat. nauky,* 2, 133–141.
34. **Weertman J., Lin I.-H., Thomson R.** (1983), Double slip plane crack model, *Acta met.*, 31, No 4, 473–482.